INVESTIGATION OF AN UNUSUAL METAL-RNA CLUSTER IN THE P5ABC SUBDOMAIN OF THE GROUP I INTRON

A Dissertation

by

SHANNON NAOMI BURNS

Submitted to the Office of Graduate Studies of
Texas A&M University
in partial fulfillment of the requirements for the degree of

DOCTOR OF PHILOSOPHY

December 2004

Major Subject: Chemistry

INVESTIGATION OF AN UNUSUAL METAL-RNA CLUSTER IN THE P5ABC SUBDOMAIN OF THE GROUP I INTRON

A Dissertation

by

SHANNON NAOMI BURNS

Submitted to the Office of Graduate Studies of
Texas A&M University
in partial fulfillment of the requirements for the degree of

DOCTOR OF PHILOSOPHY

Approved as to style and content by:

Victoria J. DeRose (Chair of Committee)	
Frank M. Raushel (Member)	David H. Russell (Member)
J. Martin Scholtz (Member)	Emile A. Schweikert (Head of Department)

December 2004

Major Subject: Chemistry

ABSTRACT

Investigation of an Unusual Metal-RNA Cluster in the P5abc Subdomain of the Group I Intron. (December 2004)

Shannon Naomi Burns, B.S., Millersville University

Chair of Advisory Committee: Dr. Victoria J. DeRose

This dissertation focuses on the spectroscopic and thermodynamic characterization of the unusual metal-RNA cluster found in the P5abc subdomain of the *Tetrahymena* group I intron. The P5abc subdomain is a part of the P4-P6 domain found in the *Tetrahymena thermophila* group I intron self-splicing RNA. From both X-ray crystal structures of the P4-P6 domain, a remarkable cluster of Mg^{2+} or Mn^{2+} ions was found in the P5abc subdomain (Cate et al. 1996; Juneau et al. 2001). It is believed that the metal ion core in the P5abc subdomain stabilizes the active conformation of the RNA (Cate et al. 1996). An understanding of the role of these metal ions in facilitating the correct structure of the P5abc subdomain provides insight into how metal ions help overcome the folding barriers of complex RNA structures.

Under solution conditions, the properties of this uncommon metal ion core and its influence on the truncated P5abc subdomain structure have been investigated. Both EPR spectroscopy and thermal denaturation experiments

have been employed to search for a spectroscopic signature of metal ion core formation and also determine the thermodynamic contribution of the metal ion core on the stability of the folded P5abc structure.

A spectroscopic signature of metal ion core formation was assigned for the P5abc subdomain by EPR microwave power saturation studies. Power saturation studies of the P5abc subdomain, P4-P6 domain and corresponding mutants reveal that the addition of 5 equivalents of Mn^{2+} are required for the wild type P5abc subdomain to form the metal ion core under solution conditions in 0.1 M NaCl. Results from both domain and subdomain microwave power saturation studies suggest that this technique can be applied for detecting clustering of Mn^{2+} ions in other RNA structures.

The thermodynamic consequence of this metal ion core was probed by thermal denaturation techniques including UV-Vis spectroscopy and differential scanning calorimetry (DSC). DSC experiments were utilized to directly determine the thermodynamic contribution of the metal ion core. This value was determined to be an average of $\Delta\Delta G$ of -5.3 kcal/mol and is consistent with $\Delta\Delta G$ values obtained for other RNA tertiary structures.

DEDICATION

This dissertation is dedicated to my loving and supportive fiancé, Brian, and my parents, Tom and Joanne.

ACKNOWLEDGEMENTS

I would like to thank my advisor, Dr. Victoria J. DeRose, for all of her encouragement and guidance throughout my graduate school career. I would also like to thank my dissertation committee, Dr. Russell, Dr. Raushel, and Dr. Scholtz.

I would also like to thank all of the DeRose group members for their support. I have enjoyed getting to know all of you: Edith, Sara, Nak-Kyoon, Janell, Aurelie, Matt, Cynthia, Murali and Carre. Nak-Kyoon, thank you for always making me laugh. Janell, thank you for all of your help with the P4-P6 plasmid preparation; I really appreciate it.

I am fortunate to have made such amazing friends in graduate school. Sara and Lea, you are both wonderful friends; thanks for always being there for me. Sara, I really appreciate all of your help in this stressful time in my life. Alyson, I would not have made it through the first three years of graduate school without you. Holly, we have been through a lot together. I will never forget our lunches and will always treasure our friendship. Edith, thanks for your constructive editing and for being a good friend. A special thanks to the chemistry softball crew, through all the wins and losses I have made some great friends.

My parents have always been there for me. Mom and Dad, thank you for your constant love and support. I know it has been hard being far apart, but thank you for always encouraging me to reach my goals.

And finally, I would like to thank my fiancé, Brian, for all of his love and support. I would not have made it through without you. Thank you for being understanding and supportive through these graduate school years. I love you and I am looking forward to all of the good times ahead of us.

TABLE OF CONTENTS

LIST OF FIGURES

Figure Page

Figure Page

LIST OF TABLES

CHAPTER I

INTRODUCTION

Ribonucleic Acids (RNA)

The basic structure of RNA consists of a chain of monomers that contain a base, a ribose sugar and a phosphate connected through a negatively charged phosphodiester backbone (Figure 1-1). The phosphates bridge the 3' and 5' positions of successive sugar residues. The bases are adenine (A), guanine (G), cytosine (C) and uracil (U), and they are attached through a glycosidic bond to the C1' position on the ribose sugar. RNA molecules are most commonly depicted as single stranded. However, there are several forces stabilizing RNA structures including base pairing, base stacking, and ionic interactions. The most common base pairs are Watson-Crick in which G hydrogen bonds with C and A with U; however, non-Watson-Crick pairing can also occur. There are several RNA structure motifs that contribute to complex tertiary structures required for a variety of functions in cells.

Prior to the early 1980's, it was presumed that the role of RNA in the cell could be described by the central dogma of biochemistry in which DNA is transcribed into RNA and then RNA is translated into protein. Proteins were believed to be the catalytic entities of a cell that were responsible for the structure, function, development, and reproduction of an organism. In this role,

---

This dissertation follows the style of *RNA*.

RNA could be considered a carrier of genetic information found as messenger RNA (mRNA), transfer RNA (tRNA) or ribosomal RNA (rRNA). Messenger RNA's (mRNA) are RNA transcripts of DNA that direct the ribosomal synthesis of polypeptides. tRNA recognizes the mRNA code, initiating its translation into protein by carrying individual amino acids to the correct position during protein synthesis. rRNA is the RNA component of the ribosome which is the center of protein synthesis. Although RNA plays a key role in translation, RNA can serve in many other roles in the cell such as splicing, gene regulation, and catalysis. For example, RNA interference (RNAi) initiates post-transcriptional gene silencing by the introduction of double-stranded RNA as a tool to knock out expression of specific genes in a variety of organisms (Cogoni and Macino 2000). The RNA's that carry out catalysis in the absence of proteins are known as ribozymes (RNA-enzymes).

The genes of eukaryotes contain coding sequences known as exons that are interrupted by intervening sequences (IVS) or introns. The introns are unexpressed sequences. Transcription of intron-containing sequences yields a precursor RNA. The pre-RNA must undergo cleavage-ligation reactions or splicing to produce a functional RNA molecule. The discovery of self-splicing RNAs opened a new field of biological research with the discovery of catalytic RNAs (Kruger et al. 1982). There is growing evidence that the spliceosome, the RNA-protein complex that catalyzes the removal of introns in eukaryotes, is also a ribozyme (Collins and Guthrie 2000).

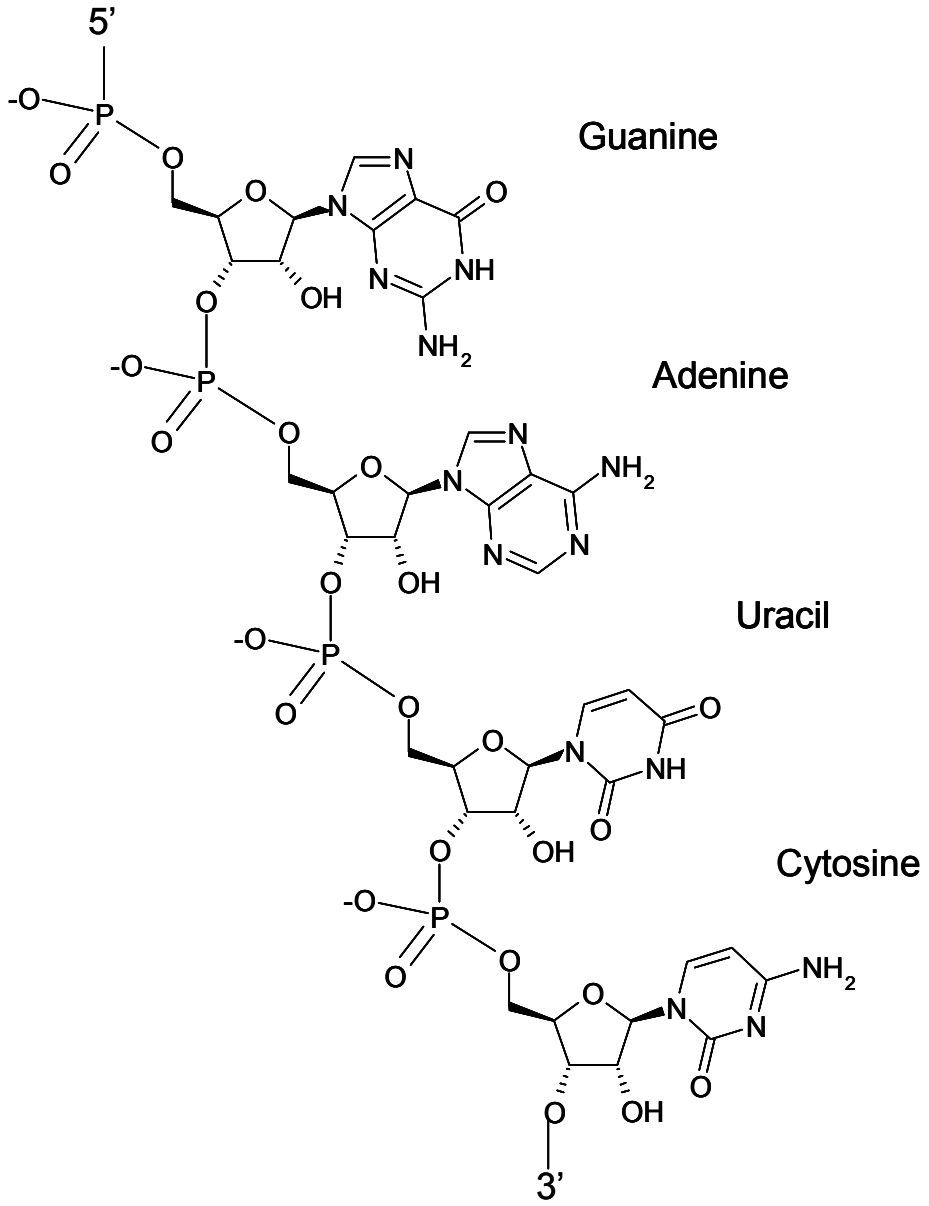

Figure 1-1. Structure of RNA.

Metal Ions and Nucleic Acids

The structure of RNA consists of a high negatively charged phosphate backbone. Therefore, the RNA structure contains the potential for metal ion coordination sites. Monovalent and divalent ions have been shown to be vital for RNA structure and function (Pyle 1993; DeRose 2003a). Metal ions can associate with the RNA through diffuse interactions in which the hydrated ions follow the electrostatic field of the RNA (Draper 2004). With the diffuse type of interaction the metal ion does not make a direct contact with the RNA molecule. A typical tertiary structure of RNA will contain a diffuse ion atmosphere of both monovalent and divalent ions. A second type of metal ions bound to RNA are the chelated ions (Draper 2004). This mode of metal ion binding involves direct ion-RNA contacts (Draper 2004). Chelated divalent ions are present in the tertiary structures of several RNA molecules including $tRNA^{Phe}$ (Shi and Moore 2000), hammerhead ribozyme (Pley et al. 1994; Scott et al. 1995), hairpin ribozyme (Rupert and Ferre-D'Amare 2001), P4-P6 domain of the group I intron (Cate et al. 1996; Juneau et al. 2001). Some common coordination modes of these metal ions that have been observed include inner- and outer-sphere coordination to the phosphodiester backbone, N7 of purines, and carbonyl oxygens (DeRose et al. 2003).

Ribozymes

Ribozymes, or catalytic RNAs, were first discovered by Cech and Altman over 20 years ago (Kruger et al. 1982; Guerrier-Takada et al. 1983). This

discovery changed the commonly held views of the central dogma that indicate that the dominant role of RNA is a genetic carrier, and that protein enzymes are the only biomolecules capable of carrying out catalytic reactions (Pyle 1993) . Ribozymes are separated into different subgroups based on their size and the reaction that they catalyze. The “large” ribozymes (> 300 nucleotides), including the group I and group II introns, mediate splicing of the RNA by a series of two phosphodiester bond cleavage-ligation reactions (Figure 1-2A). Recently it has been proposed that the spliceosome is a ribozyme based on the similarity of the chemistry of the group II intron to mRNA splicing (Sontheimer et al. 1997; Gordon et al. 2000; Yean et al. 2000; Valadkhan and Manley 2001). RNase P is also a large ribozyme, and it catalyzes the hydrolytic cleavage reaction to remove the 5’ end of pre-tRNA (Guerrier-Takada et al. 1983). The “small” ribozymes (30-100 nucleotides), such as the hammerhead, hepatitis delta virus, and the hairpin ribozymes, perform site-specific phosphodiester bond cleavage reactions (Figure 1-2B) (Tanner 1999). These RNA molecules are derived from the RNA genomes of plant viruses and viroids, which use these sequences to provide a unit length copy of their genome following rolling circle replication (Tanner 1999).

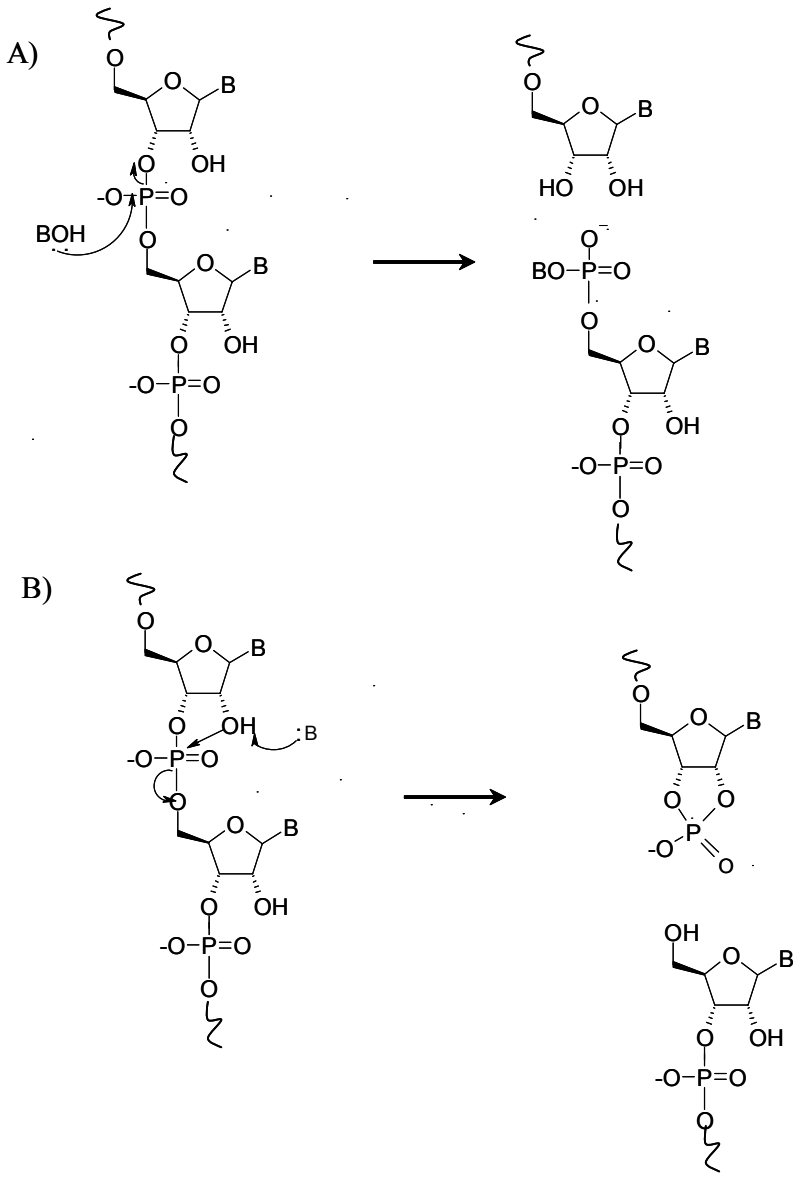

Figure 1-2. Reactions catalyzed by ribozymes. a) The reaction mechanism of the large ribozymes. b) The reaction mechanism of the small ribozymes.

An exception to the notion that ribozymes generally act upon RNA is the remarkable revelation that the ribosome is a ribozyme. The peptidyl-transferase reaction of the ribosome is catalyzed by the 23S rRNA component of its 50S

subunit (Nissen et al. 2000). This discovery that the ribosome is a ribozyme elevates the interest in these RNA-enzymes (Lilley 2003).

The general mechanisms by which proteins facilitate chemical reactions have been well characterized and generally result from the diversity of amino acid side chains. However, the general mechanisms by which nucleic acids perform chemical reactions are not well understood. There are a few proposed mechanisms for how RNA can facilitate catalysis which include the roles of nucleobases and metal ions in general acid-base and electrophilic catalysis and the importance of substrate orientation and proximity (Lilley 2003). For both the ribosome and the hepatitis delta virus (Perrotta et al. 1999; Nissen et al. 2000; Luptak et al. 2001), a base has been proposed to have an altered pK_a allowing acid-base chemistry to occur at physiological pH. Metal ions are vital for the folding of RNA molecules and thus generating the active conformation of the ribozyme. Since it has been proposed that substrate orientation and proximity may have an effect on catalysis, metal ions may in turn aid in this requirement (Murchie et al. 1998). Metal ions have also been proposed to directly aid in the catalysis of ribozymes. However, it was shown that decent levels of activity could be obtained in the hammerhead, hairpin and VS ribozymes in the presence of high levels of monovalent ions such as lithium and ammonium, therefore, excluding a requirement for site-specific binding of the ion (Murray et al. 1998). Perhaps the best evidence for the direct role of metal ions in the chemical step of a ribozyme reaction comes from the proposed mechanism for

the group I intron from *Tetrahymena thermophila*. Thiophilic metal ion rescue experiments involving individual phosphorothioate substitutions around the active site resulted in a proposal consisting of four active site ligands and three separate metals (Shan et al. 2001). One metal ion coordinates the 3'-departing oxygen of the oligonucleotide substrate and the pro-S(P) oxygen of the reactive phosphoryl group; another metal ion coordinates the attacking 3'-oxygen of the guanosine nucleophile; a third metal ion bridges the 2'-hydroxyl of guanosine and the pro-S(P) oxygen of the reactive phosphoryl group (Figure 1-3) (Shan et al. 2001).

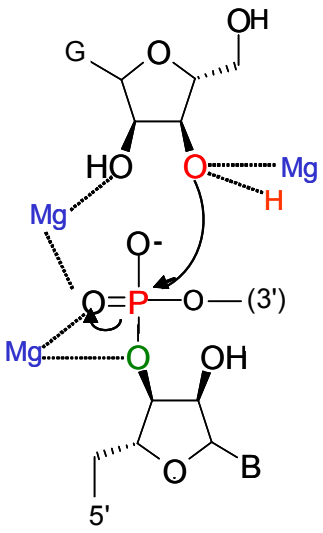

Figure 1-3. Proposed role of metal ions in the active site of the group I intron from *Tetrahymena thermophilia* (Shan et. al, 2001). The three proposed Mg^{2+} ions are shown in blue.

Group I Intron Ribozyme

The pre-rRNA of *Tetrahymena thermophila*, a ciliated protozoan, contains an intervening sequence of 413 nucleotides (Kruger et al. 1982) with a secondary structure made up of nine domains, labeled P1-P9. The Tetrahymena intron is a member of the group I introns, which are found in the mitochondria, chloroplasts, and nuclei of eukaryotes. Group I introns mediate splicing of the RNA by two transesterfication reactions that result in the excision of the intron and the ligation of the flanking exon sequences (Kruger et al. 1982; Cech 1990). The three step process is depicted in Figure 1-4. In the first reaction, the 3' hydroxyl of an exogenous guanosine performs a nucleophilic attack on a specific phosphodiester bond at the 5' splice site. The phosphodiester bond is cleaved, and the guanosine forms a 5', 3'-phosphodiester bond at the 5' end of the intron. The free 3' hydroxyl performs a nucleophilic attack at the 3' splice site forming ligated exons and release the intron with the non-encoded guanosine (Cech 1990; Tanner 1999). Splicing requires an exogenous guanosine and divalent cations such as Mg^{2+} or Mn^{2+} (Cech 1990).

The catalytic core of the Group I intron from *Tetrahymena thermophila* consists of two main structural domains: base paired (P) regions P3-P9 and P4-P6 (Doudna and Cech 1995). The P3-P9 domain contains the guanosine binding site of the intron (Doudna and Cech 1995). The P4-P6 region, which consists of helical segments P4, P5 and P6, contains half of the conserved

catalytic core (Figure 1-5) (Y. H. Wang et al. 1994; Doudna and Cech 1995). A 5.0 Å crystal structure of the Tetrahymena group I intron containing helices P3-P9 was solved by Cech and coworkers in 1998 (Golden et al. 1998). The crystal structure depicts the P4-P6 domain, similar to the previous structure of the P4-P6 domain by itself (Cate et al. 1996), with the P3-P9 helices wrapped around it (Golden et al. 1998). The close packing of the P4-P6 domain with the P3-P9 domain creates a cleft into which the P1 helix, containing the 5' splice site, could fit. The structure also reveals a tight binding site in the P7 helix for the guanosine cofactor that initiates splicing (Golden et al. 1998). Since the structure did not contain the P1-P2 domain containing the splice site, little information could be attained about the reaction mechanism (Golden et al. 1998; Doherty and Doudna 2000).

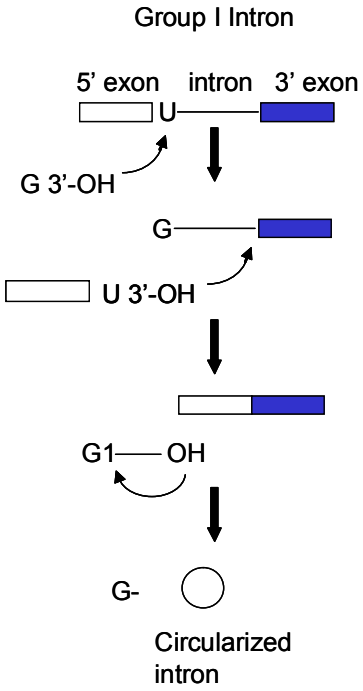

Figure 1-4. Splicing mechanisms of group I introns.

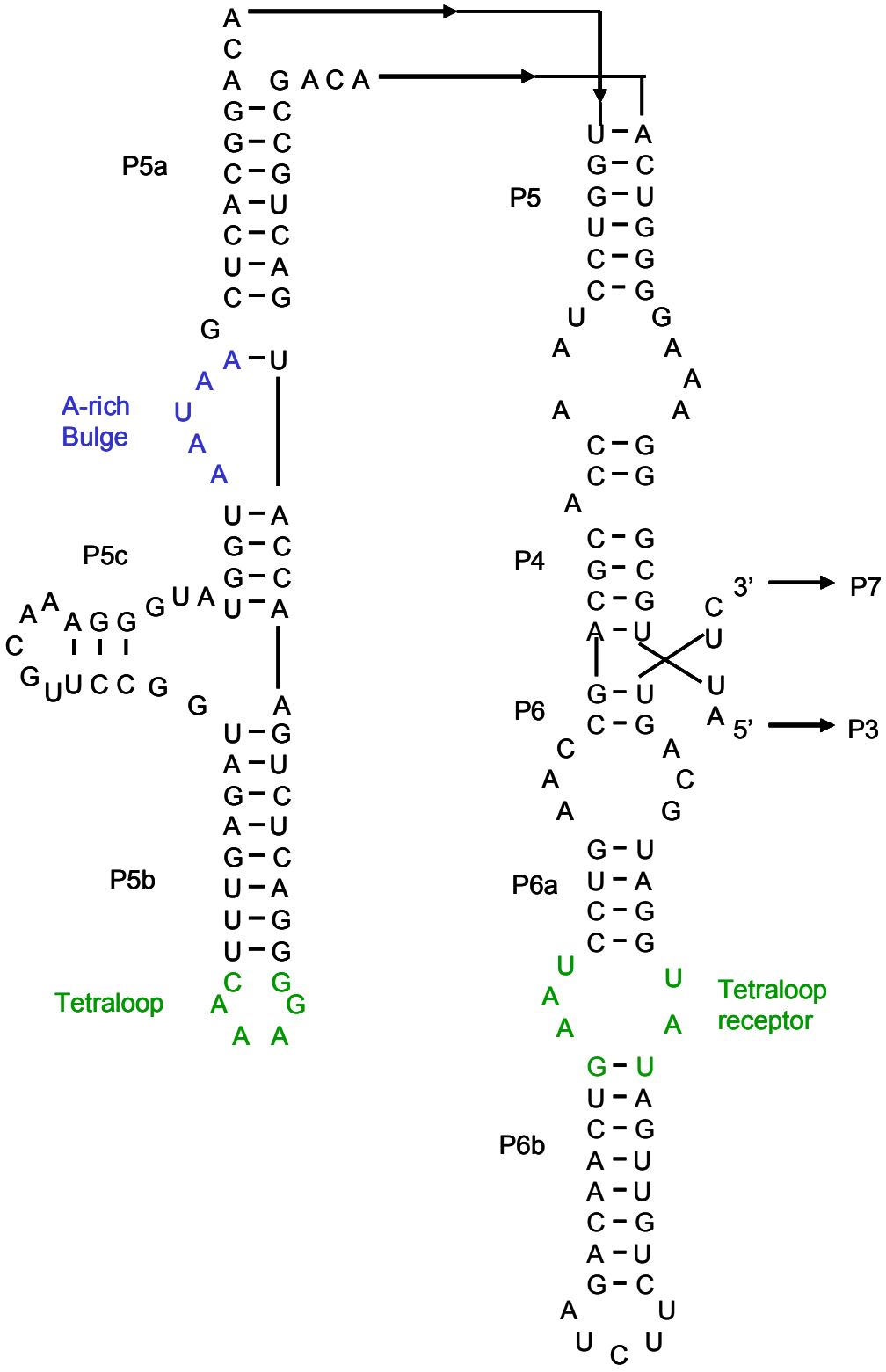

Figure 1-5. Secondary Structure of the P4-P6 domain.

The tertiary folding of the 160 nucleotide P4-P6 domain has been studied extensively (Woodson 2002). Hydroxyl radical footprinting studies reveal that this domain from *Tetrahymena* folds independently of the rest of the intron (Latham and Cech 1989; Celander and Cech 1991). Within the group I intron, this domain folds before the rest of the ribozyme (Murphy and Cech 1993; Murphy and Cech 1994). X-ray dependent hydroxyl radical footprinting studies demonstrated that the P4-P6 domain folds in 50 ms to 1 s (Sclavi et al. 1998; Deras et al. 2000; Silverman et al. 2000). The P4-P6 domain alone adopts the same secondary structure and tertiary fold as seen when included with the rest of the intron (Laggerbauer et al. 1994; Murphy and Cech 1994; Y. H. Wang et al. 1994). Furthermore, the P4-P6 domain can assemble with the remainder of the intron in *trans* to reconstitute catalytic activity (Doudna and Cech 1995). Tertiary folding of the P4-P6 domain occurs only in the presence of divalent ions (Celander and Cech 1991; Takamoto et al. 2002).

The *Tetrahymena* P4-P6 domain also contains the P5abc subdomain, which does not perform self-splicing/cleavage reactions (Celander and Cech 1991; Takamoto et al. 2002), but is required for efficient catalysis (Michel and Westhof 1990). The P5abc subdomain contains an A-rich bulge, a GAAA tetraloop, and a junction of three helices, P5a, P5b, and P5c. Fe-EDTA cleavage experiments reveal that the native P5abc subdomain of the group I intron from *Tetrahymena* folds independently of the rest of the intron (Latham and Cech 1989; Celander and Cech 1991). This domain folds before the rest of

the ribozyme (Murphy and Cech 1993; Zarrinkar and Williamson 1994; Doudna and Cech 1995; Downs and Cech 1996). Removal of the P5abc subdomain from the intron eliminates splicing activity except for in the presence of high concentrations (25-100 mM) of magnesium ions (Joyce et al. 1989), but the P5abc subdomain is stable enough that it can be added in trans to restore activity (van der Horst et al. 1991). It is believed that this subdomain stabilizes the active conformation of the RNA (Cate et al. 1996).

The 2.8 Å resolution crystal structure of the P4-P6 domain from the *Tetrahymena* group I intron was solved by Doudna and coworkers (Figure 1-6A) (Cate et al. 1996). In this domain, a flexible internal loop, J5/5A (J stands for a joining region between two duplexes) allows the backbone to make a ~ 180^{o} bend, enabling parallel association of two coaxially stacked helical segments, P5abc and P4-P5-P6. The P4, P5 and P6 helices pack tightly against the three-helix junction of P5abc (Cate et al. 1996). P5abc binds at two distinct locations to the coaxially stacked P5, P4 and P6 helices. The A-rich bulge of P5abc contacts the minor groove of helix P4 by backbone and base-mediated hydrogen bonds forming a ribose zipper. Also, the GAAA tetraloop of P5abc docks into its tetraloop receptor by both cross-helical base stacking and extensive hydrogen bonding (Cate et al. 1996; Doherty et al. 1999). Similar tetraloop/tetraloop receptor interactions have been observed in other large RNAs including group II introns and ribosomal RNA (Costa and Michel 1995).

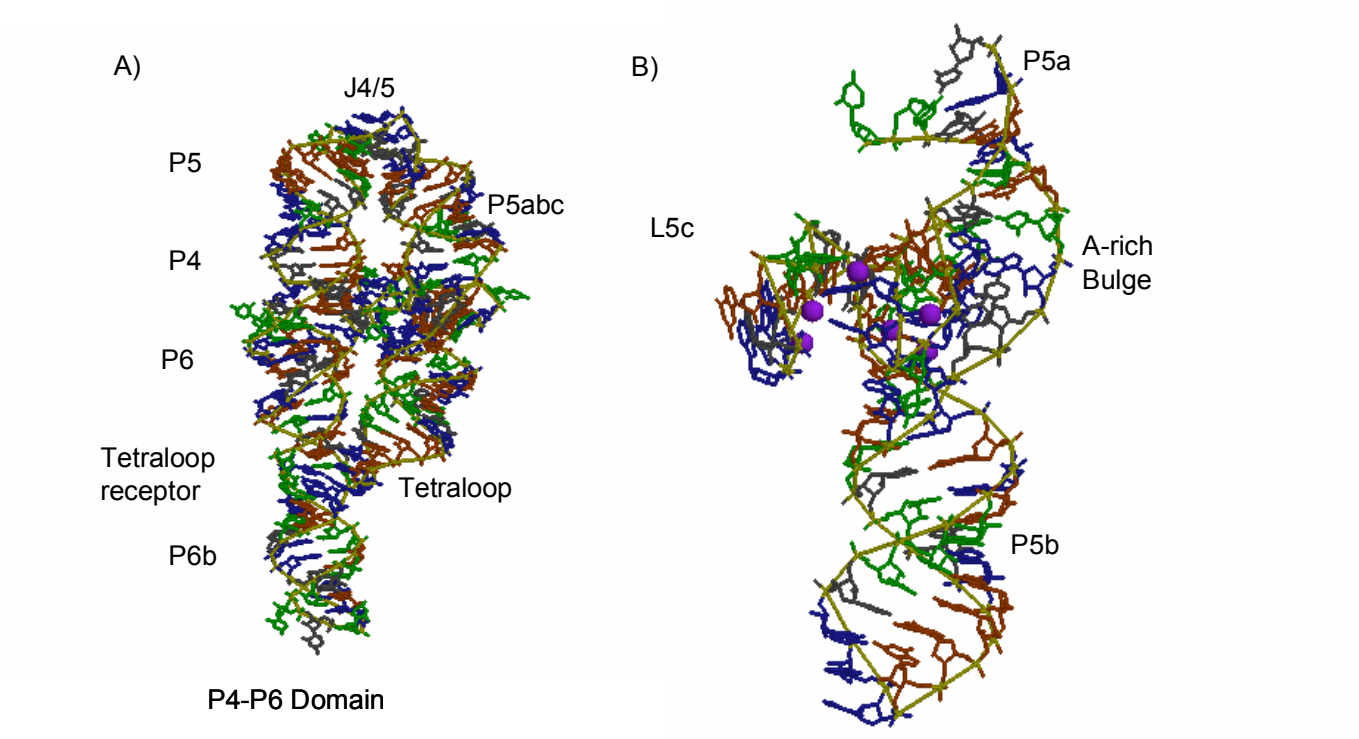

Figure 1-6. The P4-P6 domain and the P5abc subdomain. A) 2.8 Å crystal structure of the P4-P6 domain (PDB 1G1D). B) P5abc subdomain excised from the crystal structure of the of the P4-P6 domain. The 6 magnesium ions are shown as purple spheres.

A remarkable feature of the P4-P6 domain crystal structure is the clustering of six magnesium ions in the P5abc subdomain (Figure 1-6B) (Cate et al. 1996). The subdomain three helix junction protects the A-rich bulge, which, according to the crystal structure, makes a corkscrew turn to form key tertiary interactions between the helical halves of the P4-P6 domain (Cate et al. 1997) .

The magnesium ions may organize the three-helix junction in order to drive the folding pathway of the P4-P6 domain and ultimately the rest of the ribozyme (Cate et al. 1997).

Deleting a single nucleotide, C209, located in the P4 helix of the P4-P6 domain was shown to form a more stable tertiary structure in solution (Juneau and Cech 1999). Using this mutation a 2.25Å crystal structure of the P4-P6 domain was solved by Cech and coworkers (Juneau et al. 2001). In this crystal structure 10 Mg^{2+} ions were located in the P5abc subdomain, including the 6 Mg^{2+} ions found in the cluster from the previous 2.8Å crystal structure. The Mg^{2+} ions found in the cluster exhibited both inner-sphere and outer-sphere coordination as depicted in Figure 1-7 (Juneau et al. 2001). The majority of the magnesium ion coordination was to nonbridging phosphate oxygens. In addition, cobalt (III) hexammine and Mn^{2+} were used to substitute for Mg^{2+} in the crystal structure. Cobalt (III) hexammine was found to bind to specific sites that are not occupied by Mg^{2+}(Juneau et al. 2001). Mn^{2+} substituted for all of the Mg^{2+} ions that were innersphere coordinated to the RNA (Juneau et al. 2001). This result is consistent with Mn^{2+} preferring innersphere coordination (Feig 1999; Gesteland 1999).

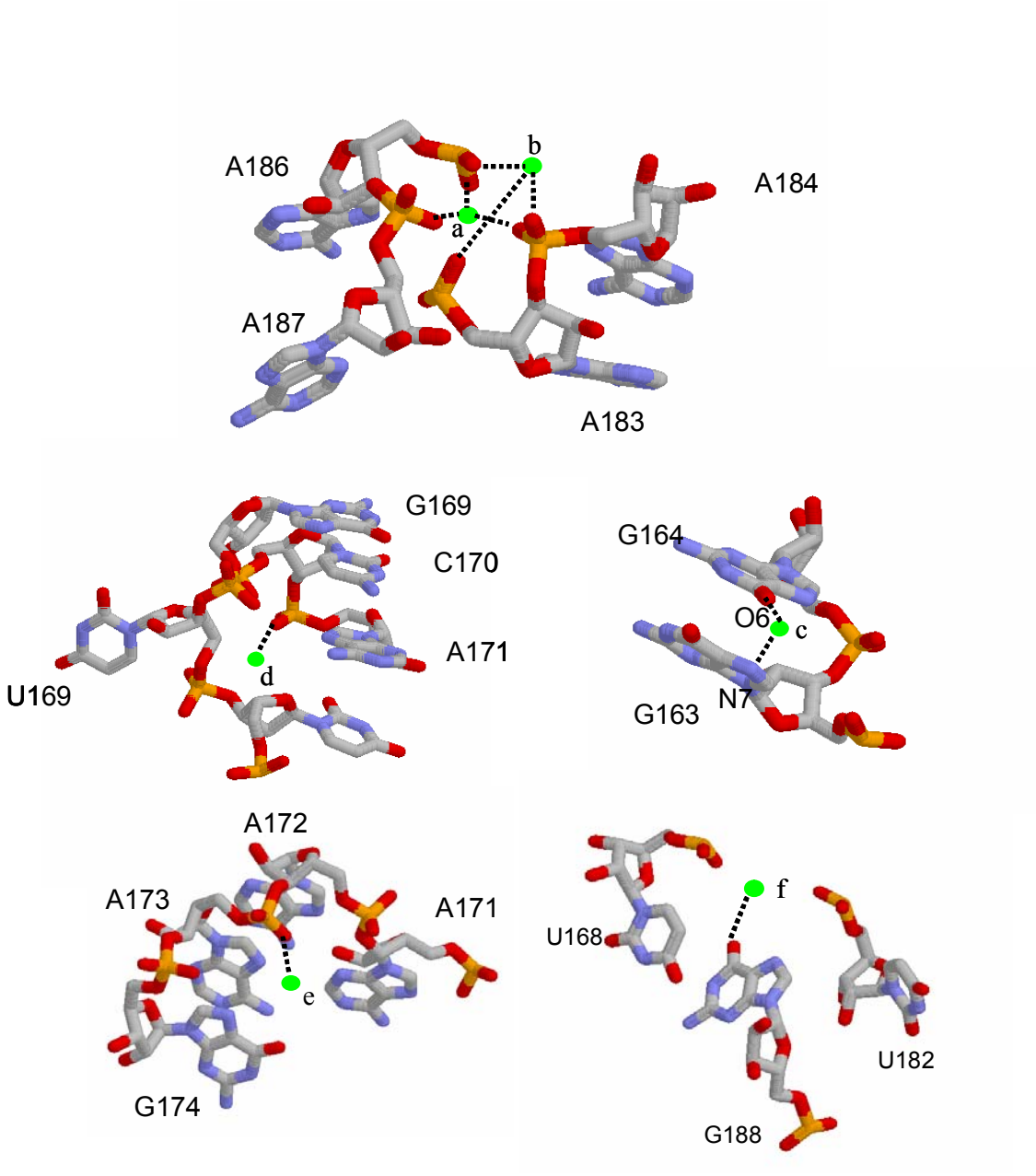

Figure 1-7. Six metal binding sites found in the metal ion core of the P5abc subdomain. (Juneau et al., 2001) Green spheres represent either Mg^{2+} or Mn^{2+}ions, innersphere coordination is depicted as black dashed lines.

To determine whether divalent metal ions play a role in folding of the P4-P6 domain, phosphorothioate substitution experiments were utilized to disrupt five of the six magnesium binding sites (Cate et al. 1997; Basu and Strobel 1999). Seven positions that contained a single R_p phosphorothioate substitution disrupted the Mg^{2+} dependent tertiary fold of the RNA (Cate et al. 1997). Six of these positions involved coordination to the five Mg^{2+} ions in the core of the subdomain. Mn^{2+} rescue of phosphorothioate interference was obtained for the G163, A171, A187 and G188 residues. However, Mn^{2+} could not rescue the phosphorothioate effects at A184 and A186, both of which coordinate the same metal in the A-rich bulge (Basu and Strobel 1999). Results from these experiments demonstrate that these five Mg^{2+} ions play a role in forming the tertiary structure of the intron.

The secondary structure of a truncated 56-nucleotide P5abc subdomain was determined by solution NMR (Figure 1-8) (Wu and Tinoco 1998). The truncated P5abc subdomain formed by the removal of 16 nucleotides (eight base pairs) from helix P5b has been shown to form the same secondary structure as found in the native 72-nucleotide P5abc subdomain (Cate et al. 1997). In the absence of Mg^{2+}, this structure differed from the structure determined by X-ray crystallography in the presence of Mg^{2+}. Mg^{2+}-induced folding of the subdomain as monitored by NMR revealed a secondary structure rearrangement to a folded conformation that is consistent with the crystal structure (Figure 1-9) (Wu and Tinoco 1998). These results contradict the

assumption that RNA folds first by forming secondary structure and then forming tertiary interactions.

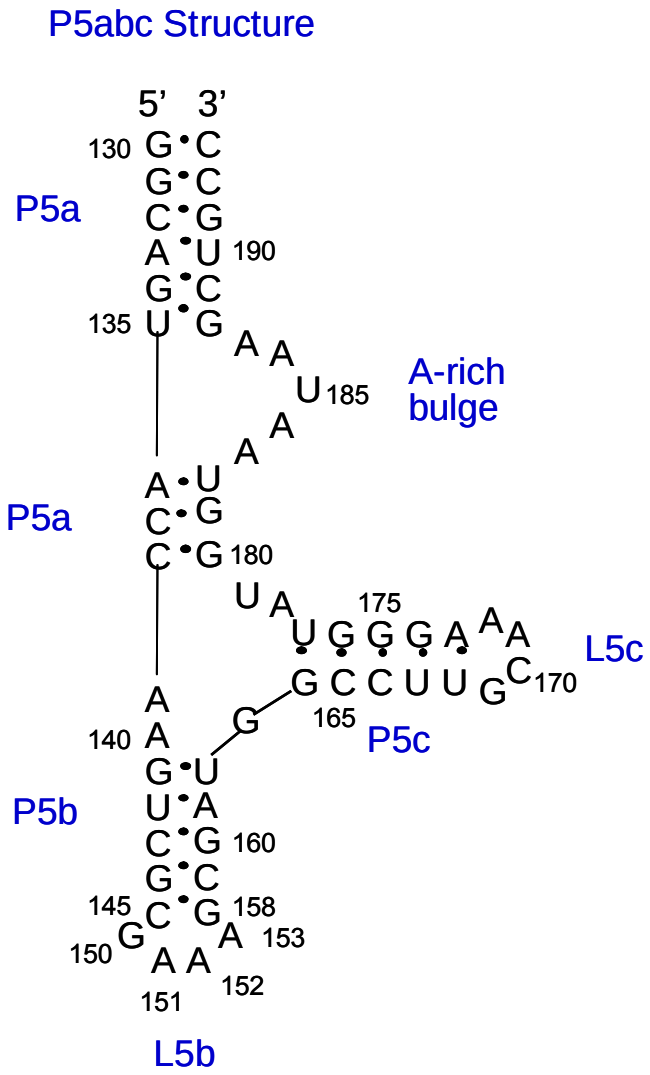

Figure 1-8. Secondary structure of the truncated P5abc subdomain determined by NMR (Wu & Tinoco, 1998).

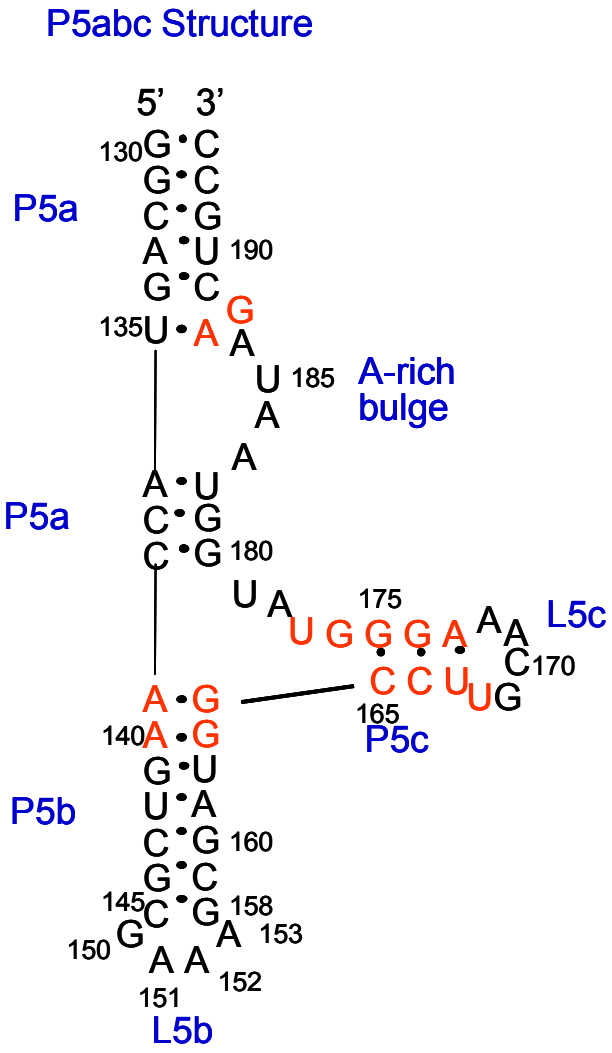

Figure 1-9. Secondary structure rearrangement of truncated P5abc in the presence of Mg^{2+}. Nucleotides that change their base pairing with metal addition are shown in red (Wu and Tinoco 1998).

Hydroxyl radical footprinting studies demonstrated that an A186U mutant of P5abc within the P4-P6 domain disrupted tertiary structure formation not only in the subdomain but throughout the entire domain (Murphy and Cech 1994). It has been proposed that the A186U mutant disrupts five hydrogen bonds with three different nucleotides in the three-way junction of the P5abc subdomain (Cate et al. 1996; Cate et al. 1997). This mutant has also been shown by native gel electrophoresis to disrupt tertiary folding of both the truncated 56-nucleotide subdomain and the entire P4-P6 domain, even at high concentrations ($>$ 50 mM) of magnesium (Cate et al. 1997). From Wu and Tinoco's NMR studies of the truncated 56-nucleotide P5abc subdomain, the imino proton spectrum of A186U in the absence of Mg^{2+} is identical to that of wild type P5abc. These results indicate that A186U and P5abc have identical secondary structures in 10 mM Na^{+} (Wu and Tinoco 1998). The addition of Mg^{2+} to A186U caused little change in its imino proton spectrum, indicating the A186U mutant does not fold into the same tertiary structure as wild type P5abc and the secondary structure of A186U does not change in the presence of Mg^{2+} (Wu and Tinoco 1998).

Tertiary structure formation in the truncated P5abc subdomain in the presence of Mg^{2+} has also been observed by mechanical force experiments that monitor the reversible unfolding of single RNA molecules (Liphardt et al. 2001). Two kinetic barriers are observed in the mechanical unfolding of P5abc in the presence of Mg^{2+}. These barriers were not observed in a P5abc mutant with

helix P5c and the A-rich bulge deleted. Therefore the kinetic barriers were assigned to tertiary interactions in P5abc (Liphardt et al. 2001).

Previous studies indicate that a cluster of metal ions are required for the P5abc subdomain to undergo tertiary folding and that this subdomain is an essential part of the group I intron from *Tetrahymena thermophila*. In this thesis, the properties of this uncommon metal ion core and its influence on the truncated P5abc subdomain structure have been investigated. Paramagnetic Mn^{2+} and EPR spectroscopy were utilized to investigate the number and affinities of divalent metal ions bound to the P5abc subdomain. The influence of monovalent ions on divalent ion binding to the subdomain was also investigated. A spectroscopic signature of metal ion core formation in both the P5abc subdomain and the entire P4-P6 domain was determined from EPR microwave power saturation studies. Phosphorothioate substitutions along with P5abc mutants and EPR spectroscopy were utilized to investigate the folding pathway of the P5abc subdomain. Thermal denaturation techniques were employed to study the unfolding of wild type and mutant P5abc in the absence and presence of divalent ions. Since it has been proposed that the metal ion core stabilizes the structure of the subdomain in order to drive the folding pathway of the P4-P6 domain and ultimately the rest of the ribozyme (Cate et al. 1997), an enthalpic contribution for formation of this ion core was determined by differential scanning calorimetry studies. Finally, thermal melting of P5abc fragments and mutations

were utilized to further investigate the metal-dependent folding pathway of the P5abc subdomain.

CHAPTER II

MATERIALS AND METHODS

RNA Synthesis and Purification

The 56-nucleotide wild type P5abc and the A186U mutant of P5abc used in this research were initially synthesized by in vitro transcription with T7 polymerase (Milligan and Uhlenbeck 1989). The 73-nucleotide DNA strand (56-nucleotide plus the added 17-nucleotide primer sequence) and the 17-nucleotide primer DNA strand were purchased from Gene Technologies Laboratory at Texas A&M University. The DNA was purified on a 20% denaturing polyacrylamide gel. The gel pieces containing the DNA were electroeluted with 1 X Tris-Borate-EDTA (TBE) buffer (0.09 M Tris, 0.002 M EDTA) until the gel pieces no longer contained DNA as determined by UV-shadowing. The solution was then concentrated using Centricon YM-3 (Amicon) tubes, ethanol precipitated, dried and resuspended in ~100 μL 1 X Tris EDTA (10 mM Tris, 1 mM EDTA (TE) buffer. The primer-template used for the transcription reactions was made in a 1:1 ratio at a 5 μM final concentration in the 1 X TE buffer. The primer-template was annealed at 90 ^{o}C for 2 minutes, cooled on ice, and stored at –20 ^{o}C until further use.

Transcription reactions contained 1 X transcription buffer (400 mM Tris, 50 mM DTT, 10 mM spermidine, 0.10 % v/v Triton X-100, pH 8.1), 0.5 μM primer-template, 4mM nucleotide triphosphates (NTP's), 20 mM $MgCl_2$, 80 mg/mL polyethylene glycol (PEG), and 0.07 mg/mL T7 RNA polymerase.

Transcription reactions were placed in a 37 ^{o}C water bath for 6 hours. The reactions were quenched with 20% formamide, purified on 20% polyacrylamide gels and electroeluted as described above. The RNA was then dialyzed with dialysis tubing (MWCO 5000) against the appropriate buffer for at least 72 h with five reservoir changes at 4 °C. The RNA was concentrated (Centricon-3, Amicon), ethanol-precipitated, dried, and resuspended into autoclaved water to form a stock solution. Concentrations were determined by UV absorbance at 260 nm and RNAs were stored at -20 °C until use.

The following RNAs were also purchased from Dharmacon Research (Boulder, CO) and deprotected before purification: wild type P5abc, A186U mutant, P5abc Fragments (P5a, P5b, and P5c), P5abc phosophorothioates (P5abc A186 PS and P5abc A171 PS) and the P5abc modifications (P5abc P5a mod, P5abc P5b mod and P5abc P5c mod). To deprotect the RNA the tubes were centrifuged to ensure the RNA pellet was at the bottom of the tube, and then 400 μL of 2'-deprotection buffer (Dharmacon) was added to each tube. After completely dissolving the RNA pellet by pipetting up and down the solution is vortexed for 10 seconds. Lastly the tube is incubated at 60 ^{0}C for 30 minutes and allowed to cool until an equal volume of formamide is added to the samples before purification. The oligonucleotides were purified as described above. Concentrations were determined by UV absorbance at 260 nm and all RNAs were stored at -20 °C until use.

Plasmids (pUC19) containing the P4-P6 DNA sequences were obtained from the lab of Professor Jennifer Doudna, Department of Biochemistry and Molecular Biology, University of California, Berkeley. The plasmid DNA was purified using a Qiagen Plasmid Maxi Kit and cleaved with BsaI restriction enzyme. The DNA was transcribed using the MegaScript in vitro transcription kit (Ambion) containing T7 polymerase. The 160 nucleotide P4-P6 RNA was purified on a 6% polyacrylamide gel and electroeluted as described above. The RNA was then dialyzed with dialysis tubing (MWCO 5000) against the appropriate buffer for at least 72 h with five reservoir changes at 4 °C. The RNA was concentrated (Centricon-3, Amicon), ethanol-precipitated, dried, and resuspended into autoclaved water to form a stock solution. Concentrations were determined by UV absorbance at 260 nm and P4-P6 RNA was stored at -20 °C until use.

Spectroscopic Techniques

Mn^{2+} EPR Spectroscopy

Room temperature electron paramagnetic resonance (EPR) spectroscopy can be utilized to quantitate the number of Mn^{2+} bound per biomolecule (Cohn 1954). Paramagnetic Mn^{2+} is a useful spectroscopic probe for Mg^{2+} in the P5abc subdomain, since both divalent ions have been observed to bind in the metal ion core (Juneau et al. 2001). In aqueous solution free Mn^{2+}, $Mn(H_2O)_6^{2+}$, possesses octahedral geometry and is highly symmetric. $Mn(H_2O)_6^{2+}$ is high spin with 5 unpaired electrons yielding an electron spin of 5/2 (S = 5/2) and a

nuclear spin of 5/2 (I=5/2). When $Mn(H_2O)_6^{2+}$ is placed in a magnetic field and excited with microwaves allowed transitions between energy levels with $\Delta m_s = 1$ and $\Delta m_i = 0$ can be observed. The combination of the S = 5/2 and the I = 5/2 values for $Mn(H_2O)_6^{2+}$ generate 30 possible transitions. However, in most cases, the Mn^{2+} ion has high symmetry and the transitions between the $\pm$ 1/2, $\pm$ 3/2 and $\pm$ 5/2 spin states are degenerate yielding 6 observed transitions (Figure 2-1 (a)). At room temperature, the EPR spectrum of $Mn(H_2O)_6^{2+}$ results in a six line EPR spectrum, centered at g = 2, and separated by 90 G.

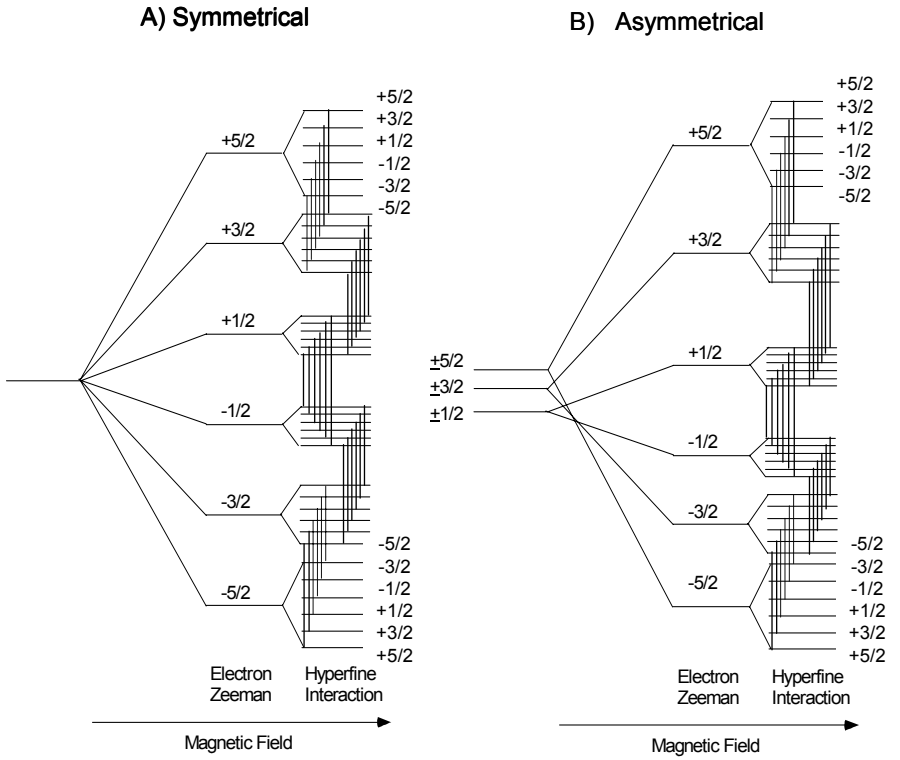

Figure 2-1. Mn^{2+} energy level splitting diagram. A) Representation of the electron spin energy levels for Mn^{2+} in a symmetrical environment with degenerate spin states. B) Representation of the electron spin energy levels for Mn^{2+} in an asymmetrical environment with nondegenerate spin states.

Upon binding to a biomolecule, the symmetry of the Mn^{2+} decreases, resulting in an increased zero field splitting. Therefore the ± 1/2 , ± 3/2 and ± 5/2 spin states are no longer degenerate (Figure 2-1 (b)). Also, an increase in rotational correlation time (τ_c) is observed upon Mn^{2+} binding to a biomolecule. Together these changes cause the room temperature Mn^{2+} EPR signal to broaden and become undetectable (Cohn 1954). The decrease in signal amplitude can then be quantitated and used to calculate the number of Mn^{2+} per RNA (Figure 2-2). The number and affinity of Mn^{2+} ions bound to the hammerhead ribozyme were determined previously in our lab (Clardy et al. 1998; Hunsicker and DeRose 2000).

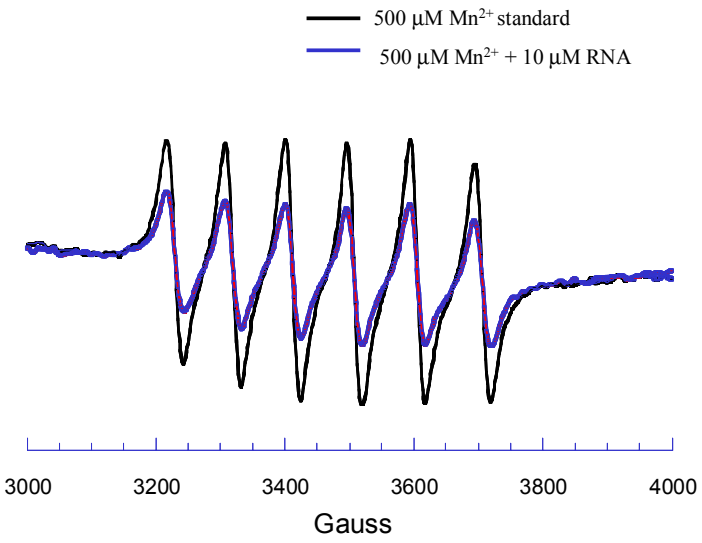

Figure 2-2. Mn^{2+} EPR spectra of Mn^{2+}-P5abc compared with a Mn^{2+} standard. The difference in intensity is quantitated to measure Mn^{2+} bound to the RNA.

These Mn^{2+} titration experiments were used to determine the number and affinity of Mn^{2+} ions binding to the P5abc subdomain, the P5abc mutants and the P4-P6 domain. The data were fit to equation 2-1 assuming a simple model of j classes of independent, non-interacting sites. Each type of site has a population of n_i identical sites, each of which has a dissociation constant of $K_{d,i.}$

$$[Mn^{2+}_{bound}]/[RNA] = \sum_{i=1}^{j} n_i[Mn^{2+}_{free}]/(K_{d,i} + [Mn^{2+}_{free}]) \qquad [2\text{-}1]$$

The cooperativity of Mn^{2+} binding to a biomolecule can be obtained from the Mn^{2+} EPR titration experiments under various NaCl concentrations. The data can be plotted as the log of free Mn^{2+} versus the number of Mn^{2+} bound per RNA and fit for the Hill coefficient (n_H) (Sclavi et al. 1997).

$$[Mn^{2+}_{bound}]/[RNA] = (K_a\,[Mn^{2+}_{free}]^{nH})/(\,1 + K_a\,[Mn^{2+}_{free}]^{nH}) \qquad [2\text{-}2]$$

Room Temperature Mn^{2+} EPR Titration Experiments

Samples were prepared with the oligonucleotides in 5 mM TEA buffer at pH 7.8 and concentrations of 5, 30 and 100mM NaCl, heating to 90º C for 90 seconds and cooling on ice for 30 min. After cooling, divalent metal ($MnCl_2$ Sigma™) was added from metal stocks made daily for each experiment to minimize metal-hydroxide formation over time. X-band EPR equipped with house N_2 was carried out at room temperature with a Bruker EMX spectrometer and TE_{102} cavity. EPR measurements were taken using 75 µl samples in capillary tubes with final RNA concentrations of 10 µM. Mn^{2+} EPR intensities

were measured at a microwave power of 0.2mW, 26G modulation amplitude, and 7.3G/s scan rate. An average of three independent measurements was obtained for each sample.

EPR Measurements of Mn^{2+} Displacement by NaCl

Samples were prepared with the oligonucleotides in 5 mM TEA, pH 7.8 with variable concentrations of NaCl from 5 to 140mM NaCl and then heating to 90º C for 90 seconds and cooled on ice for 30 min. The 75 µL samples were placed in a capillary tube containing a final RNA concentration of 10 µM and the Mn^{2+} concentration was held constant at 1mM. The room temperature X-band EPR experiments were carried out as described above. Addition of competing Na^+ to a biomolecule causes an increase in signal due to the Mn^{2+} being released from the biomolecule which can be quantitated. The competition data were fit to equation 2-3, which assumes a 1:1 Mn^{2+} displacement by the competing metal (Feig et al. 1999).

$$[Mn^{2+}_{bound}]/[RNA] = \sum n_j(1-[M]/(K_{d\ app,\ j} + [M])) \qquad [2\text{-}3]$$

where $[Mn^{2+}_{bound}]/[RNA]$ is the number of Mn^{2+} bound per RNA at [M] added competing Na^+, j is the number of types of sites, n is the total number Mn^{2+} ions displaced over the titration, and $K_{d\ app}$ is an apparent dissociation constant of the competing Na^+ in the presence of Mn^{2+}. An assumption is made that at an infinite concentration of Na^+ the number of Mn^{2+} bound is zero.

EPR Microwave Power Saturation Studies

Mn^{2+} EPR microwave power saturation studies provide a tool to investigate cluster formation in biomolecules. The microwave power at half saturation, $P_{1/2}$, is proportional to $1/(T_1T_2)$, where T_1 is the spin-lattice relaxation time and T_2 is the spin-spin relaxation time (Brudvig 1995; Galli et al. 1996). Therefore, as the spin relaxation times become shorter, there will be an increase in the microwave power required to saturate the signal. The value for $P_{1/2}$ was determined from a plot of the log $(S/P^{1/2})$ versus log of P and fit to the following equation using KaleidaGraph software:

$$\log (S/P^{1/2}) = \log (K) - (b/2)\log[1 + (P/P_{1/2})] \qquad [2\text{-}4]$$

Where S is the signal amplitude, P is the microwave power, K is a constant, $P_{1/2}$ is the microwave power at half saturation, and b is the inhomogeneity parameter (Galli et al. 1996). The inhomogeneity parameter can have a value from 1 (inhomogeneous) to 3 (homogeneous) (Galli et al. 1996). The plot of this data results in two linear regions. When $P << P_{1/2}$, log $(S/P^{1/2})$ will be constant and equal to log (K); when $P >> P_{1/2}$ the plot will have a slope of –b/2. These linear regions will intersect at $P = P_{1/2}$ (Brudvig 1995; Galli et al. 1996).

The presence of dipolar interactions has been observed to enhance spin relaxation (Hirsh et al. 1992; Galli et al. 1996). A through-space dipole-dipole interaction between spins occurs when two paramagnetic species are close to one another (Reed 1984). EPR saturation measurements of a paramagnetic species frozen in glass will have a random distribution of molecular orientations

in the magnetic field. The magnitude of the dipolar relaxation enhancement will depend on the distance between the slow and the fast relaxing spin (Hirsh et al. 1992; Galli et al. 1996). There will be a random but fixed orientation of the spins with respect to the static magnetic field. Therefore the dipolar interaction results in a distribution of spin-relaxation times (Galli et al. 1996).

In microwave progressive power saturation experiments, the distribution of T_1 values are observed as a distribution of $P_{1/2}$ values (Hirsh et al. 1992; Galli et al. 1996). The plot of the log ($S/P^{1/2}$) versus log P will result in the two linear regions as mentioned above. However, with an increase in the dipolar enhanced power saturation the intersection of the two linear regions, where $P = P_{1/2}$, will change. The increase in the value for $P_{1/2}$ will depend on the magnitude of the dipolar interaction (Galli et al. 1996).

Another indication of an increase in dipolar interactions is a decrease in the b value or inhomogeneity parameter (Galli et al. 1996). Brudvig and coworkers found that for dipolar-enhanced power saturation data, the fit for the b value was less than 1, which is the inhomogeneous broadening limit (Galli et al. 1996). In order to relate the inhomogeneity parameter to dipolar coupling microwave power saturation data were simulated with enhanced dipolar interactions. In cases where the dipolar interaction was small the b value obtained from the fit was 1. In contrast when there was a significant dipolar interaction, the value obtained for b was progressively smaller as the magnitude of the dipolar interaction increased (Galli et al. 1996). It was concluded that a

value of b < 1 was indicative of a dipolar interaction (Galli et al. 1996). This data was fit best to a b value of 0.3 indicating dipolar interactions. To eliminate three unknown variables in equation [2-4], the b value was held constant at 0.3.

X-band EPR microwave power saturation data were obtained for various RNAs over the microwave range of 0.2 to 63 mW at 10K, 100 KHz field modulation, and 7.3 G/sec scan rate. The low temperature EPR experiments required an Oxford liquid helium cryostat. Each 75 μL sample contained 250 μM RNA and ratios of one to ten equivalents of Mn^{2+} to RNA in a buffer containing 5mM TEA and 100mM NaCl, pH 7.8 (20% ethylene glycol). Samples of Mn^{2+} in buffer (5mM TEA, 100mM NaCl, pH 7.8, 20% ethylene glycol) were also used for comparison.

Fe(II)-EDTA –Dependent Hydroxyl Radical Footprinting

Hydroxyl radical footprinting is a technique that permits high resolution mapping of protected regions of RNA (X. D. Wang and Padgett 1989). Hydroxyl radicals cleave RNA independent of the base sequence allowing resolution of the protected regions at the single nucleotide level (Tullius and Dombroski 1986; X. D. Wang and Padgett 1989). In the presence of an oxygen source and a reducing agent, solvent-based Fe(II)-EDTA initiates a free radical reaction that attacks the sugar moiety of a nucleic acid backbone and ultimately results in strand scission (Hertzberg and Dervan 1984; Tullius and Dombroski 1985; Tullius and Dombroski 1986; X. D. Wang and Padgett 1989).

$$[Fe(EDTA)]^{2-} + H_2O_2 \rightarrow [Fe(EDTA)]^{1-} + OH^- + {}^{\bullet}OH$$

Riboses protected from cleavage are solvent inaccessible. Hydroxyl radical footprinting is utilized in these studies to look for regions of protection in P5abc in the absence and presence of divalent ions. Regions of protection in the presence of divalent ions would suggest potential metal binding sites required for the proper folding of the RNA.

Reactions were performed in Professor Sarah Woodson's lab in the Department of Biophysics, Johns Hopkins University, Baltimore, MD (Deras et al. 2000). 5' ^{32}P-labeled RNA was diluted in 10 μL of 10mM sodium cacodylate, pH 7.5 and 0.1 mM EDTA (CE) (300,000 cpm/μL). A scintillation counter was used to ensure the 5' ^{32}P-labeled RNA was around 300,000 cpm/μL and constant for each sample tube. 4 μL of $MgCl_2$ or $MnCl_2$ was added up underneath the lid of the appropriate sample tubes then heated all of them for one minute at 95^{o}C. The tubes were immediately spun down in the microfuge after heating. Samples were equilibrated at room temperature (approximately 5 minutes) before adding 2μL of 10mM $(NH_4)_2Fe(SO_4)_2$ and 20mM EDTA (pH 8.0), 2μL 10mM sodium L-ascorbate, and 2 μL of 0.3% H_2O_2 (20 μL total). The 10 mM Fe(II) and the 20 mM EDTA should be mixed together just before needed. At which time, the EDTA was added, and immediately pulled a sealed vacuum on the filtration flask with the building vacuum or a good aspirator. The completely dissolved salt was light green. As a note, rust colored solutions are oxidized iron and are useless. This solution needed to be made fresh each time. Reactions were vortexed and microfuged before they were quenched after 90

seconds with 6 μL of quench solution, which contained 1 μL 100mM thiourea and 5 μL precipitation buffer (1.5 mM sodium acetate, 0.3 μg of carrier tRNA, 10mM EDTA). Three volumes of ethanol were added and the RNA was precipitated at –80^{o}C for 30 minutes. The samples were pelleted, dried and dissolved in 4 μL of formamide dye. Samples were heated to 90^{o}C for 1 minute and cooled on ice before loading on 12% polyacrylamide gel (gel size: 33 width x 42 length (cm)). The gels were run with 1 X Tris-Borate-EDTA (TBE) buffer at 15 W for approximately 3 hours. Gels were dried and exposed to Molecular Dynamics Phosphoimager screens. Gels were quantified by ImageQuant for Macintosh version 1.2.

Thermal Denaturation

UV-Vis Thermal Melting

Thermal denaturation studies were performed to determine the thermodynamic consequence of the metal ion core on the P5abc subdomain and investigate the unfolding pathway of this subdomain. Thermal melting of an ordered structure of a nucleic acid to a disorderd denatured state can be monitored by an increase in UV-Vis absorbance at 260 and 280 nm. As the ordered regions of the stacked base pairs are disrupted the UV-Vis absorbance increases, which is referred to as hyperchromicity. By monitoring the increase in absorbance with increasing temperature a melting curve can be obtained for the denaturation of the nucleic acid molecule. From this data the melting

temperature (t_m) or the temperature at which half of the base pairs are unstacked can be determined (Puglisi and Tinoco 1989).

RNA thermal denaturation experiments were carried out on a Cary 1 double-beam UV-Vis spectrometer equipped with a six-cell block and a variable temperature controller. All melts were carried out in 5mM TEA and pH 7.8 with varying concentrations of NaCl, $MgCl_2$ and $MnCl_2$. The sample concentration was 2 μM RNA unless noted. The RNA samples were prepared by heating to 90°C for 90 seconds and cooling on ice for 30 minutes. Divalent cations were then added from concentrated stock solutions in water. Samples were loaded into sealed cuvettes at room temperature, placed in the spectrometer and allowed to equilibrate to 5°C for 10 minutes before beginning the experiment. The temperature controller was ramped at a rate of 0.3 °C/min from 5 to 100 °C. Data were collected at 0.3 degree intervals as determined by a temperature probe inserted into a cuvette containing the reference buffer. Absorbance was recorded at 260 and 280 nm with increasing temperature.

Analysis of Thermal Melting Profiles

The data sets were smoothed over a 4°C window and the melting profile was presented as the derivative of absorbance with respect to temperature and plotted as a function of temperature. Thermal denaturation profiles were fit using Dr. Jon Christopher's t-melt program on a UNIX based workstation (Christopher 1998). The data were fit to a sequential unfolding model as described previously (Theimer and Giedroc 1999). This model assumes a two-

state unfolding event for each transition in which the molecule is either fully folded or fully unfolded with no intermediates. This is described by an equilibrium constant, K_i, that is a function of the enthalpy of the transition, ΔH_i, and the melting temperature for that transition, t_m as expressed in equation [2-5].

$$K_i = \exp\left((\Delta H_i^*(1/t_{m,i} - 1/T))/R\right) \qquad [2\text{-}5]$$

The partition function q describes all species in the solution at the temperature T

$$q = 1 + \left(\sum_{j=1}^{ntrans} \left(\prod_{i}^{j} K_i\right)\right) \qquad [2\text{-}6]$$

where ntrans is the total number of unfolding transitions. Z_{itrans} is the sum of the terms in which the individual transition participates.

$$Z_{itrans} = \left(\sum_{j=itrans}^{ntrans} \left(\prod_{i}^{j} K_i\right)\right) \qquad [2\text{-}7]$$

The absorbance at a given temperature is the sum over all transitions of the contribution of each transition, Z, multiplied by its amplitude, A_n, divided by the partition function for the system, q.

$$signal = \sum_{n=1}^{ntrans} A_n Z/q = \sum_{n=1}^{ntrans} \left(A_n\left(\sum_{j=n}^{ntrans} \left(\prod_{i=1}^{j} K_i\right)\right)\right)/\left(1 + \left(\sum_{j=1}^{ntrans} \left(\prod_{i=1}^{j} K_i\right)\right)\right) \qquad [2\text{-}8]$$

The derivative of the signal is calculated and equation [2-9] is actually fit.

$$\delta A/\delta T = \sum_{n=1}^{ntrans} \left(\frac{A_n \left[\sum_{j=n}^{ntrans} \left[\sum_{m=1}^{j} \left[\prod_{i=1}^{m-1} \right] \left[\prod_{i=m+1}^{j} \right] H_m K \right] \right]}{T^2} \right) \Big/ q - \left(\frac{A_n z \left[\sum_{j=1}^{ntrans} \left[\sum_{m=1}^{j} \left[\prod_{i=1}^{m-1} \right] \left[\prod_{i=m+1}^{i} \right] H_m K \right] \right]}{T^2} \right) \Big/ q^2 \Bigg)$$

[2-9]

Analysis of Divalent Cation Concentration Dependence of the Melting Profiles

The melting temperature at various divalent ion concentrations were plotted as $1/T_m$ vs. $[M^{2+}]$ (M) and fit to the equation derived by Laing et. al, 1994 (Laing et al. 1994). This model assumes an electrostatic interaction of one divalent ion for every two phosphates. This model also assumes two-state unfolding for the transition being fit. The model generates RNA-metal affinities associated with a given transition for the folded form K_f and the unfolded form K_u of the RNA (Equation 2-10) (Laing et al. 1994; Nixon and Giedroc 1998).

$$1/t_m = 1/t_o - (R/\Delta H_o)\ \ln [(0.5 + 0.5(1 + 4K_fL)^{1/2})^m/(0.5 + 0.5(1 + 4K_uL)^{1/2})^m] \qquad [2\text{-}10]$$

where t_m is the melting temperature at a given metal concentration, and K_f and K_u are the metal binding constants for the folded and unfolded forms of the RNA, L is the free metal concentration, and m is the number of phosphates participating in a given unfolding event (Laing et al. 1994). ΔH_o and t_o are the enthalpy and melting temperature of the transition in the absence of divalent ions.

Thermal Melting Profiles for the P5abc Fragments and Mutations

To check for formation of dimers in the P5abc fragments the concentration dependence of the melting temperature was determined for the optical melts of the P5a, P5b and P5c fragments. Under 2μM, 10μM and 30μM RNA concentrations the melting temperature for each fragment remained the same. Since these results indicate monomers unfolding 2μM RNA was used for the optical studies in 5mM TEA, 100mM NaCl, pH 7.8 and various Mn^{2+} concentrations. The P5abc mutation optical melts were also run with an RNA concentration of 2μM in 5mM TEA, 100mM NaCl, pH 7.8 and various Mn^{2+} concentrations. The data were fit to the same sequential unfolding model as for wild type P5abc.

Differential Scanning Calorimetry

Differential Scanning Calorimetry (DSC) can also be used to detect thermally induced unfolding transitions in nucleic acids. However, the excess heat capacity (ΔC_p) is monitored instead of the change in absorbance of the solution. ΔC_p vs. temperature is plotted in order to observe the melting profile. The area under the melting transition is equal to the transition enthalpy.

DSC data were collected on a Microcal VP-DSC in Professor David Giedroc's lab in the department of Biochemistry/Biophysics at Texas A&M University. RNA samples were dialyzed extensively against 5mM TEA, 100mM NaCl, pH 7.8 buffers and the final dialysis buffer was used for references. The RNA samples were degassed under vacuum and loaded into a pressurized

500μL sample cell with a final RNA concentration of 30 μM. Samples were equilibrated at 5 ^{o}C for 30 minutes before the temperature was ramped at a rate of 1 ^{o}C/min from 5 to 120 ^{o}C. Baseline scans were run under the same conditions using final dialysis buffer in both the reference and sample cells. Calorimetry data were analyzed with the Origin program (MicroCal). The buffer baseline scan was subtracted from the raw DSC data. After baseline subtraction the data were fit to a sequential unfolding model as described (Theimer and Giedroc 1999) above with the exception that the signal A_n in Equation 2-9 is now the intrinsic molar enthalpy ΔH_n. The equation is differentiated with respect to temperature to obtain the system heat capacity, C_p (Theimer and Giedroc 1999).

Electrostatic Calculations

The electrostatic calculations were performed using a nonlinear Poisson-Boltzmann (NLPB) equation as previously described by Chin et al (Chin et al. 1999). The PDB coordinates were obtained for the P5abc subdomain from the 2.8Å crystal structure of the P4-P6 domain by Doudna and coworkers (Cate et al. 1996). The NLPB solver was obtained from A.M. Pyle's website (http://cpmcnet.columbia.edu/dept/gsas/biochem/labs/pyle/electrostatics.html). The Biopolymer module of Insight II was utilized to add hydrogen to the entire structure. Electrostatics was calculated using the NLPB equation by the program Qnifft. The structure was minimized and a phi map was generated using the rna2.crg charge set and the rna2.siz parameter file for the atomic radii (Discover Forcefield). The calculated charges generated by the NLPB solver

were mapped as electrostatic surface using SPOCK (Christopher 1998.). Parameters included a monovalent ion concentration of 0.145 M, an internal dielectric constant of 2, and an external dielectric constant of 80.

CHAPTER III

SPECTROSCOPIC INVESTIGATION OF THE METAL ION CORE IN THE P5ABC SUBDOMAIN

Introduction

Metal ions are vital to ribozyme (RNA enzyme) structure and function. In most cases, the activity of a ribozyme is directly correlated to the correct structure formation, which may be related to the requirement of metal ions. Also in some cases, evidence has been presented that metal ions directly aid in the catalytic reaction. Because of their importance for RNA structure and function, it is useful to have direct probes for metal sites in RNA. In these studies, spectroscopic properties of Mn^{2+} binding in the P5abc subdomain of the group I intron have been characterized, and a unique spectroscopic signature of metal ion core formation was observed.

The 2.8 Å resolution crystal structure of the P4-P6 domain from the *Tetrahymena* group I intron was solved by Doudna and coworkers (Cate et al. 1996). A remarkable feature of the P4-P6 domain crystal structure is the clustering of five magnesium ions in the P5abc subdomain (Figure 3-1) (Cate et al. 1996). The subdomain three helix junction protects the A-rich bulge, which, according to the crystal structure, makes a corkscrew turn to form key tertiary interactions between the helical halves of the P4-P6 domain (Cate et al. 1997) . The magnesium ions may organize the three-helix junction in order to drive the

folding pathway of the P4-P6 domain and ultimately the rest of the ribozyme (Cate et al. 1997).

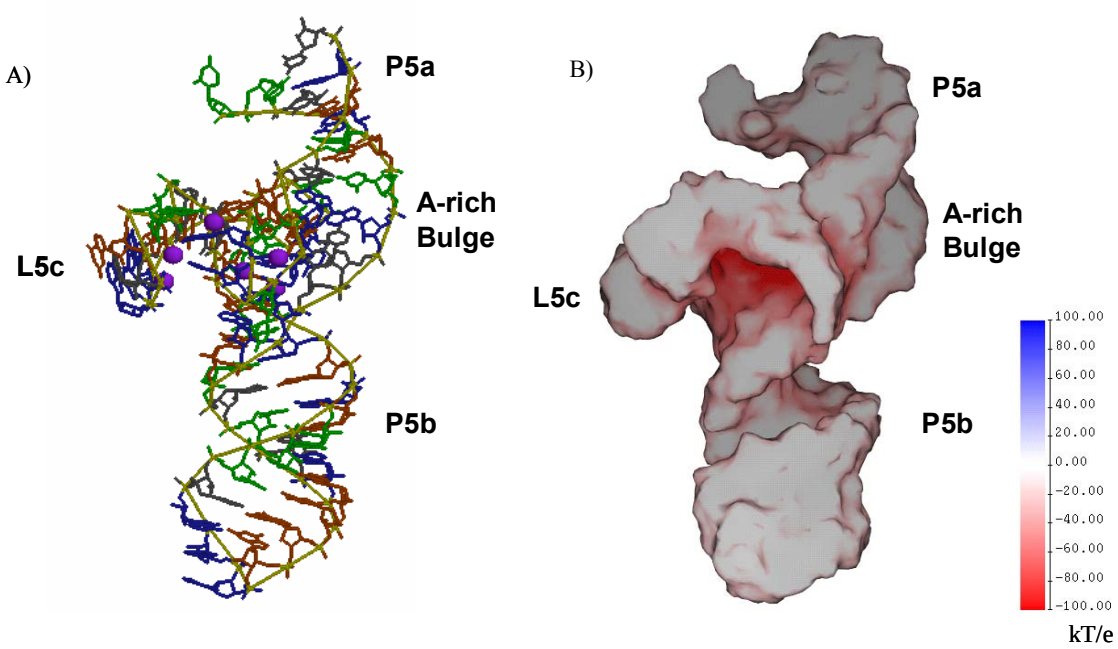

Figure 3-1. P5abc subdomain of the group I intron. A) Metal ion core found in the P5abc subdomain of the group I intron excised from the crystal structure of the P4-P6 domain (nucleotides 130-193) (PDB 1G1D). Purple spheres represent Mg^{2+} ions. B) Electrostatic surface plot of the P5abc subdomain. Regions of high negative electrostatic potential are consistent with the metal ion core.

Deleting a single nucleotide, C209, located in the P4 helix of the P4-P6 domain was shown to form a more stable tertiary structure in solution (Juneau and Cech 1999). Using this mutation a 2.25Å crystal structure of the P4-P6 domain was solved by Cech and coworkers (Juneau et al. 2001). In this crystal structure 10 Mg^{2+} ions were located in the P5abc subdomain, including the 6 Mg^{2+} ions found in the cluster from the previous 2.8Å crystal structure. The Mg^{2+} ions found in the cluster exhibited both innersphere and outersphere

coordination (Juneau et al. 2001). The majority of the magnesium ion coordination was to nonbridging phosphate oxygens. In addition, cobalt (III) hexammine and Mn^{2+} were used to substitute for Mg^{2+} in the crystal structure. Cobalt (III) hexammine was found to bind to specific sites that are not occupied by Mg^{2+}(Juneau et al. 2001). Mn^{2+} substituted for all of the Mg^{2+} ions that were innersphere coordinated to the RNA (Juneau et al. 2001). This result is consistent with Mn^{2+} preferring innersphere coordination (Feig 1999; Gesteland 1999).

To determine whether the divalent metal ions play a role in folding of the P4-P6 domain, phosphorothioate substitution experiments were utilized to disrupt the magnesium binding sites (Cate et al. 1997; Basu and Strobel 1999). Seven positions that contained a single R_p phosphorothioate substitution disrupted the Mg^{2+} dependent tertiary fold of the RNA (Cate et al. 1997). Six of these positions involved coordination to the five Mg^{2+} ions in the core of the subdomain. Results from these experiments support the hypothesis that the five Mg^{2+} ions play a role in forming the tertiary structure of the intron.

Previous studies suggest that a cluster of metal ions are required for the P5abc subdomain to undergo tertiary folding and that this subdomain is an essential part of the group I intron from *Tetrahymena thermophila*. Here, under solution conditions, the properties of this uncommon metal ion core and its influence on the truncated P5abc subdomain structure (Figure 3-2) have been investigated. Paramagnetic Mn^{2+} and EPR spectroscopy were utilized to

investigate the number and affinities of divalent metal ions bound to the P5abc subdomain. The influence of monovalent ions on divalent ion binding to the subdomain was also investigated. A spectroscopic signature of metal ion core formation was determined from EPR microwave power saturation studies. Finally, phosphorothioate substitutions along with P5abc mutants were utilized to investigate the folding pathway of the P5abc subdomain.

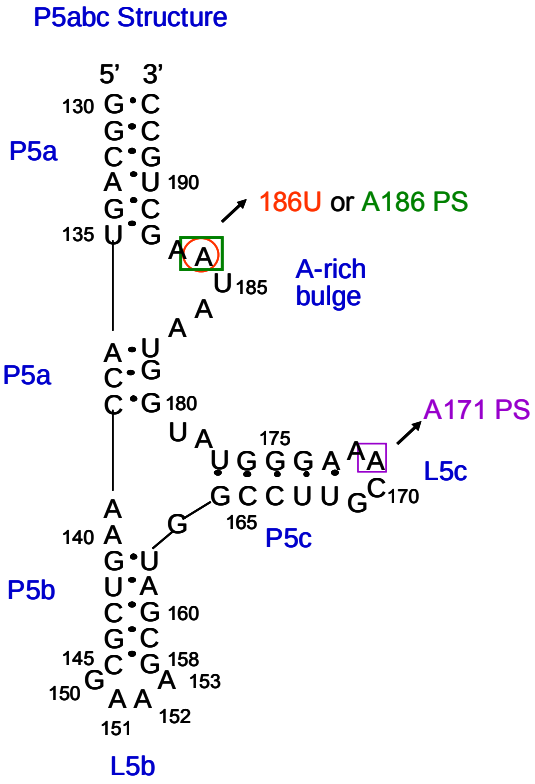

Figure 3-2. Secondary structure of P5abc. (O) An A186U mutant that does not undergo tertiary folding, (□)A186 PS, and (□) A171 PS.

Results

Electrostatic Model of the P5abc Subdomain

The structure of the P5abc subdomain contained within the X-Ray crystal structure of the P4-P6 domain (Cate et al. 1996) is shown in Figure 3-1A, where the six Mg^{2+} ions in the metal ion core are depicted as purple spheres. An electrostatic surface plot calculated for the isolated P5abc subdomain, based on the x-ray coordinates, reveals that there is a high negative electrostatic potential in the interior of the structure (Figure 3-1B). An electrostatic plot of the P4-P6 domain revealed that there were similar regions of high negative electrostatic potential in the P5abc subdomain within the P4-P6 domain (Chin et al. 1999). These results indicate the P5abc subdomain alone adopts the same conformation with high negative electrostatic potential as when it is a part of the P4-P6 domain. Comparison of the X-ray crystal structure of P5abc with the electrostatic model reveals the region of high negative electrostatic potential is consistent with the metal ion core.

Mn^{2+} Binding Affinities for the P5abc Subdomain

If the P5abc subdomain creates an unusual metal-binding pocket, it might be expected that the P5abc would exhibit high apparent affinities for Mn^{2+} ions. The relative affinities of Mn^{2+} for P5abc were determined under different NaCl concentrations from Mn^{2+} EPR titration studies. The binding isotherm for P5abc in 5 mM, 30 mM and 100 mM NaCl is shown in Figure 3-3A. In the presence of 100 mM NaCl, there are 12 ± 1.1 Mn^{2+} ion binding sites in the 56-nucleotide

P5abc subdomain. The ions bind with an average K_d of 136 ± 18 μM (Table 3-1). The following 13-mer duplex, (5' UGCGAGCGAGCGC 3'/ 3' ACGCUCGCUCGCG 5'), in 100 mM NaCl binds 3.5 ± 0.3 Mn^{2+} ions with an average apparent K_d of 147 ± 33 μM (Vogt 2003). The 13-mer duplex was used as a control model that has no expected unusual metal-binding properties. The Mn^{2+} binding affinities for the13-mer duplex and the P5abc subdomain are similar, therefore the apparent affinity determined suggests that this technique measures predominately diffuse Mn^{2+} ion binding to P5abc.

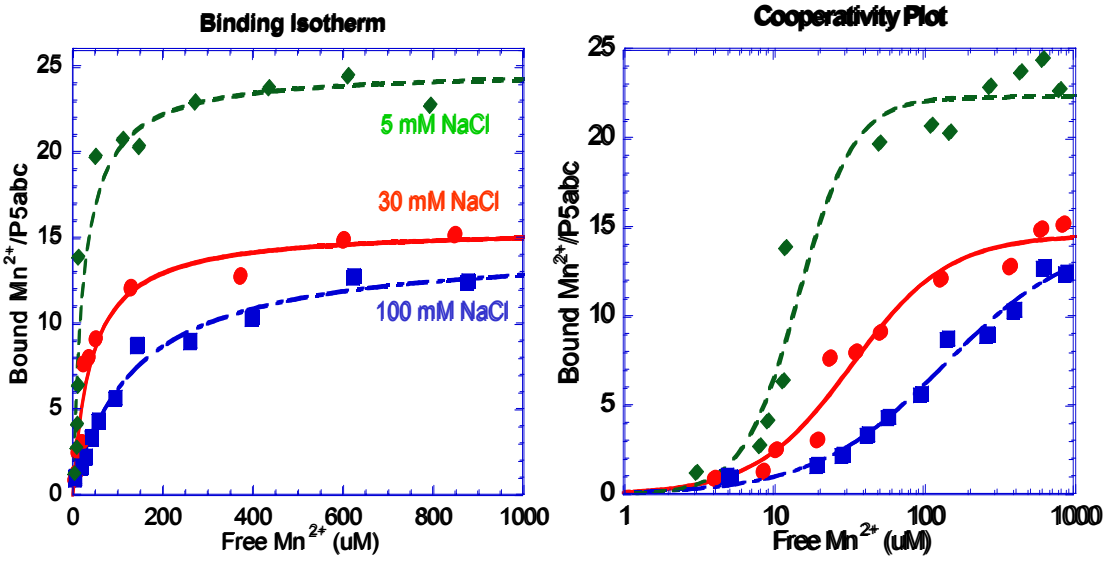

Figure 3-3. Mn^{2+} binding to P5abc measured using RT EPR spectroscopy. A) Mn^{2+} binding isotherm of P5abc with addition of NaCl: (◆) 5 mM NaCl, (●)30mM NaCl, (■)100 mM NaCl. B) Cooperativity plot of Mn^{2+} binding to P5abc. Each sample contained 10μM RNA in 5mM TEA, pH 7.8.

As expected the number of Mn^{2+} ions that bind to the subdomain decreases with an increase in NaCl concentration, and the relative affinities also decrease (Figure 3-3A, Table 3-1). These studies indicate that the loss of the majority of Mn^{2+} binding sites with an increase in NaCl concentration is likely due to diffuse-charge screening interactions that can be satisfied with either monovalent or divalent cations.

The cooperativity of Mn^{2+} binding to P5abc under the different NaCl concentrations was also determined from the Mn^{2+} EPR titration data. The cooperativity plot for Mn^{2+} binding at each NaCl concentration is shown in Figure 3-3B where the data were fit to a Hill coefficient (n_H) value (Table 3-1). In 5mM NaCl, Mn^{2+} binding to P5abc is slightly cooperative ($n_H = 1.5 \pm 0.3$) indicating the binding of one Mn^{2+} may promote the binding of the next Mn^{2+} ion. However with an increase in NaCl concentration up to 100 mM, Mn^{2+} binding to P5abc is no longer cooperative ($n_H = 1.0 \pm 0.2$).

Table 3-1. Relative affinities of Mn^{2+} for the P5abc subdomain in different NaCl concentrations.

NaCl (mM)	*n*	K_d (μM)	n_H
5	24.8 ± 1.4	23.6 ± 6.1	1.5 ± 0.3
30	15.6 ± 1.8	41.2 ± 7.7	1.4 ± 0.3
100	12.4 ± 0.7	136.4 ± 18.0	1.0 ± 0.2

Samples contained 10 μM RNA in 5mM TEA, pH 7.8.

Mn^{2+} Displacement by NaCl Measured by Competition Studies

In 0.1 M Na^+, P5abc binds approximately 12 Mn^{2+} with an apparent affinity of 130 μM and no apparent cooperativity. Although diffuse ion binding is expected to be of lower affinity than chelated ions, it is possible that the relative affinities are closer than the factor of ~ 1/10 required to distinguish sites through fitting binding isotherms. To further distinguish diffuse Mn^{2+} ion sites from chelated ions, an EPR NaCl competition experiment was performed. With an increase in NaCl concentration, the Na^+ ions compete for the diffuse Mn^{2+} ion sites revealing the chelated Mn^{2+} ion sites bound to the subdomain, which are more resistant to displacement by Na^{2+}. In this study, the Mn^{2+} ion and RNA concentration were held constant at 1 mM and 10 μM respectively while increasing concentrations of NaCl (5 to 140 mM) were added to the samples. The number of Mn^{2+} binding sites at each NaCl concentration was calculated. The competition data shown in Figure 3-4 were fit to two types of Na^+ sites. The first type of site displaced 14.6 ± 4.3 Mn^{2+} sites with a $K_{d\ app}$ of 17.9 ± 2.0 mM. The second type of site displaced 9.5 ± 1.7 Mn^{2+} sites with a $K_{d\ app}$ of 750.3 ± 54.3 mM (Table 3-2). In the first type of site, Na^+ easily displaces diffuse Mn^{2+} ions, whereas the other Mn^{2+} sites are more resistant to competition from Na^+. The ~9 Mn^{2+} sites that are not easily displaced by Na^+ may be associated with the metal ion core depicted in the crystal structure.

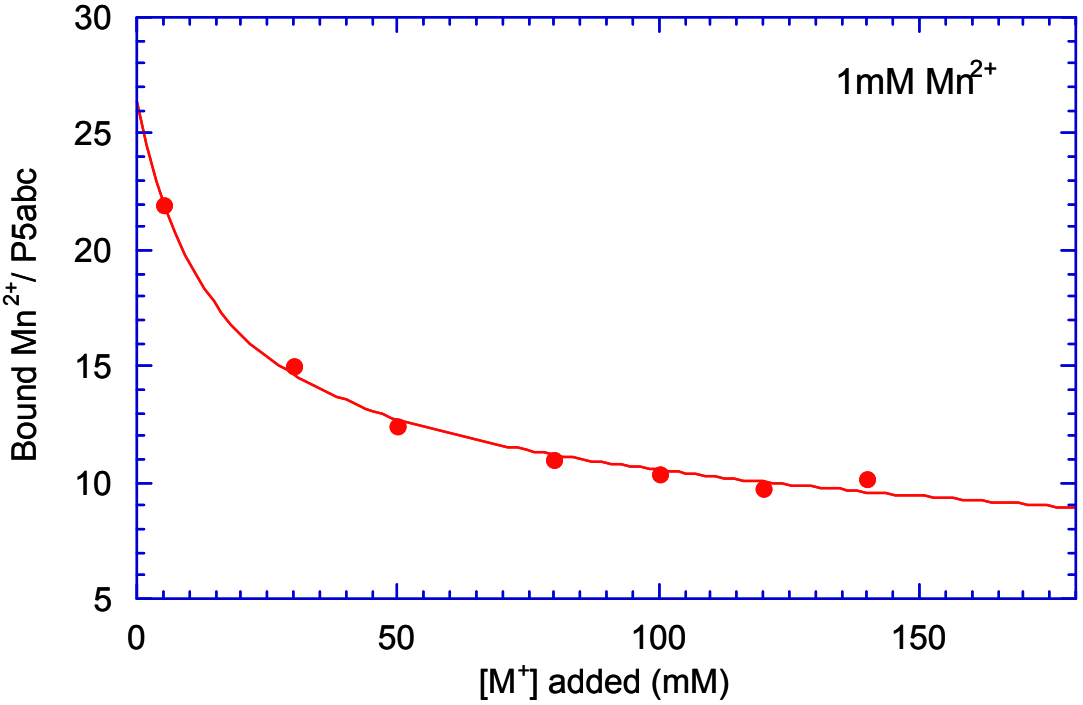

Figure 3-4. Influence of added NaCl on Mn^{2+} binding to the P5abc subdomain in 1 mM Mn^{2+}. Each sample contained 10 μM RNA, 1 mM Mn^{2+}in 5 mM TEA, pH 7.8.

Table 3-2. NaCl EPR competition for Mn^{2+} binding to the P5abc subdomain.

Site	K_{comp} (mM)	Number of Mn^{2+} displaced
1	17.9 ± 2.0	14.6 ± 4.3
2	750.3 ± 54.3	9.5 ± 1.7

Samples contained 10μM RNA, 1mM Mn^{2+} in 5mM TEA and increasing NaCl concentrations (5 to 140mM), pH 7.8.

Mn^{2+} Binding to the A186U Mutant

The A186U mutant of the native P5abc subdomain has been shown by both Fe-EDTA cleavage experiments and solution NMR experiments not to form

tertiary structure in the presence of Mg^{2+} and Mn^{2+} ions (Latham and Cech 1989; Celander and Cech 1991; Murphy and Cech 1994; Y. H. Wang et al. 1994; Wu and Tinoco 1998). In the absence of divalent ions, the A186U mutant and wild type P5abc have the same secondary structure (Figure 3-2). A comparison of the Mn^{2+} EPR binding isotherms for the A186U mutant and wild type P5abc in the presence of 100mM NaCl are shown in Figure 3-5. There are 24.5 ± 2.0 Mn^{2+} ions bound to the A186U mutant with an apparent K_d = 231.9 ± 48.2 μM (Table 3-3). In comparison to wild type P5abc, the A186U mutant binds an average of 12 more Mn^{2+} ions and has a slightly weaker apparent affinity. Since the A186U mutant does not undergo tertiary structure formation, these data are consistent with Mn^{2+} binding to an unfolded structure where the negative phosphate backbone would be more accessible to neutralization.

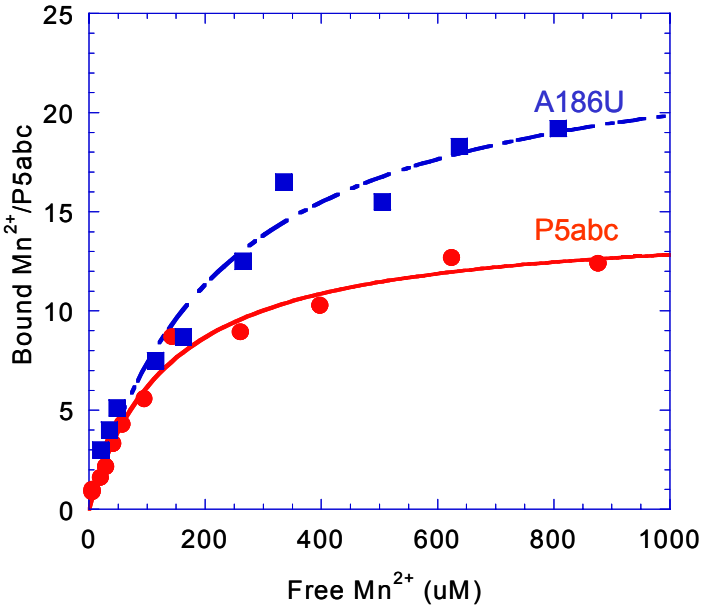

Figure 3-5. Mn^{2+} binding isotherms for (•) P5abc and (■) A186U. Each sample contained 10μM RNA in 5mM TEA, 100mM NaCl, pH 7.8.

Table 3-3. Relative affinities of Mn^{2+} for the P5abc subdomain, A186U mutant and P5a fragment.

RNA	*n*	K_d (μM)
P5abc	12.4 ± 0.7	136.4 ± 18.0
A186U	24.5 ± 2.0	231.9 ± 48.2
P5a	7.8 ± 0.8	363.4 ± 76.2

Samples contained 10 μM RNA in 5mM TEA, 100mM NaCl pH 7.8.

Spectroscopic Signature of Metal Ion Core Formation in the P5abc Subdomain

Formation of the metal ion core in the P5abc subdomain predicts that the metal ions will be in close proximity, with inter-Mn^{2+} distances of ~ 6-15Å. To search for a spectroscopic signature for the metal ion core formation in the P5abc subdomain, low temperature Mn^{2+} EPR microwave power saturation experiments were performed. In the case of paramagnetic Mn^{2+}, the neighboring ions should enhance relaxation and increase the microwave power required to saturate the EPR signal. The microwave power required at half saturation ($P_{1/2}$) is determined to monitor this enhancement in relaxation.

The $P_{1/2}$ values characterizing Mn^{2+} EPR signal saturation were determined for 1 to 10 equivalents of Mn^{2+} added to P5abc. Figure 3-6A represents microwave power saturation data for a Mn^{2+} standard in comparison with 2 and 6 equivalents of Mn^{2+} added to 1 P5abc. The Mn^{2+} standard contained only 1 mM Mn^{2+} in 5 mM TEA, 100 mM NaCl, pH 7.8 buffer which is equal to four equivalents of Mn^{2+} used in this studies. A small increase in $P_{1/2}$ is

observed when comparing $2Mn^{2+}$: 1P5abc to the Mn^{2+} standard. The Mn-RNA samples contain 0.25 mM to 2.5 mM Mn^{2+}. It is important to note that the $P_{1/2}$ values for 0.25 to 2.5 mM Mn^{2+} standards containing no RNA did not change in these studies (data not shown). A rather large increase in $P_{1/2}$ is observed when comparing 6 Mn^{2+}: 1 P5abc to either 2 Mn^{2+}:1 P5abc or the Mn^{2+} standard. The $P_{1/2}$ values are plotted against equivalents of Mn^{2+} in Figure 3-7. As observed in Figure 3-7, there is an abrupt increase in $P_{1/2}$ upon addition of 4- 5 equivalents of Mn^{2+} ions to P5abc (Table 3-4). The $P_{1/2}$ value remains constant upon addition of further equivalents of Mn^{2+}. These data suggest that the rise in $P_{1/2}$ is due to formation of the metal ion core. To test this, the A186U mutant of P5abc, which has been shown not to form tertiary structure, was studied under the same conditions. As predicted, the EPR microwave power saturation experiments on the A186U mutant do not reveal a dramatic increase in the $P_{1/2}$ value (Table 3-4, Figure 3-6B, 3-7). This suggests that the P5abc microwave power saturation results are indicative of metal ion core formation.

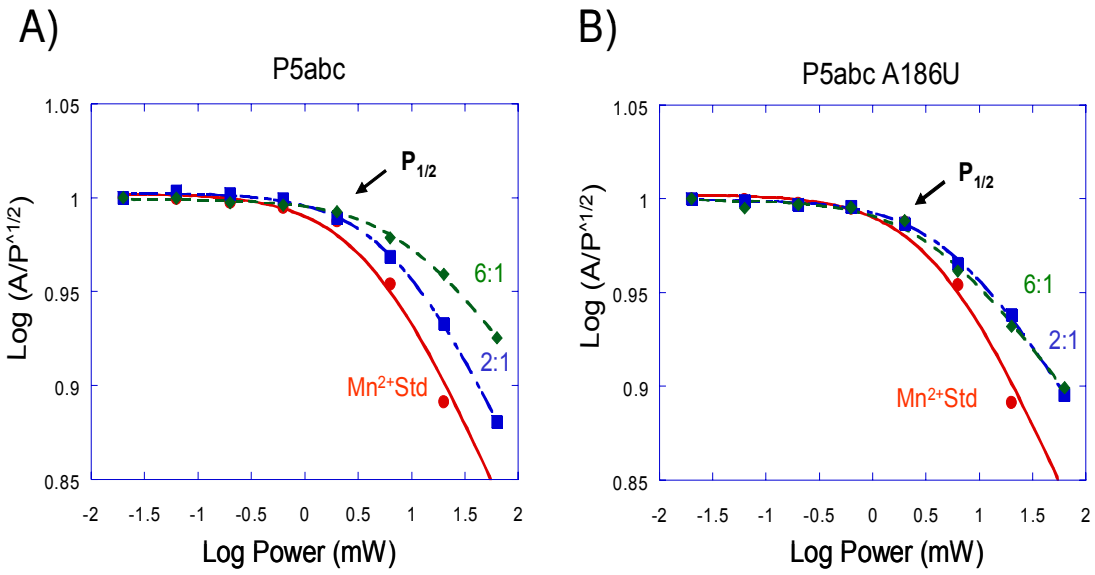

Figure 3-6. Example of EPR microwave power saturation behavior for Mn^{2+} bound to P5abc WT and the A186U mutant. A) Comparison of the power saturation of a Mn^{2+} standard, 2 equivalents of Mn^{2+}: 1 P5abc and 6 equivalents of Mn^{2+}:1 P5abc. There is an increase in the $P_{1/2}$ value when 6 equivalents of Mn^{2+} are added to the P5abc subdomain. B) Comparison of the power saturation of a Mn^{2+} standard, 2 equivalents of Mn^{2+}: 1A186U mutant and 6 equivalents of Mn^{2+}:1A186U mutant. There is no dramatic change in the $P_{1/2}$ value upon addition of Mn^{2+} to the A186U mutant.

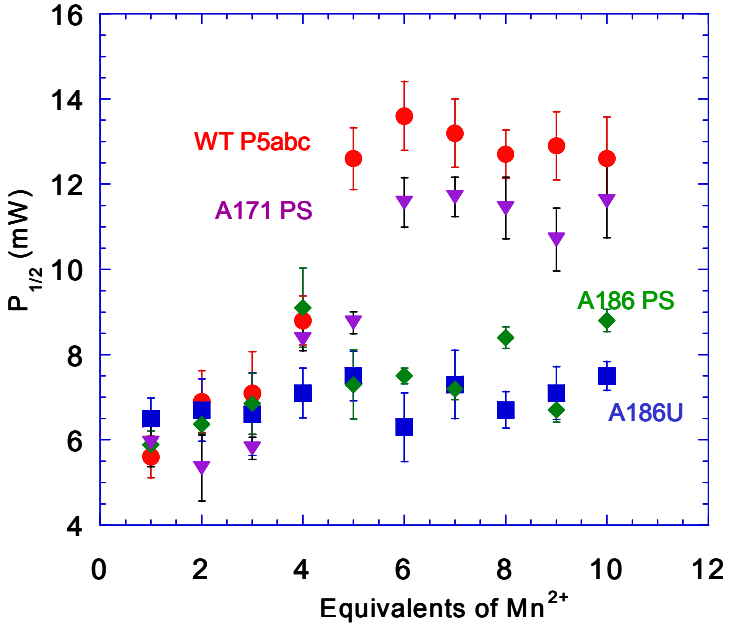

Figure 3-7. Results of microwave power saturation studies of P5abc. $P_{1/2}$ values for (•) WT P5abc, (■) A186U mutant, (♦) A186 PS and (▼) A171 PS. Each sample contained 250 μM of RNA, 20% ethylene glycol, 5 mM TEA, 100 mM NaCl , pH 7.8. X-band EPR was run at 10K.

Table 3-4. $P_{1/2}$ obtained from microwave power saturation studies.

$P_{1/2}$ (mW) values for different equivalents of Mn^{2+}

RNA	1	2	3	4	5	6	7	8	9	10
P5abc	5.6 ± 0.5	6.9± 0.7	7.1 ± 1.0	8.8 ± 0.6	12.6 ± 0.7	13.6 ± 0.8	13.2 ± 0.8	12.7 ± 0.6	12.9 ± 0.8	12.6 ± 0.9
A186U	6.5 ± 0.5	6.7 ± 0.7	6.6 ± 0.9	7.1 ± 0.6	7.5 ± 0.7	6.3 ± 0.8	7.3 ± 0.9	6.7 ± 0.4	7.1 ± 0.6	7.5 ± 0.3
A186 P-S	5.9 ± 0.3	6.4 ± 0.2	6.9 ± 0.7	9.1 ± 0.9	7.3 ± 0.8	7.5 ± 0.2	7.2 ± 0.3	8.4 ± 0.4	6.7 ± 0.3	8.8 ± 0.5
A171 P-S	5.9 ± 0.6	5.3 ± 0.8	5.8 ± 0.3	8.4 ± 0.3	8.8 ± 0.4	11.6 ± 0.6	11.7 ± 0.5	11.4 ± 0.7	10.7 ± 0.7	11.6 ± 0.9
P5a Fragment	3.7 ± 0.6	4.9 ± 0.7	4.5 ± 0.5	5.4 ± 0.2	4.3 ± 0.3	4.5 ± 0.8	4.9 ± 0.5	5.5 ± 0.3	4.7 ± 0.6	5.1 ± 0.8

Samples contained 250 μM RNA, 5mM TEA, 100mM NaCl, pH=7.8, 20% ethylene glycol.

Also the b value or inhomogeneity parameter for all equivalents of Mn^{2+} added to the subdomain was best fit to a value of 0.3. To reduce the number of unkown values for the fit to equation [2-4] the b value was held constant at 0.3. Since the b value is less than 1, this data further represents significant dipolar interactions (Galli et al. 1996).

Mn^{2+} Binding to P5abc under Conditions of Microwave Power Saturation Studies

One possible explanation for the abrupt increase in $P_{1/2}$ values for P5abc is that the Mn^{2+} does not bind tightly under the conditions of the low temperature EPR experiment. To confirm that each equivalent of Mn^{2+} is bound under EPR microwave power saturation conditions, the Mn^{2+} room temperature EPR spectra were obtained and quantified at each Mn^{2+}: RNA concentration. The number of Mn^{2+} bound to P5abc and the A186U mutant at each Mn^{2+} concentration is shown in Figure 3-8. For the wild type P5abc, all equivalents of Mn^{2+} are bound to the subdomain through the 8 equivalents (2mM) tested. However, for the A186U mutant, only the first five Mn^{2+} ions appear bound at 250uM RNA. This is expected based on the weaker apparent affinities measured for Mn^{2+} binding to the A186U mutant.

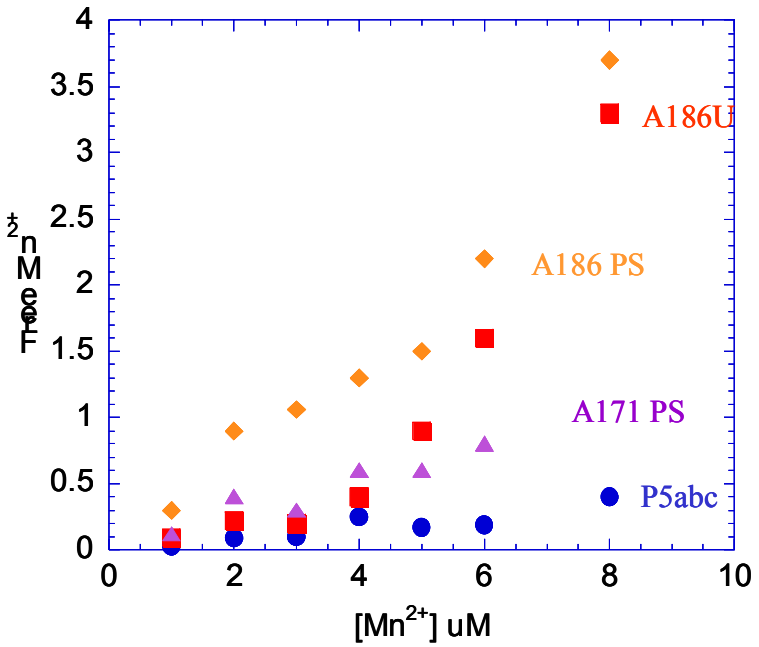

Figure 3-8. Number of free Mn^{2+} per equivalent of Mn^{2+}added to 250 μM RNA. (●) wild type P5abc, (■) A186U mutant, (♦) A186 PS, (▲) A171 PS. Each sample was in 20% ethylene glycol, 5mM TEA, 100mM NaCl, pH 7.8.

Investigation of Mn^{2+} Dependent Folding Pathway of P5abc

Although it seems likely that the rise in microwave $P_{1/2}$ occurs due to Mn^{2+} clustering in P5abc, the molecular origin of this phenomenon are not well-defined. A proposed metal dependent folding model for the P5abc subdomain is shown in Figure 3-9. The proposed metals, m_a through m_f, are based on the 6 Mg^{2+} or Mn^{2+} ions found in the metal ion core of the structure of the P5abc

subdomain contained within the X-ray crystal structure of the P4-P6 domain (Cate et al. 1996; Juneau et al. 2001). In this model the first two (m_a and m_b) metals bind in the A-rich bulge, the next two metals (m_c and m_d) bind in helices P5b and P5c and then the last two metals (m_e and m_f) bind between helices P5a and P5c and between P5c and P5b completely forming the metal ion core. Therefore, in this model it is proposed that the large increase in $P_{1/2}$ value observed after 5 equivalents of Mn^{2+} are added to wild type P5abc, the binding of metals m_e and m_f, is due to complete formation of the ion core. However, it is also possible that the large increase in $P_{1/2}$ could be due to binding of the two closest ions (m_A and m_B) to P5abc. The two closest divalent metal binding sites are found in the A-rich bulge bound to A183, A184, A186 and A187 (Figure 1-7) (Cate et al. 1996; Juneau et al. 2001), and the following studies have been utilized to investigate this possibility.

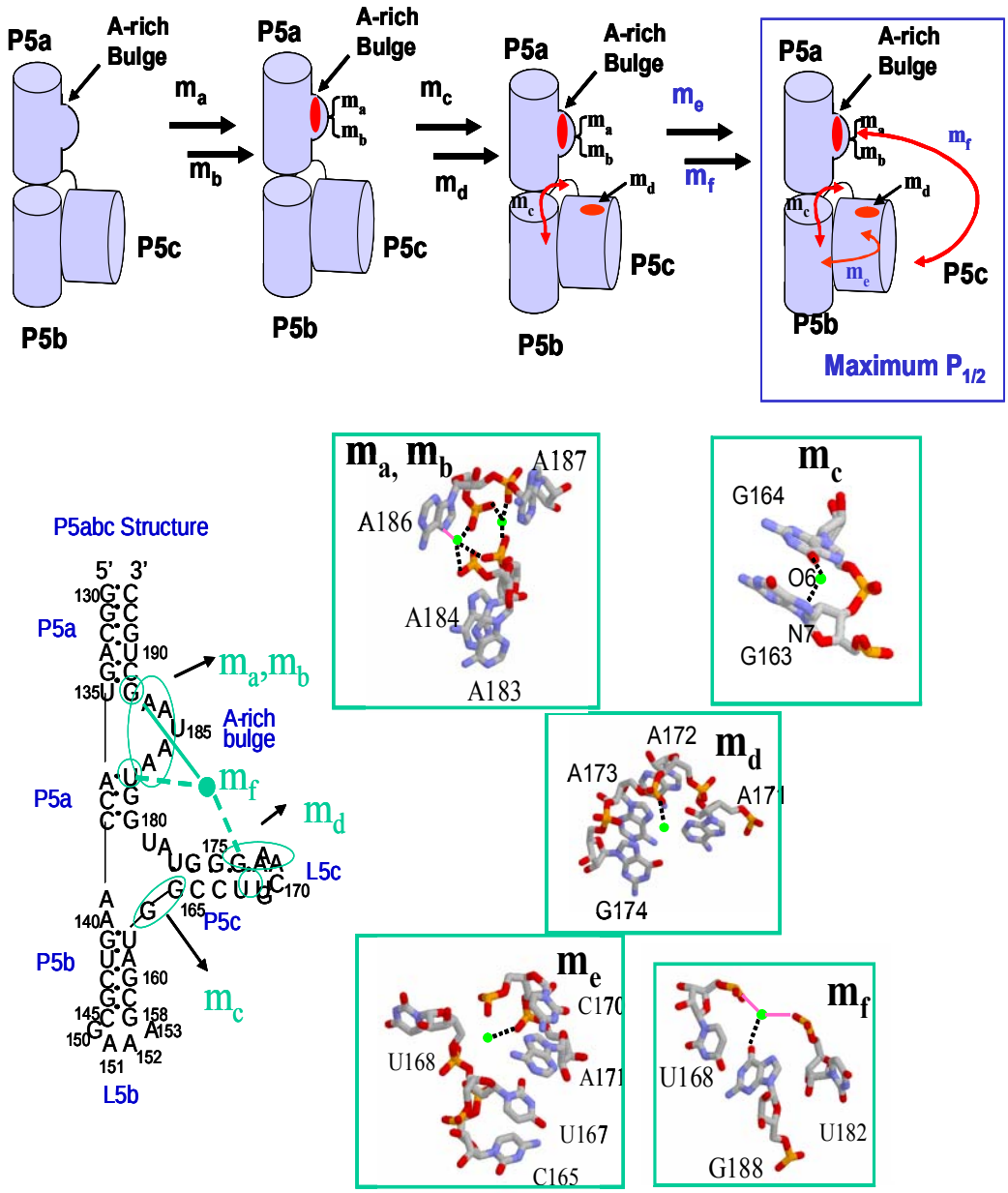

Figure 3-9. Proposed metal-dependent folding model for the P5abc subdomain.

Phosphorothioate Substitutions of P5abc

Mn^{2+} rescue experiments with phosphorothioate substitutions (PS) in the P5abc subdomain of the P4-P6 domain have been previously performed to identify divalent metal binding sites required for P5abc folding (Basu and Strobel 1999). In order to investigate whether results from the microwave power saturation studies are indicative of metal ion core formation in the P5abc subdomain or if the large increase in $P_{1/2}$ is due to the two closest ions binding in the A-rich bulge, $P_{1/2}$ values from microwave power saturation studies of samples containing a PS substitution at A186 (A186 PS) or A171 (A171 PS) were determined. Studies were performed on a mixture of PS diastereomers in both cases. Previous results from Basu and Strobel report that folding of an A186 PS could not be rescued with an addition of up to 0.3mM Mn^{2+}, however folding of an A171 PS could be rescued with Mn^{2+} (Basu and Strobel 1999). Results from microwave power saturation experiments of these two phosphorothioate substitutions are shown in Figure 3-7 and Table 3-4. $P_{1/2}$ values obtained for the A186 PS microwave power saturation studies remain constant, with addition of up to 10 equivalent of Mn^{2+}, and no large increase in $P_{1/2}$ is observed. These data are consistent with Mn^{2+} not being able to rescue folding of a P4-P6 domain with an A186 PS substitution. $P_{1/2}$ values obtained for the A171 PS microwave power saturation studies remain constant with an addition of up to 5 equivalents of Mn^{2+} ions and then a large increase in $P_{1/2}$ is observed after the 6^{th} equivalent of Mn^{2+} is added to the subdomain (Figure 3-7).

These data support the Mn^{2+} rescue of the A171 PS observed previously in folding studies.

Room temperature Mn^{2+} EPR spectra were also obtained for each equivalent of Mn^{2+} added to the phosphorothioate substituted P5abc and results are shown in Figure 3-8. The A186 PS behaves similarly to the A186U sample in that 4 free Mn^{2+} ions remain in 8 equivalents of Mn^{2+}. This data is consistent with Mn^{2+} being unable to rescue folding of the A186 PS P5abc and the absence of the signature of metal ion core formation in the microwave power saturation studies. The A171 PS sample shows behavior more similar to that of wild type P5abc. Overall the A171 PS sample has 1 free Mn^{2+} ion compared to all of the Mn^{2+} bound to wild type P5abc. This data is consistent with the microwave power saturation studies that indicate 6 equivalents of Mn^{2+} are required for metal ion core formation in comparison to the 5 equivalents required for wild type P5abc ion core formation.

Microwave Power Saturation Studies of the P5a Fragment

Since no increase in $P_{1/2}$ values with the addition of up to 10 equivalents of Mn^{2+} ions is observed for both the A186U mutant and the A186 PS, it is reasonable to assume that Mn^{2+} binding to A186 is involved in the large increase in $P_{1/2}$ value observed upon addition of greater than 5 equivalents of Mn^{2+} to the P5abc subdomain, which we believe suggests formation of the ion core. To further investigate the possibility that the large increase in $P_{1/2}$ is due to Mn^{2+} binding to the two closest Mn^{2+} ion sites located in the A-rich bulge (m_A and m_B)

(Cate et al. 1996; Juneau et al. 2001), microwave power saturation studies were performed on the P5a fragment of P5abc. The P5a fragment, with a UUCG tetraloop added after C138-G180 for stability (Figure 3-10A), was shown from solution NMR studies to form the same secondary structure as when it is apart of the whole P5abc subdomain (Wu and Tinoco 1998). However, studies have not been performed on the P5a fragment in the presence of divalent ions, and therefore, it is unknown whether or not divalent ions bind in the A-rich bulge of the P5a fragment.

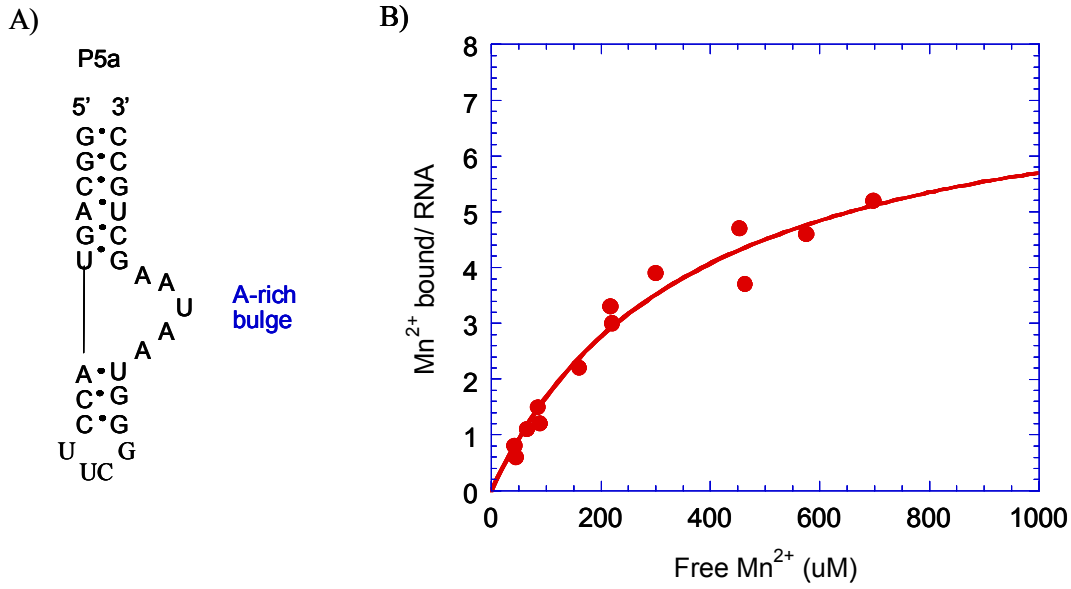

Figure 3-10. Evaluation of Mn^{2+} Binding to the P5a Fragment. A) Secondary Structure of the P5a fragment. B) Mn^{2+} Binding Isotherm of the P5a fragment (●). Each sample contained 10μM RNA in 5 mM TEA, 100 mM NaCl pH 7.8.

An investigation of Mn^{2+} binding to the P5a fragment was performed utilizing Mn^{2+} EPR titration studies and microwave power saturation studies. Results from Mn^{2+} EPR titration experiments are shown in Figure 3-10B and Table 3-3. In the presence of 100mM NaCl, the P5a fragment binds 7.8 ± 0.8 Mn^{2+} ions with an apparent K_d of 363.4 ± 76.2 μM. The association of Mn^{2+} with the P5a fragment ($K_d = 363.4 \pm 76.2$ μM) is weaker than the association of Mn^{2+} with P5abc ($K_d = 136.4 \pm 18.0$ μM). These data are consistent with diffuse Mn^{2+} binding to the P5a fragment.

Microwave power saturation studies of the P5a fragment are shown in Figure 3-11. Upon the addition of 1 through 10 equivalents of Mn^{2+} to 1 P5a fragment the $P_{1/2}$ value remains constant (Table 3-4). In comparison to the microwave power saturation of the P5abc subdomain, the lack of increase in $P_{1/2}$ value for the P5a fragment indicates that Mn^{2+} ions are not binding close to each other in the P5a fragment. However Mn^{2+} EPR titration studies indicate divalent ion binding to the P5a fragment. As a result we can not dismiss the proposal that the large increase in $P_{1/2}$ value observed after 5 equivalents of Mn^{2+} are added to P5abc is due to the two closest ions binding last in the A-rich bulge.

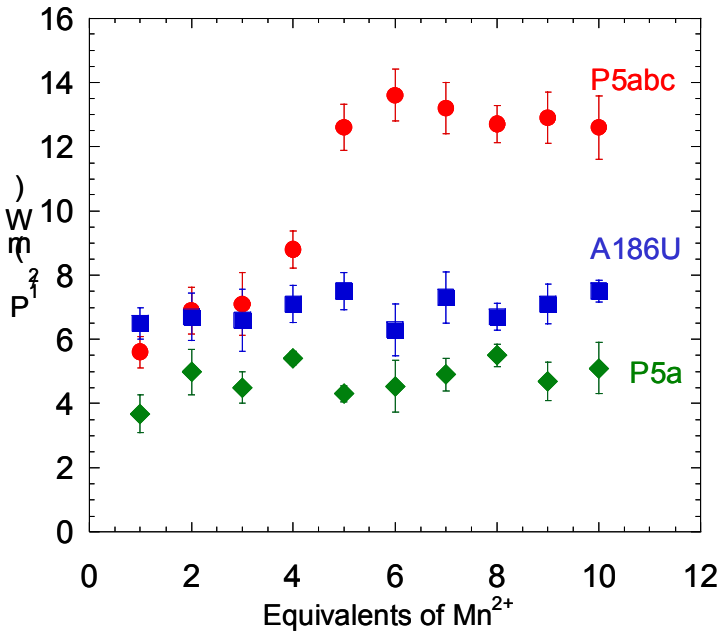

Figure 3-11. Microwave power saturation behavior of P5a fragment. (●) WT P5abc, (■) A186U mutant and (♦) P5a fragment. Each sample contained 250 µM RNA in 5mM TEA, 100mM NaCl, pH 7.8 buffer. X-band EPR was run at 10K.

Discussion

X-ray crystal structures of the P5abc subdomain of the P4-P6 domain reveal that P5abc contains a metal ion core consisting of 6 Mg^{2+} or Mn^{2+} ions (Cate et al. 1996; Juneau et al. 2001) . However, does the P5abc subdomain fold around a metal ion core under solution conditions? Are divalent ions necessary to bind to P5abc or can monovalent ions fulfill this requirement? Mn^{2+} binding to P5abc under solution conditions was investigated using various EPR techniques. Mn^{2+} EPR binding titrations were utilized to determine the number and affinity of metal binding sites to P5abc at different NaCl concentrations. In the presence of 100 mM NaCl, the room temperature Mn^{2+} EPR binding

isotherms indicate that 12 Mn^{2+} ions bind non-cooperatively with an affinity of K_d = 136 μM to the P5abc subdomain. However, when an increase in NaCl concentration competes with these Mn^{2+} binding sites, 9.5 Mn^{2+} sites remain. These 9 sites may be associated with the metal ion core occupied either with site bound Mg^{2+} or Mn^{2+} observed in both crystal structures (Cate et al. 1996; Juneau et al. 2001).

Low temperature EPR microwave power saturation studies indicate that after 5 equivalents of Mn^{2+} are added to P5abc, the ions are in close proximity to each other. This is observed by the large increase in the $P_{1/2}$ value. Upon the addition of Mn^{2+} to the nonfolding A186U mutant, no significant change in $P_{1/2}$ is observed. These data suggest that the unique spectroscopic signature results from metal ion core formation in the P5abc subdomain. In Figure 3-9 a proposed metal-folding model of the P5abc subdomain is given. In this model there is a slight increase in $P_{1/2}$ as the first four metal ions bind, but it is not until the last two metals bind and P5abc is completely folded, that the largest increase in $P_{1/2}$ is observed. In order to ensure that the low $P_{1/2}$ values observed for 1 equivalent through 4 equivalents of Mn^{2+} to P5abc were not due to a mixture of free and bound Mn^{2+}, room temperature EPR experiments were conducted to determine the number of Mn^{2+} bound to P5abc. These experiments examined Mn^{2+} binding to P5abc at 250 μM RNA concentration, and in the presence of cryoprotectant. For each concentration of Mn^{2+} from 1 equivalent through 8 equivalents all of the Mn^{2+} was bound. Since all 8

equivalents of Mn^{2+} are bound and 6 of these ions are proposed to be in the metal ion core, the tertiary folding of the P5abc subdomain may promote additional binding sites allowing two more equivalents to bind to the subdomain. However, only 5 Mn^{2+} are bound to the A186U mutant with an addition of up to 8 equivalents of Mn^{2+}. This is consistent with A186U being unable to undergo tertiary folding and prohibiting metal ion core formation and would suggest that folding of the subdomain may promote the formation of the metal binding sites.

Phosphorothioate modifications of the P5abc subdomain were utilized to investigate the Mn^{2+} dependent folding pathway. Microwave power saturation studies of the A186 PS resulted in no increase in $P_{1/2}$ value, which is consistent with the folding of the A186 PS P5abc not being rescued with Mn^{2+}(Basu and Strobel 1999). On the other hand, microwave power saturation studies of the A171 PS resulted in a large increase in $P_{1/2}$ after 6 equivalents of Mn^{2+} were added to the subdomain. This is also consistent with the folding of the A171 PS P5abc being rescued with Mn^{2+}. It appears to be a general rule that the more highly coordinated the metal ion, the less likely the possibility that the metal site will be rescued (Basu and Strobel 1999). The pro-R_p oxygen of A171 is the only ligand directly coordinated to the metal ion found in the X-ray crystal structure (Juneau et al. 2001). On the other hand the two metal ions found in the A-rich bulge in which A186 is coordinated make three innersphere contacts with the RNA (Juneau et al. 2001). Although the exact folding pathway of P5abc can not be elucidated from the phosphorothioate substitution experiments alone, these

results do indicate that Mn^{2+} binding to A186 is essential for metal ion core formation. The need for Mn^{2+} to bind A186 is also evident in the results from the microwave power saturation studies of the A186U mutant in which no increase in $P_{1/2}$ is observed and the fact that this mutant has been shown to not undergo tertiary folding.

Results from the Mn^{2+} EPR studies of the P5a fragment do not reveal Mn^{2+} ions binding close to one another because there is no change in $P_{1/2}$ value. Although the P5a fragment has been shown to fold with the same secondary structure as when it is a part of the whole P5abc subdomain (Wu and Tinoco 1998), there is no evidence that this fragment can bind Mn^{2+} ions specifically in the A-rich bulge. Therefore the exact role of the A-rich bulge residues in binding Mn^{2+} and in turn the effect they have on the large increase in $P_{1/2}$ observed after 5 equivalents of Mn^{2+} are added to the P5abc subdomain can not be determined from these experiments.

It is evident from the Mn^{2+} EPR studies of the P5abc subdomain and corresponding mutants that the wild type P5abc subdomain forms the metal ion core under solution conditions. Also the microwave power saturation studies are useful for identifying a clustering of Mn^{2+} ions. The results for wild type P5abc are consistent with the metal ion core determined from the X-ray crystal structures of the P4-P6 domain (Cate et al. 1996; Juneau et al. 2001). Microwave power saturation studies of phosphorothioate substituted P5abc reveal formation of the metal ion core with an A171 PS can be rescued with

Mn^{2+} while the A186 PS cannot. These results are consistent with previous Mn^{2+} rescue experiments (Basu and Strobel 1999). Although the exact Mn^{2+} dependent folding pathway could not be determined from these studies, it is evident that Mn^{2+} binding to A186 occur in the last stages of metal ion core formation and this nucleotide is critical for tertiary structure formation.

CHAPTER IV

THERMODYNAMIC INVESTIGATION OF THE METAL ION CORE IN THE P5ABC SUBDOMAIN

Introduction

RNA molecules consist of a highly negatively charged phosphate backbone and therefore cations are essential for RNA folding. However some cations are more effective than others at stabilizing RNA structure (Draper 2004). Optical melting and differential scanning calorimetry have been used in various studies to investigate the thermodynamic stability associated with monovalent and divalent ions in the folding of RNA structures (Draper 2004). In some cases divalent ions, in particular Mg^{2+} ions, are required for tertiary structure formation whereas high concentrations of monovalent ions cannot fulfill this requirement (Stein and Crothers 1976; Gluick and Draper 1994; Laing and Draper 1994). A particularly interesting example of the effects of divalent ions on structure is the 'metal ion core', a cluster of divalent ions that appear in the X-ray crystal structure of the P4-P6 domain of the group I intron (Cate et al. 1996). In the present studies thermal denaturation experiments were employed to investigate the folding and formation of the metal ion core in the P5abc subdomain of the group I intron.

The group I intron is a self-splicing RNA that carries out specific phosphodiester bond cleavage and subsequent splicing reactions. Group I introns mediate self-splicing by two transesterfication reactions. Splicing

requires a guanosine or a guanosine nucleotide and a divalent cation such as Mg^{2+} or Mn^{2+}. The catalytic core of the Group I intron consists of two main structural domains, base paired (P) regions P3-P9 and P4-P6 (Doudna and Cech 1995). The P3-P9 domain contains the guanosine binding site of the intron (Doudna and Cech 1995). The P4-P6 region, which consists of helical segments P4, P5 and P6, contains half of the conserved catalytic core (Y. H. Wang et al. 1994; Doudna and Cech 1995). Hydroxyl radical footprinting experiments reveal that the P4-P6 domain of the group I intron from *Tetrahymena thermophila* folds independently of the rest of the intron (Latham and Cech 1989; Celander and Cech 1991). This domain folds before the rest of the ribozyme (Murphy and Cech 1993; Zarrinkar and Williamson 1994; Doudna and Cech 1995; Downs and Cech 1996). The P4-P6 domain alone adopts the same secondary structure and tertiary fold as seen when included with the rest of the intron (Laggerbauer et al. 1994; Murphy and Cech 1994; Y. H. Wang et al. 1994).

The *Tetrahymena* P4-P6 domain also contains the P5abc subdomain, which is not near the catalytic core, but is required for efficient catalysis (Michel and Westhof 1990). The P5abc subdomain contains an A-rich bulge, a GAAA tetraloop, and a junction of three helices, P5a, P5b, and P5c (Figure 4-1). Removal of the P5abc subdomain from the intron eliminates splicing activity except for in the presence of high concentrations (25-100 mM) of Mg^{2+} (Joyce et al. 1989). The P5abc extension is a stable subdomain that can be added in

trans to restore activity (van der Horst et al. 1991). It is believed that this subdomain stabilizes the active conformation of the RNA (Cate et al. 1996).

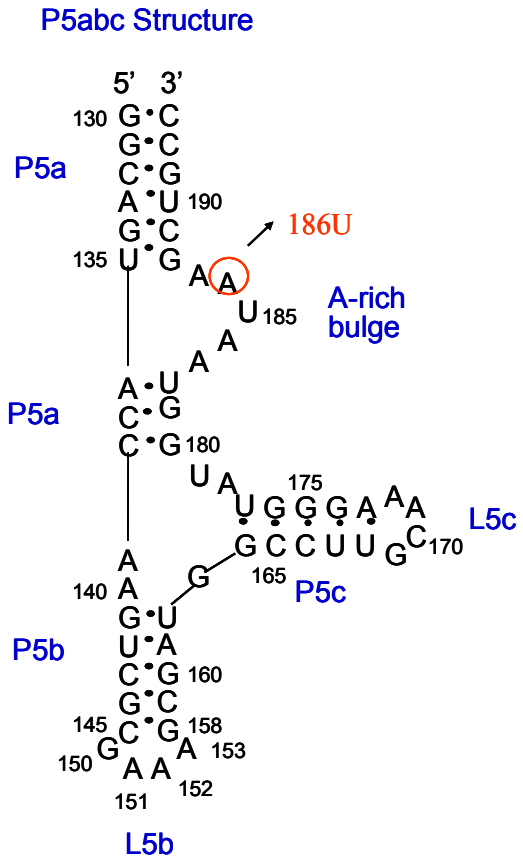

Figure 4-1. P5abc sequence used in this study. (O) An A186U mutant that does not undergo tertiary folding.

Both crystal structures of the P4-P6 domain (2.8 Å and the 2.3 Å resolution) from the *Tetrahymena* group I intron reveal a remarkable clustering of six Mg^{2+} or Mn^{2+} ions in the P5abc subdomain (Cate et al. 1996; Juneau et al. 2001). The subdomain three helix junction protects the A-rich bulge, which, according to the crystal structures, makes a corkscrew turn to form key tertiary interactions between the helical halves of the P4-P6 domain (Cate et al. 1997). The divalent ions are proposed to organize the three-helix junction in order to drive the folding pathway of the P4-P6 domain and ultimately the rest of the ribozyme (Cate et al. 1997).

To determine if the divalent metal ions play a role in folding of the P4-P6 domain, phosphorothioate substitution experiments were utilized to disrupt the Mg^{2+} binding sites (Cate et al. 1997; Basu and Strobel 1999). Seven positions that contained a single R_p phosphorothioate substitution disrupted the Mg^{2+} dependent tertiary fold of the RNA (Cate et al. 1997). Six of these positions involved coordination to five Mg^{2+} ions in the core of the subdomain. Results from these experiments demonstrate that the Mg^{2+} ions play a role in forming the tertiary structure of the intron.

The secondary structure of a truncated 56 nucleotide P5abc subdomain was determined by NMR (Wu and Tinoco 1998). In the absence of Mg^{2+}, this structure determined by NMR in solution was different than the structure determined from X-ray crystallography (Wu and Tinoco 1998). Mg^{2+}-induced folding of the subdomain as monitored by NMR revealed a secondary structure

rearrangement to a folded conformation that is consistent with the crystal structure (Wu and Tinoco 1998).

Previous studies indicate that the P5abc subdomain is an essential part of the group I intron. Both crystal structures reveal that this RNA folds around an unusual metal cluster (Cate et al. 1996; Juneau et al. 2001) and it was proposed that this metal cluster stabilizes the folded structure of the domain. However, this proposal has not been previously tested. Here both optical and differential scanning calorimetry thermal denaturation techniques are employed to investigate the thermodynamic properties of this uncommon metal ion core and its influence on the 56 nucleotide P5abc subdomain structure.

Results

Folding of the P5abc Subdomain

Previously Fe(II)-EDTA hydroxyl radical footprinting studies were performed on the native 72-nucleotide P5abc subdomain (Deras et al. 2000). Upon the addition of Mg^{2+} three regions of protection were observed in the subdomain indicating tertiary structure formation. Here Fe-EDTA hydroxyl radical footprinting studies of the 56-nucleotide P5abc were performed to ensure that the truncated subdomain undergoes the same folding (Figure 4-1). As seen in Figure 4-2 in either the presence of Mg^{2+} or Mn^{2+} three regions of protection are observed in the subdomain that are consistent with what was observed for the 72-nucleotide subdomain (Deras et al. 2000). In Figure 4-3A, an analysis of phosphorimager counts versus nucleotides is shown for the P5abc subdomain in

the presence of 2 mM Mn^{2+}. For nucleotides G163, G164, G175, G176, U177, G180 and G181 there is ~250 decrease in counts compared to the other nucleotides, which is consistent with protection in these areas in the P5abc subdomain. In the absence of divalent ions no protection was observed which coincides with the subdomain requiring divalent ions to undergo tertiary folding. The A186U mutant of the native P5abc subdomain has been shown by both Fe-EDTA cleavage experiments and solution NMR experiments not to fold in the presence of magnesium ions (Latham and Cech 1989; Celander and Cech 1991; Murphy and Cech 1994; Y. H. Wang et al. 1994; Wu and Tinoco 1998). In the absence of Mg^{2+}, wild type P5abc and mutant A186U have the same secondary structure (Figure 4-1) (Wu and Tinoco 1998). Hydroxyl radical footprinting of the A186U mutant in the truncated P5abc were also performed (Figure 4-3B). An analysis of the phosphorimager counts of the A186U mutant is also shown in Figure 4-3A. In comparison to wild type P5abc, there is little decrease in counts for any of the nucleotides. Therefore, in the absence or presence of divalent ions no protections are observed in the A186U mutant of P5abc. These results are consistent with the mutant not undergoing tertiary folding.

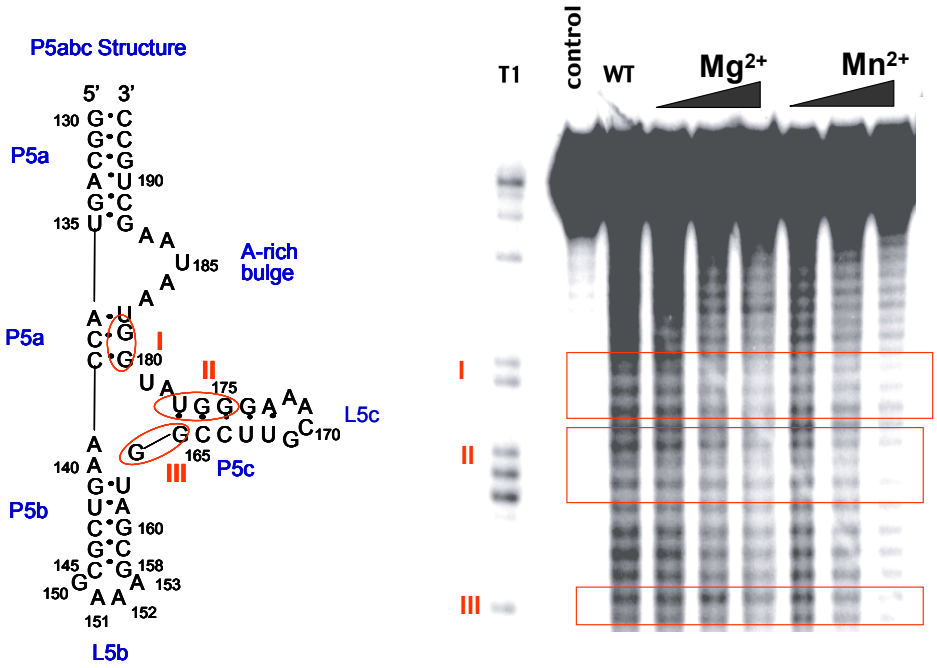

Figure 4-2. Hydroxyl radical cleavage **of the P5**abc subdomain. G ladder in lane 1 from RNase T1. Control contained **P5abc, 10mM Mg^{2+} and no oxidants. Regions of** protection in P5abc upon the addition of Mg^{2+} or Mn^{2+} are indicated in **regions I, II and III and outlined in red on the sec**ondary structure shown on the left. Increasing concentrations of Mg^{2+} **were added in the following order: 1 mM, 5 mM** and 10 mM. Increasing concentrations of Mn^{2+} were added in the **following order: 0.5 mM, 2 mM and 5 mM. Sam**ples contained 5' ^{32}P-labeled RNA (300,000 cpm/μL), 10 mM sodium **cacodylate, pH 7.5 and 0.1 mM EDTA (CE buffer).**

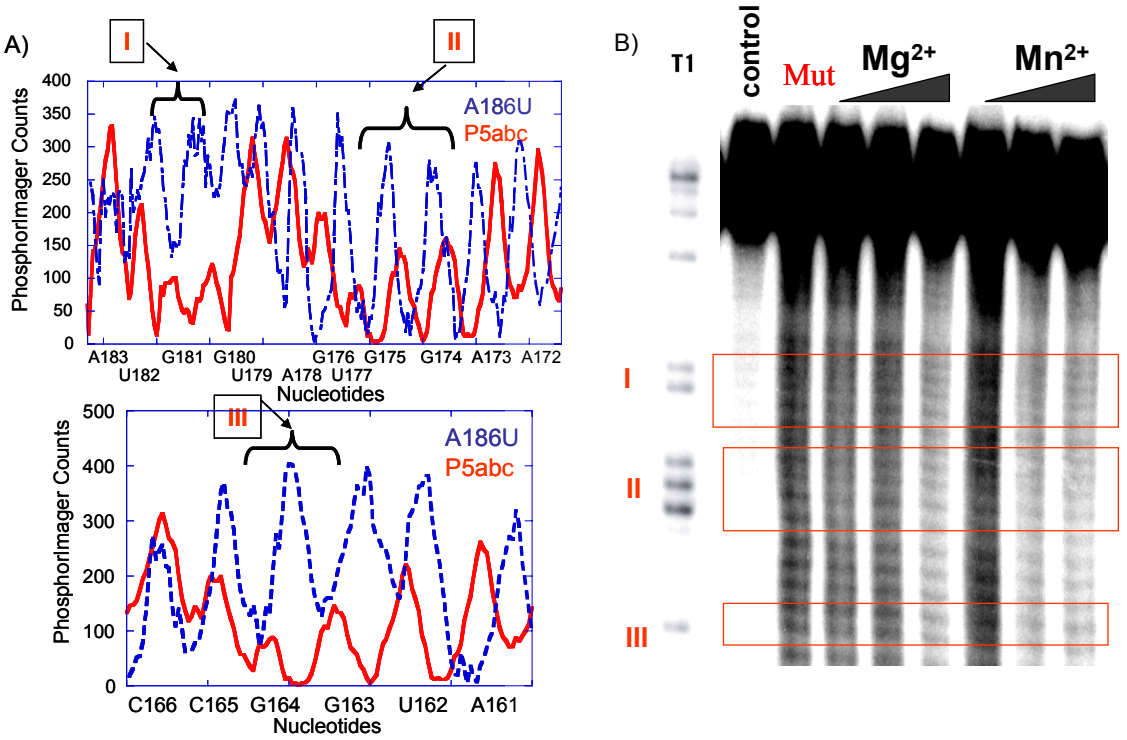

Figure 4-3. Quantitation of hydroxyl radical cleavage of P5abc and the A86U mutant. A) Plot of phosphoimager counts versus nucleotide position is shown. B) Regions of protection observed in wild type P5abc depicted by I, II and III and red boxes. G ladder in lane 1 from RNase T1. Control contained P5abc, 10mM Mg^{2+} and no oxidants. Increasing concentrations of Mg^{2+} were added in the following order: 1 mM, 5 mM and 10 mM. Increasing concentrations of Mn^{2+} were added in the following order: 0.5 mM, 2 mM and 5 mM. Samples contained 5' ^{32}P-labeled RNA (300,000 cpm/μL), 10 mM sodium cacodylate, pH 7.5 and 0.1 mM EDTA (CE buffer).

Thermal Denaturation of P5abc

Na^+ induced P5abc stabilization

Optically detected thermal denaturation experiments were used to analyze the unfolding pathway, and thermodynamic properties of the P5abc subdomain and the influence of metal ions on these properties. Thermal denaturation profiles acquired at 260 and 280 nm for wild type P5abc in the presence of various NaCl concentrations are shown in Figure 4-4. The data are shown as the derivative of absorbance with respect to temperature and are fit to

an unfolding model consisting of sequential, two-state unfolding transitions (Misra and Draper 1998; Nixon and Giedroc 1998).

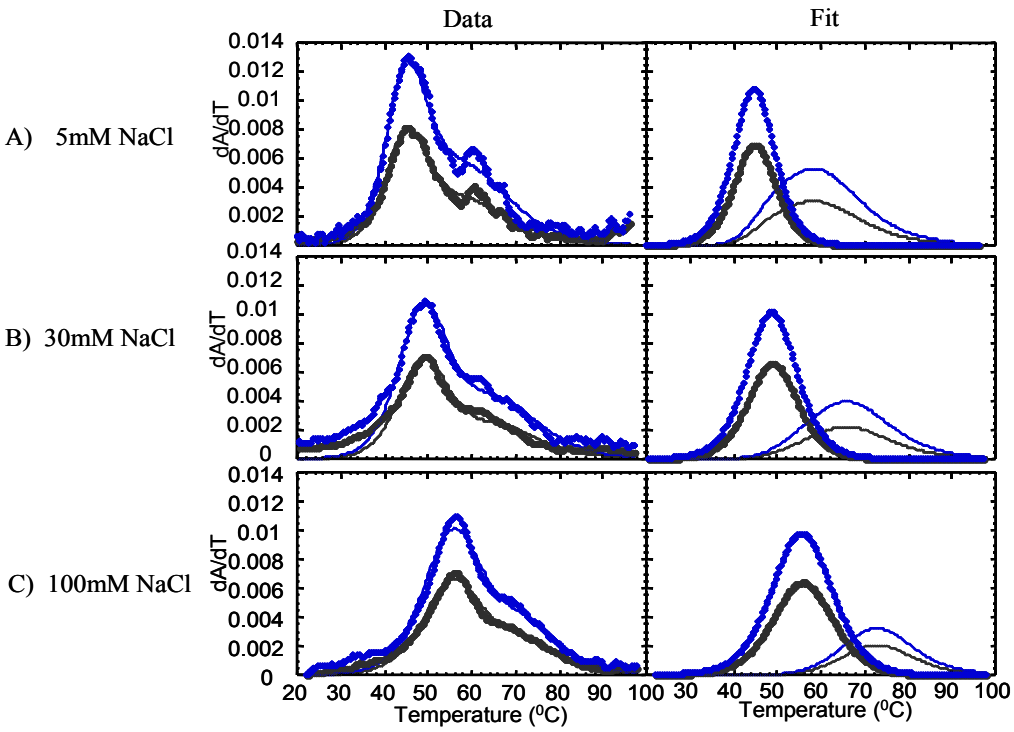

Figure 4-4. Na^+ dependence on the unfolding of P5abc. a) 5mM NaCl, b) 30mM NaCl and c)100mM NaCl. The data shown on the left were collected at two wavelengths, 260 nm (blue circles) and 280 nm (black circles). The calculated fits are shown as continuous lines through each data set. The data shown on the right represent individual transitions that make up the calculated fit to the data at each wavelength. All samples contained 2 μM RNA in 5mM TEA, pH 7.8 buffer.

The experimental data are shown on the left-hand side and are superimposed with a smooth curve, which represents the optimized nonlinear least squares fit to the unfolding model. The individual transitions that make up the total fit are shown on the right. In 5mM NaCl, P5abc unfolds in two transitions with T_{m1} = 45.0 °C and T_{m2} = 59.4 °C and an overall ΔH = 87.1 kcal/mol (Table 4-1).

Table 4-1. Thermodynamic values obtained for the sodium dependence on the unfolding of the P5abc subdomain.

RNA	Conditions	Transition	T_m (°C)	ΔH_{VH} (kcal mol^{-1})	ΔH_{total} (kcal mol^{-1})
P5abc	5mM NaCl	1 2	45.0 59.4	50.8 36.3	87.1
P5abc	30mM NaCl	1 2	49.0 66.7	53.6 34.1	87.7
P5abc	100mM NaCl	1 2	58.5 68.7	55.7 35.1	90.8

As expected with increasing concentrations of Na^+ up to 100mM there is ~ 14 °C increase in T_m for transition one and ~ 18 °C increase in T_m for transition two indicating an overall increase in the stability of the P5abc subdomain. The overall enthalpy increases to a ΔH ~90.8 kcal/mol in 100 mM NaCl, which is a 3.7 kcal/mol increase in total enthalpy for stabilization of P5abc by monovalent ions.

<u>Mn^{2+} Dependence of the Unfolding of P5abc and the A186U Mutant</u>

Comparisons of the optically detected unfolding transitions observed for wild type P5abc and the A186U nonfolding mutant in the absence and presence of divalent ions are shown in Figure 4-5. In the absence of divalent ions, in 100 mM Na^+, both wild type P5abc and the A186U mutant unfold in two similar transitions with similar T_m and ΔH values (Table 4-2). Since the A186U mutant has the same secondary structure as wild type P5abc in the absence of divalent ions these data are consistent with being due predominantly due to secondary structure unfolding.

Thermal denaturation profiles were obtained for both wild type and mutant P5abc over a wide range of Mn^{2+} concentrations (10^{-6}-0.002 M) in the presence of 100 mM NaCl. Upon the addition of low concentrations of Mn^{2+} (2 μM to 200 μM) to the wild type P5abc there is an increase in melting temperature for both transitions that are present in the absence of divalent ions, indicating that Mn^{2+} is providing additional stability to the folding of P5abc. However with increasing concentrations of Mn^{2+} (> 200 μM) the two transitions appear to collapse into one sharp transition with a maximum T_m = 73.0 ^oC and ΔH = 96.0 kcal/mol (2mM Mn^{2+}) and there is an appearance of a new broad transition with a maximum T_m = 61.9 ^oC and ΔH = 52.1 kcal/mol (2 mM Mn^{2+}) (Table 4-2, Figure 4-5). The overall enthalpy for the unfolding of P5abc in the presence of 2 mM Mn^{2+} is ΔH = 148.1 kcal/mol and the overall free energy is ΔG = 14.0 kcal/mol (Table 4-2). This is a 57.3 kcal/mol increase in ΔH and a 6.9 kcal/mol increase in ΔG compared to the unfolding of P5abc in the absence of Mn^{2+}. This increase in enthalpy and free energy is observed only in transition 2. The large increase in total enthalpy and free energy in the presence of Mn^{2+} is consistent with the requirement of divalent ions for the fully folded form of the P5abc subdomain. Since the large increase in enthalpy and free energy is due to transition 2, this transition may report tertiary structure formation.

An apparent affinity of Mn^{2+} for the folded form of P5abc can be determined by plotting $1/T_m$ vs. $[Mn^{2+}]$ and fitting the data to equation [2-10] derived by Laing et al (Laing et al. 1994; Misra and Draper 1998; Nixon and Giedroc 1998). This model assumes an electrostatic interaction of one divalent cation for every two phosphates, and two-state unfolding associated with the transition being fit (Laing et al. 1994). The apparent $K_{f,}$ K_u and K_d values obtained for both unfolding transitions for wild type P5abc in the presence of Mn^{2+} are shown in Table 4-3. Mn^{2+} dependent thermal denaturation data are shown in Figure 4-6 for P5abc in the presence of 75 μM, 300μM, and 2 mM Mn^{2+}. The dependence of the transition 1 T_m on Mn^{2+} concentration is plotted in Figure 4-7a. The apparent K_d for transition 1 is 0.23 ± 0.03 mM. Unfolding of tertiary structure is often reflected in the lowest-energy transition(Gluick and Draper 1994; Draper and Gluick 1995; Nixon and Giedroc 1998; Giedroc et al. 2000). However, the dependence of the transition 2 T_m on Mn^{2+} concentration is shown in Figure 4-7b and the apparent K_d for transition 2 is 0.08 ± 0.01 mM. Since transition 2 has a greater apparent affinity for Mn^{2+} than transition 1, it is proposed that tertiary structure formation may be involved in transition 2.

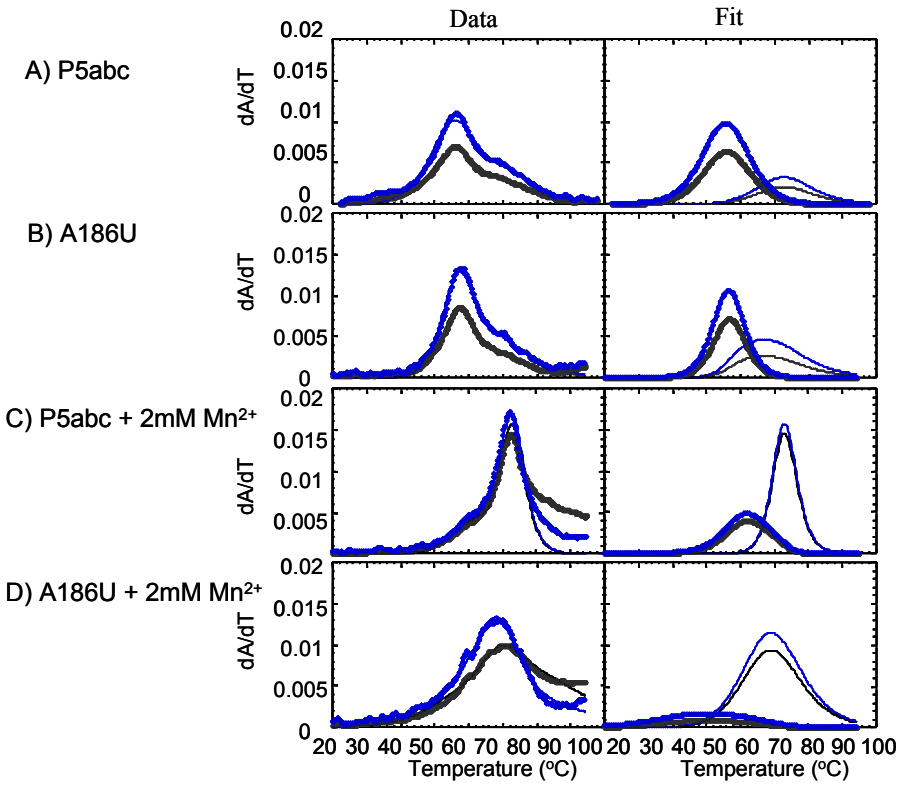

Figure 4-5. Comparison of the optical melting profiles of the P5abc subdomain and the A186U mutant. A) P5abc B) A186U mutant C)P5abc + 2mM Mn^{2+} and D) A186U + 2mM Mn^{2+} . The data shown on the left were collected at two wavelengths, 260 nm (blue circles) and 280 nm (black circles). The calculated fits are shown as continuous lines through each data set. The data shown on the right represent individual transitions that make up the calculated fit to the data at each wavelength. All samples contained 2 μM RNA in 5mM TEA, 100 mM NaCl, pH 7.8 buffer.

Table 4-2. Thermodynamic values obtained for the unfolding of the P5abc subdomain and the A186U mutant in 100 mM NaCl.

RNA	[Mn^{2+}]	Transition	T_m (°C)	ΔH_{VH} (kcal mol^{-1})	ΔH_{total} (kcal mol^{-1})	ΔG_{total} (kcal mol^{-1})	$T_{m\,cal}$ (°C)	ΔH_{cal} (kcal mol^{-1})	$\Delta H_{total\,(cal)}$ (kcal mol^{-1})	$\Delta G_{total\,(cal)}$ (kcal mol^{-1})
P5abc	0	1 2	58.5 68.7	55.7 35.1	90.8	7.1	57.0 67.5	68.1 45.3	113.4	8.3
A186U	0	1 2	56.9 68.9	55.0 35.0	90.0	6.5	55.3 65.1	68.0 46.6	114.7	7.8
P5abc A186U	2 mM 2 mM	1 2 1 2 3	61.9 73.0 59.9 69.1	52.1 96.0 29.0 58.4	148.1 87.4	14.0 7.4	63.4 72.9 59.7 69.3 82.3	65.7 95.7 36.7 51.0 32.0	161.4 119.7	14.9 11.4

Samples contained 2μM RNA, 5mM TEA, 100mM NaCl, pH 7.8.

Table 4-3. Mn^{2+} binding affinities for both P5abc and the A186U mutant in 100 mM NaCl.

RNA	Transition	K_f (M^{-1})	K_u (M^{-1})	K_d (mM)
P5abc	1	4.3×10^3	3.7×10^3	0.23 ± 0.03
P5abc	2	1.2×10^4	4.7×10^3	0.08 ± 0.01
A186U A186U	1 2	3.4×10^3 4.3×10^3	3.0×10^3 2.7×10^3	0.30 ± 0.07 0.23 ± 0.04

Samples contained 2μM RNA, 5mM TEA, 100mM NaCl, pH 7.8.

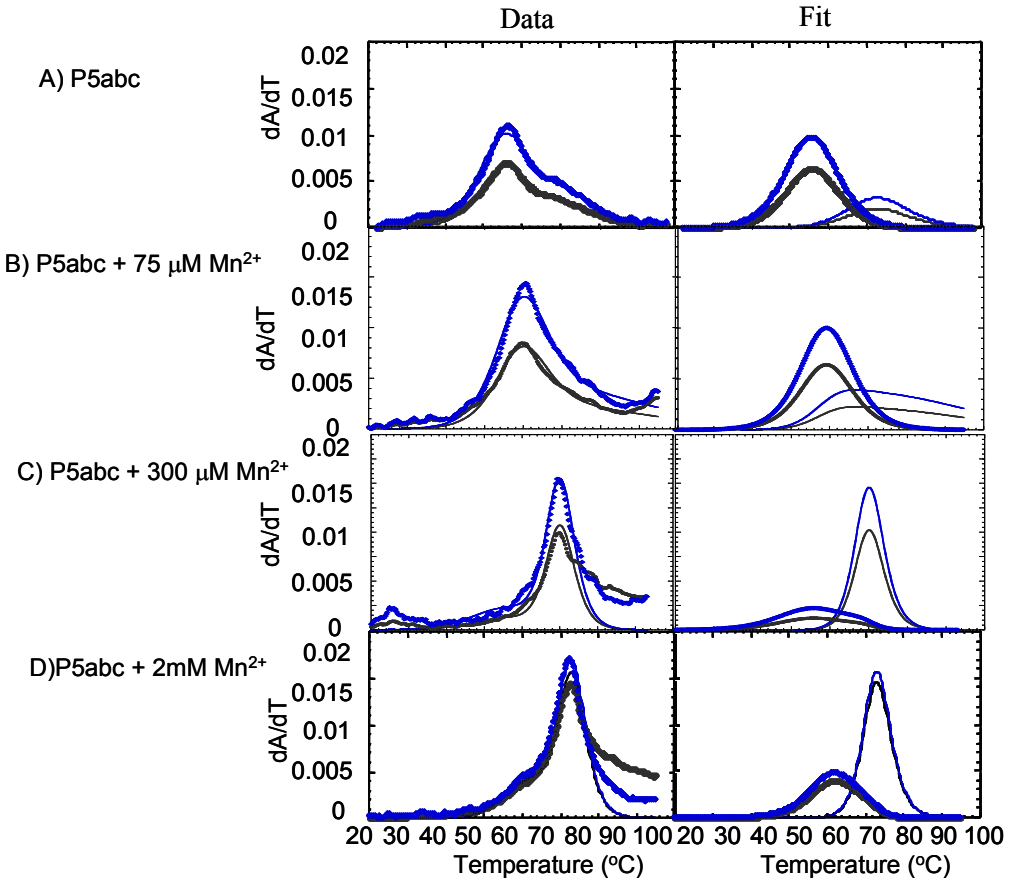

Figure 4-6. Comparison of the optical melting profiles of the P5abc subdomain upon the addition of Mn^{2+}. A) P5abc B) P5abc + 75μM Mn^{2+} C)P5abc + 300μM Mn^{2+} and D) P5abc + 2mM Mn^{2+} . The data shown on the left were collected at two wavelengths, 260 nm (blue circles) and 280 nm (black circles). The calculated fits are shown as continuous lines through each data set. The data shown on the right represent individual transitions that make up the calculated fit to the data at each wavelength. All samples contained 2 μM RNA in 5mM TEA, 100 mM NaCl, pH 7.8 buffer.

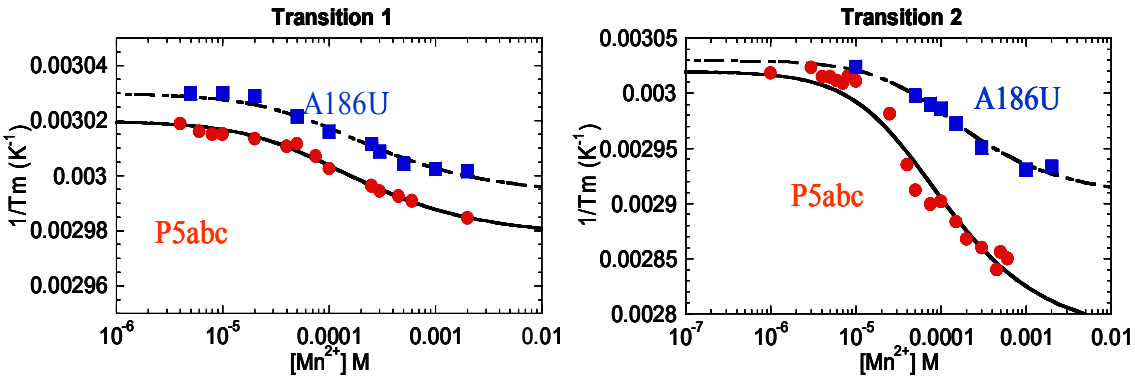

Figure 4-7. Mn^{2+} Dependence on the UV-Vis thermal denaturation of P5abc.
A) Transition 1 Mn^{2+} dependence on folding of (•)P5abc and the (◆)A186U mutant
B) Transition 2 Mn^{2+} dependence on folding of (•)P5abc and the (■)A186U mutant

To further investigate which transition is due to tertiary structure formation in P5abc the Mn^{2+} dependence on the A186U nonfolding mutant was examined. Upon the addition of low concentrations of Mn^{2+} (2 μM to 250 μM) to the A186U there is an increase in melting temperature for both transitions that are present in the absence of divalent ions, indicating Mn^{2+} is providing additional stability to the folding of A186U. However with increasing concentrations of Mn^{2+} (> 250 μM) A186U unfolds in two broad transitions with a maximum T_m = 59.9 °C and ΔH = 29.0 kcal/mol (2 mM Mn^{2+}) for transition 1 and a maximum T_m = 69.1 °C and ΔH = 58.4 kcal/mol (2 mM Mn^{2+}) for transition 2 (Figure 4-5 and Table 4-2). The overall enthalpy and free energy for the unfolding of the A186U mutant in the presence of 2 mM Mn^{2+} are 87.4 kcal/mol and 7.4 kcal/mol respectively. This is similar to the overall enthalpy of 90 kcal/mol and free energy of 6.5 kcal/mol observed for the unfolding of A186U in the absence of Mn^{2+} (Table 4-2).

The difference in total enthalpy and free energy for P5abc unfolding in the presence of 2 mM Mn^{2+} and the A186U mutant in the presence of 2 mM Mn^{2+} is 60.6 kcal/mol and 6.6 kcal/mol. Since A186U does not form tertiary structure even in the presence of Mn^{2+} the large difference in enthalpy and free energy can be attributed to metal ion core formation in wild type P5abc. The Mn^{2+} concentration dependence on A186U unfolding is plotted in Figure 4-7 for both transitions. The apparent K_d for transition 1 is 0.30 ± 0.07 mM and the apparent K_d for transition 2 is 0.23 ± 0.04 mM. Both transitions for the A186U mutant have weaker apparent affinities when compared to the wild type P5abc subdomain. However, the assignment of either unfolding transition in the P5abc subdomain in the presence of Mn^{2+} to tertiary structure formation cannot be elucidated from this data.

Determination of the Thermodynamic Consequence of the Metal Ion Core

Comparison of UV-melting profiles for P5abc and the A186U mutant in the presence of 2mM Mn^{2+} reveal a large difference in total enthalpy and free energy observed for the unfolding of the two RNAs. This large difference in enthalpy is tentatively attributed to metal ion core formation in the P5abc subdomain. To better determine the thermodynamic consequence of the metal ion core in P5abc, Differential Scanning Calorimetry (DSC) was utilized since it is a technique in which the thermodynamic values for RNA unfolding transitions can be directly detected. A comparison of the optical melts versus DSC data for wild type and mutant P5abc in the absence of divalent ions are shown in Figure

4-8. The DSC scans reveal two unfolding transitions which are similar to that observed in the optical experiment and are consistent with secondary structure unfolding. The thermodynamic values for the two unfolding transitions for wild type P5abc are T_m = 57.0 ^oC (ΔH_{cal} = 68.1 kcal mol^{-1}) and T_m = 67.5 ^oC (ΔH_{cal} = 45.3 kcal mol^{-1}). The two transitions for the A186U mutant have T_m = 55.1 ^oC (ΔH_{cal} = 68.0 kcal mol^{-1}) and T_m = 65.1 ^oC (ΔH_{cal} = 46.6 kcal mol^{-1}). The ΔH_{cal} values of 113.4 kcal/mol (P5abc) and 114.7 kcal/mol (A186U) obtained from the DSC experiment are slightly larger than the total ΔH_{VH} of 90.8 kcal/mol (P5abc) and 90.0 kcal/mol (A186U) values obtained from the optical experiment (Table 4-2). The ΔG_{total} values of 8.3 kcal/mol (P5abc) and 7.8 kcal/mol (A186U) obtained from the DSC experiment are also slightly larger than the ΔG_{VH} of 7.1 kcal/mol (P5abc) and 6.5 kcal/mol (A186U) obtained from the optical experiment (Table 4-2). In the presence of 2mM Mn^{2+} two transitions are observed by DSC in the unfolding of the wild type P5abc (Figure 4-9). The two transitions have T_m = 63.4 ^oC (ΔH_{cal} = 65.7 kcal mol^{-1}) and T_m = 72.9 ^oC (ΔH_{cal} = 95.7 kcal mol^{-1}). The ΔH_{cal} value of 161.4 kcal/mol obtained from the DSC experiment is consistent with the total ΔH_{VH} value of 148.1 kcal/mol obtained from the optical experiment (Table 4-2). The ΔG_{cal} value of 14.9 kcal/mol is also consistent with the ΔG_{VH} of 14.0 kcal/mol obtained from the optical experiment (Table 4-2).

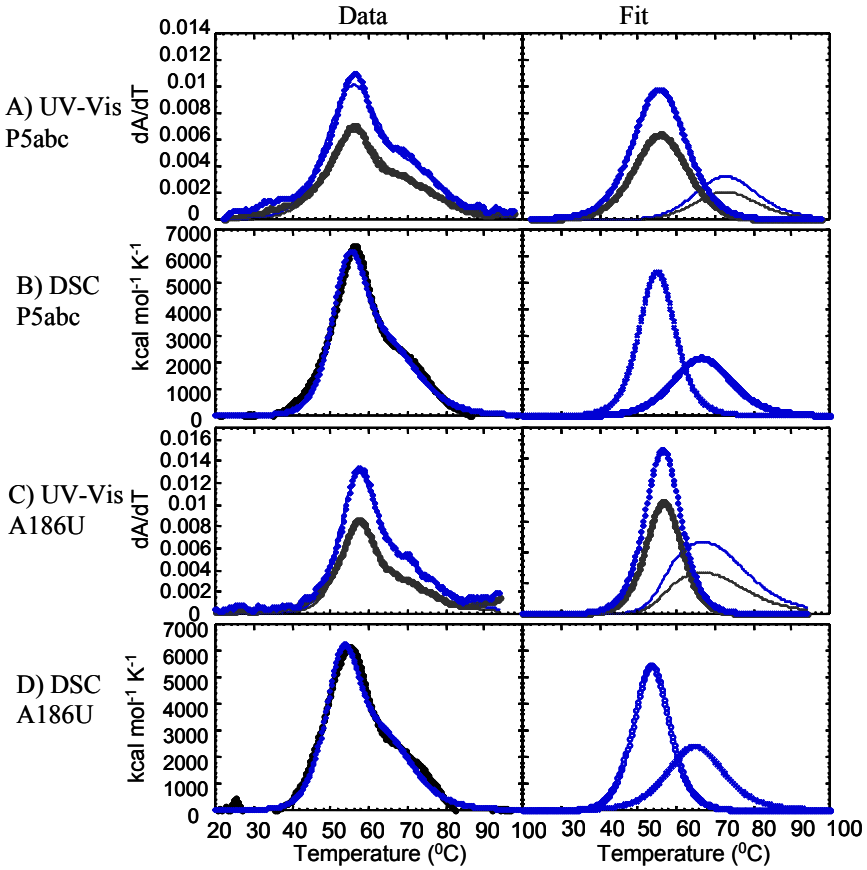

Figure 4-8. Comparison of UV-Vis and DSC thermal denaturation of P5abc and A186U in the absence of divalent ions. Comparison of A) and C)UV-Vis and B) and D) DSC thermal denaturation of P5abc and A186U. For both UV-Vis and DSC experiments, P5abc and the A186U mutant have similar unfolding transitions in the absence of divalent ions. All samples contained either 2 μM RNA (UV-Vis) or 30 μM RNA (DSC) in 5mM TEA, 100 mM NaCl, pH 7.8 buffer.

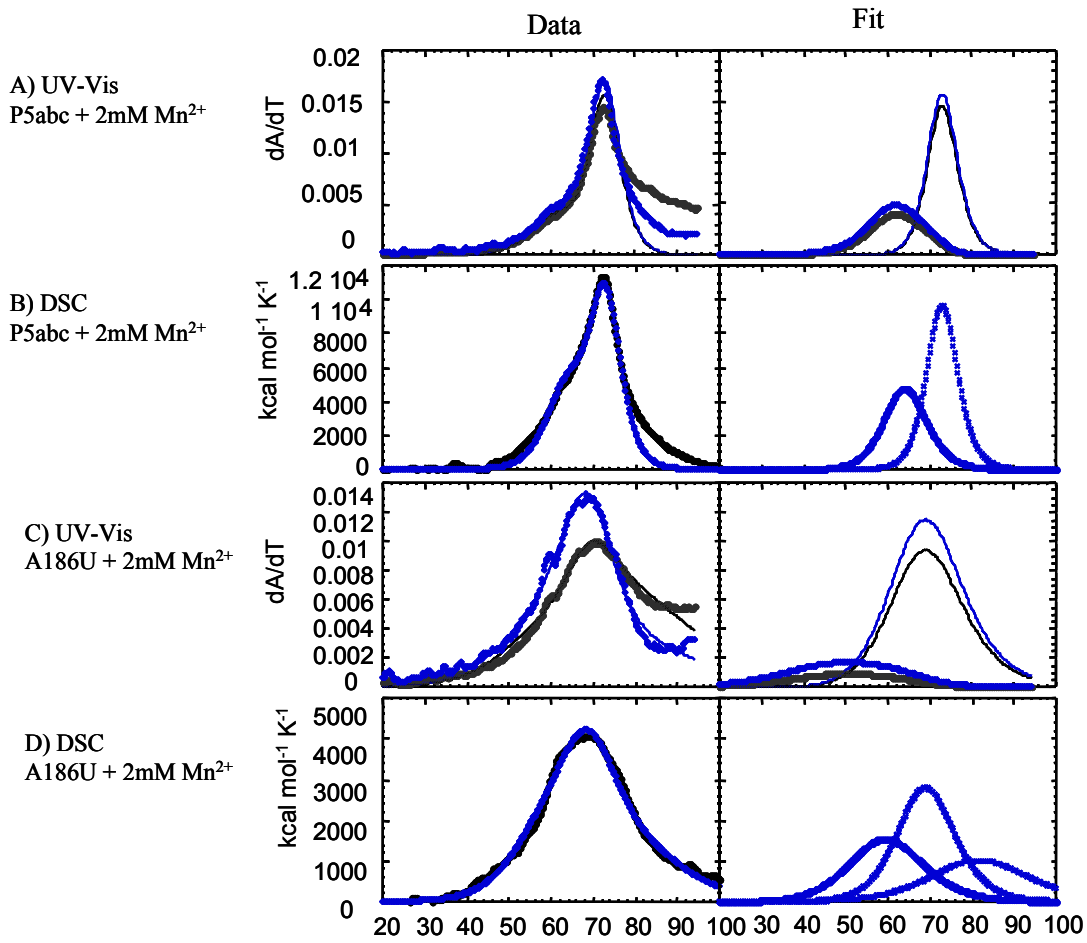

Figure 4-9. Comparison of UV-Vis and DSC thermal denaturation of P5abc and A186U in the presence of 2mM Mn^{2+}. All samples contained either 2 μM RNA (UV-Vis) or 30 μM RNA (DSC) in 5mM TEA, 100 mM NaCl, pH 7.8 buffer.

For the A186U mutant in the presence of 2 mM Mn^{2+}, the DSC data are best fit using three broad unfolding transitions (Figure 4-9D,Table 4-2). The data from the optical experiment were adequately fit using two transitions. In theory the data should fit the same, however in practice this is not what was found. The ΔH_{cal} and ΔG_{cal} values obtained from the DSC experiment are 32 kcal/mol and 4 kcal/mol respectively larger than the total ΔH_{VH} and ΔG_{VH} values obtained

from the optical experiment. This difference in total enthalpy for A186U in the presence of 2 mM Mn^{2+} between the optical and DSC experiment is due to not obtaining a fit for the third transition in the optical experiment.

The DSC experiments provide a direct determination of total enthalpy for the unfolding of P5abc and the A186U mutant in the absence and presence of divalent ions. The thermodynamic consequence of the ion core formation can be calculated in two different ways. The difference in ΔH_{tot} for P5abc in the absence and presence of divalent ions is $\Delta\Delta H$ = 47.6 kcal mol^{-1}. The difference in ΔH_{tot} for wild type P5abc and the nonfolding A186U mutant in the presence of 2 mM Mn^{2+} is $\Delta\Delta H$ = 41.7 kcal mol^{-1}. These numbers are quite similar. Therefore the average $\Delta\Delta H$ value of 44.7 kcal mol^{-1} is attributed to metal ion core formation in the P5abc subdomain. The difference in ΔG_{cal} for wild type P5abc and the nonfolding A186U mutant in the presence of 2 mM Mn^{2+} is $\Delta\Delta G$ = 3.5 kcal mol^{-1}. Therefore the $\Delta\Delta G$ value of 3.5 kcal/mol is attributed to metal ion core formation in the P5abc subdomain.

Thermal Denaturation of P5abc Fragments

The thermal denaturation properties of three fragments of P5abc, P5a, P5b and P5c (Figure 4-10) were determined in an attempt to identify the transitions in the unfolding pathway of the P5abc subdomain. A UUCG tetraloop was added after the C138-G180 base pair of the P5a fragment for stability. Previous NMR experiments confirmed that the three fragments, P5a, P5b and

P5c, have the same individual secondary structures as when they are present in the P5abc subdomain (Wu and Tinoco 1998).

The unfolding of P5a, P5b and P5c in the absence and presence of divalent ions is shown in Figures 4-11 and 4-12. Comparison of the individual unfolding profiles of the fragments with the unfolding transitions of the P5abc subdomain reveal that the fragments are more stable individually then when they are apart of the whole subdomain (Figure 4-11, Table 4-4). Also since a UUCG tetraloop was added to the P5a fragment it was expected to be more stable (Groebe and Uhlenbeck 1988; Antao et al. 1991). It is reasonable to assume that three-helix junction may destabilize helices P5a, P5b and P5c when they are a part of the whole P5abc subdomain (Draper and Gluick 1995). As predicted from Turner's rules in 1 M Na^+, the P5a fragment with the UUCG tetraloop should unfold with a T_m of 79^{o}C and a ΔH of 88.7 kcal/mol. It is important to note that the A-rich bulge is destabilizing to the P5a fragment structure however a thermodynamic value for this bulge can only be estimated based on limited thermodynamic information (Serra and Turner 1995). A T_m of 91.4 ^{o}C and a ΔH of 91.1 kcal/mol are predicted for the P5b fragment and a T_m of 84.2 ^{o}C and a ΔH of 76.0 kcal/mol are predicted for the P5c fragment. The predicted T_m values are higher for the individual fragments since the values are calculated in 1 M Na^+ conditions, however, the thermal denaturation data of the fragments (Figure 4-11) unfold in a similar trend to the predicted values with P5a and P5c unfolding first and P5b unfolding last. The predicted enthalpies for each

fragment are very similar to the enthalpies obtained from the fit for the thermal denaturation data. Therefore although the individual fragments are more stable than the whole P5abc subdomain, the profile in the absence of divalent ions for the addition of the three fragments unfolding may provide insight into how these helices unfold when they are a part of the whole subdomain (Figure 4-13). The P5a and P5c fragments are unfolding with similar T_m's. However, the P5a fragment with the UUCG tetraloop added is more stable than the native P5a helix in the P5abc subdomain. Therefore P5a and P5c may be contributing to the first unfolding transition for P5abc followed by P5b unfolding in the second transition.

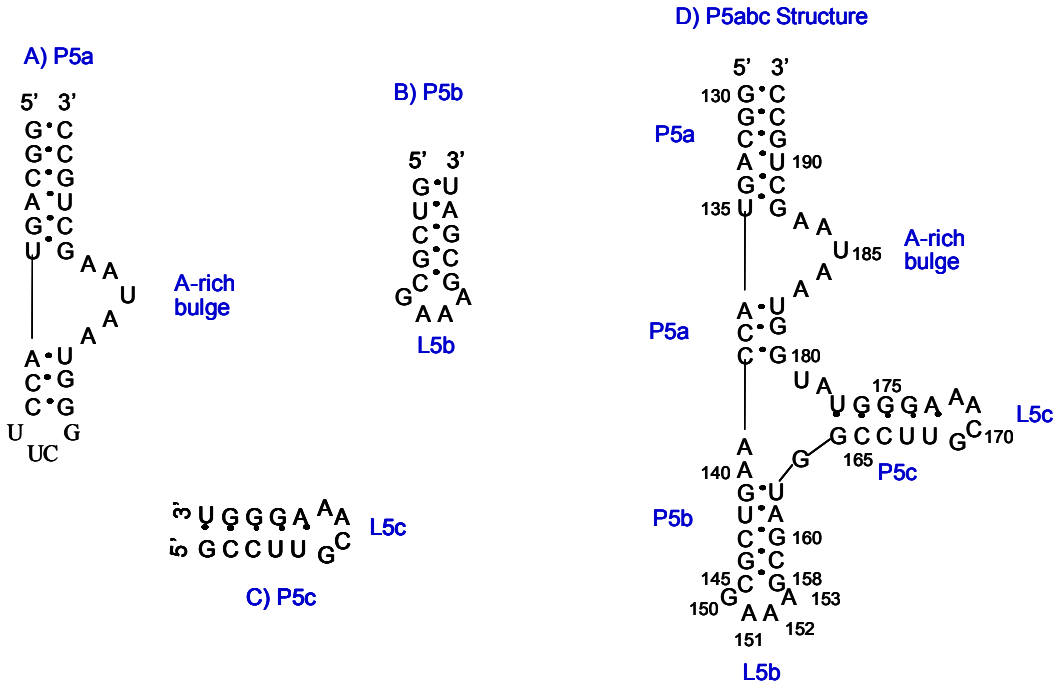

Figure 4-10. Secondary structures of the P5abc fragments vs. the P5abc subdomain. A) P5a, B) P5b, C) P5c and D) P5abc subdomain.

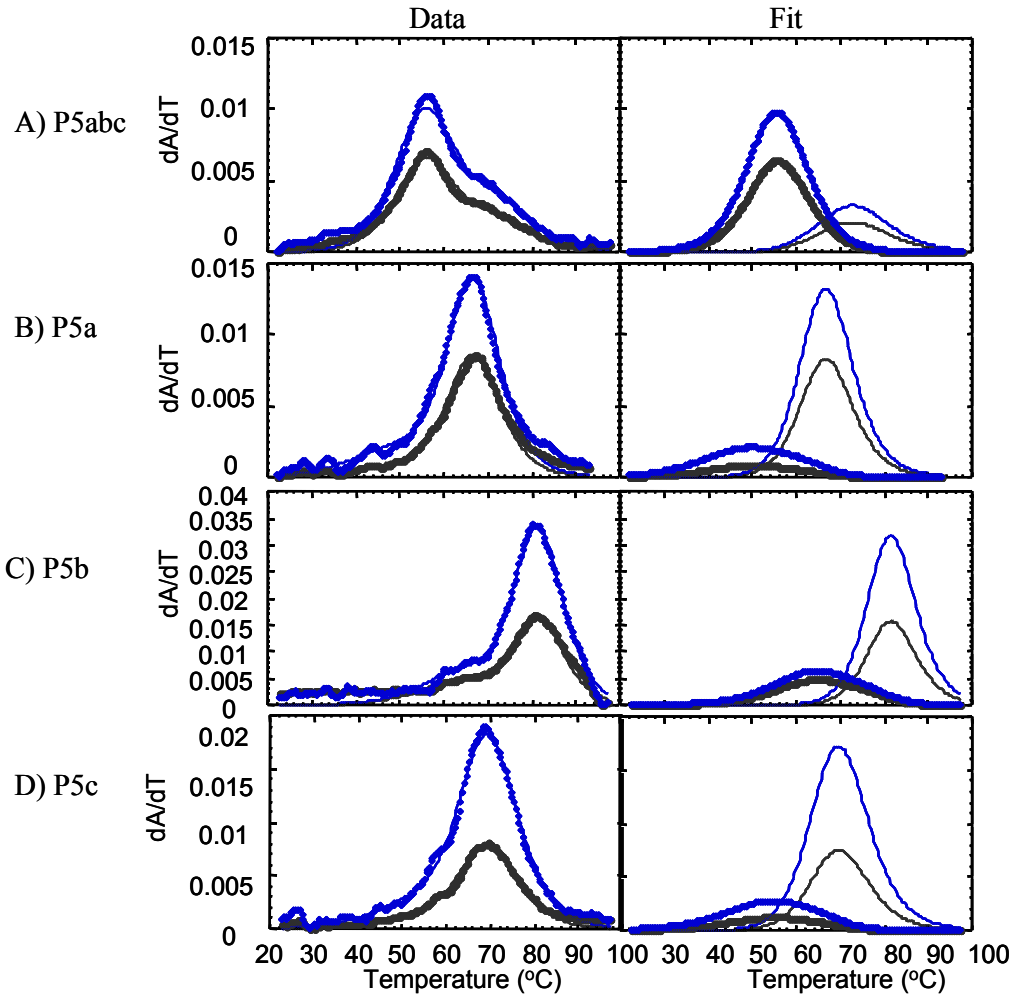

Figure 4-11. Optical melts of P5abc fragments in the absence of divalent ions. Comparison of A) P5abc unfolding with the B) P5a, C) P5b and D) P5c fragments. All samples contained 2 μM RNA in 5mM TEA, 100 mM NaCl, pH 7.8 buffer.

Table 4-4. Thermodynamic values obtained for the unfolding of the P5abc fragment and mutations.

RNA	$[Mn^{2+}]$	Transition	T_m (°C)	ΔH_{VH} (kcal mol^{-1})	ΔH_{total} (kcal mol^{-1})
P5a	0	1	50.1	29.1	79.1
	1mM	2	66.7	50.0	82.0
		1	55.0	22.0	
		2	70.3	60.0	
P5b	0	1	65.0	35.0	100.3
	1mM	2	80.7	65.3	101.6
		1	66.4	30.0	
		2	82.4	71.6	
P5c	0	1	50.0	35.0	82.2
	1mM	2	68.1	47.2	83.2
		1	54.6	33.0	
		2	69.6	50.2	
P5abc P5a mutant	0	1	51.1	47.4	104.4
	1mM	2	72.6	57.0	54.5
		1	68.4	54.5	
P5abc P5b mutant	0	1	55.5	68.5	68.5
	1mM	1	69.9	51.3	86.3
		2	88.1	35.0	
P5abc P5c mutant	0	1	38.6	43.3	77.4
	1mM	2	62.4	34.1	77.9
		1	63.3	47.6	
		2	87.0	30.3	

Samples contained 2 μM RNA, 5 mM TEA, 100 mM NaCl, pH 7.8.

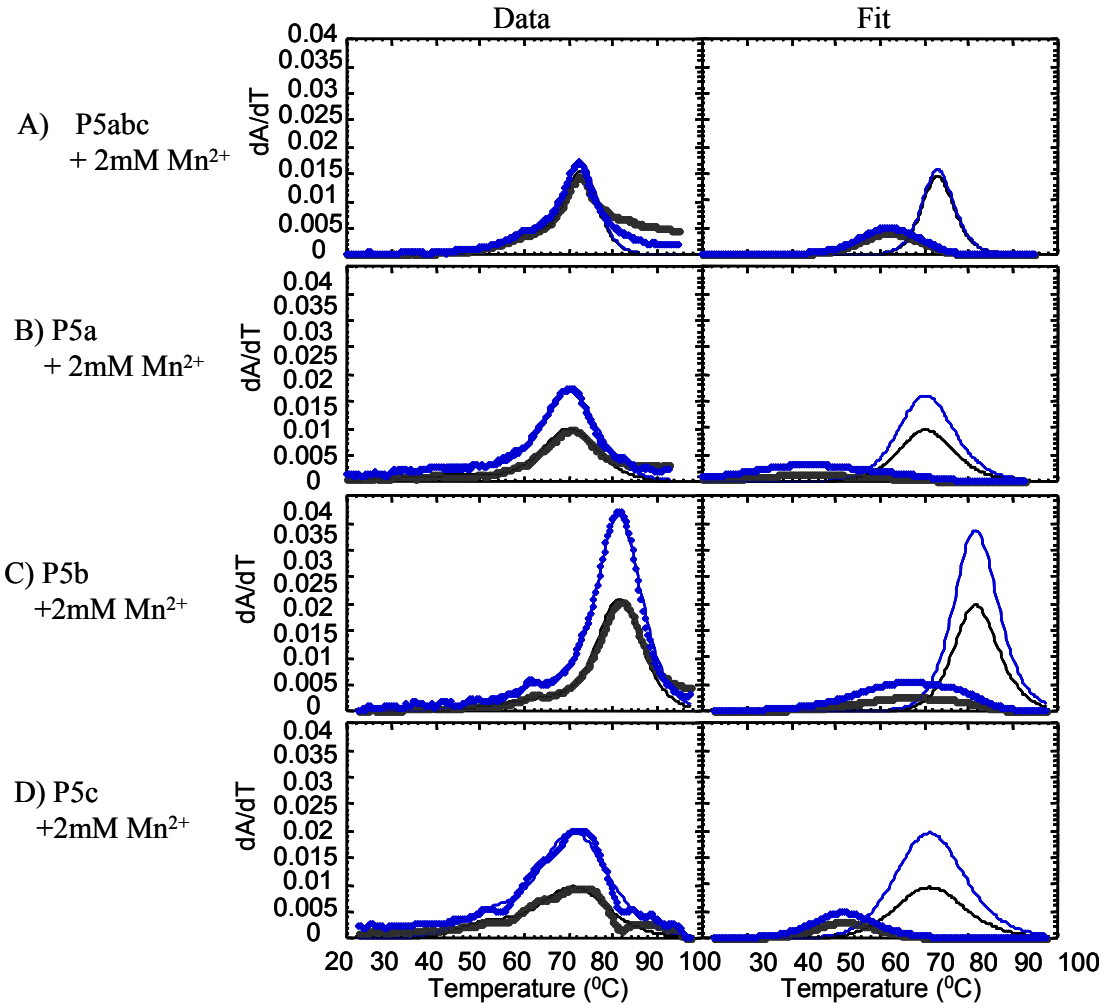

Figure 4-12. Optical melts of P5abc fragments in the presence of 2mM Mn^{2+}. Comparison of A) P5abc unfolding with the B) P5a, C) P5b and D) P5c fragments. All samples contained 2 μM RNA in 5mM TEA, 100 mM NaCl, pH 7.8 buffer.

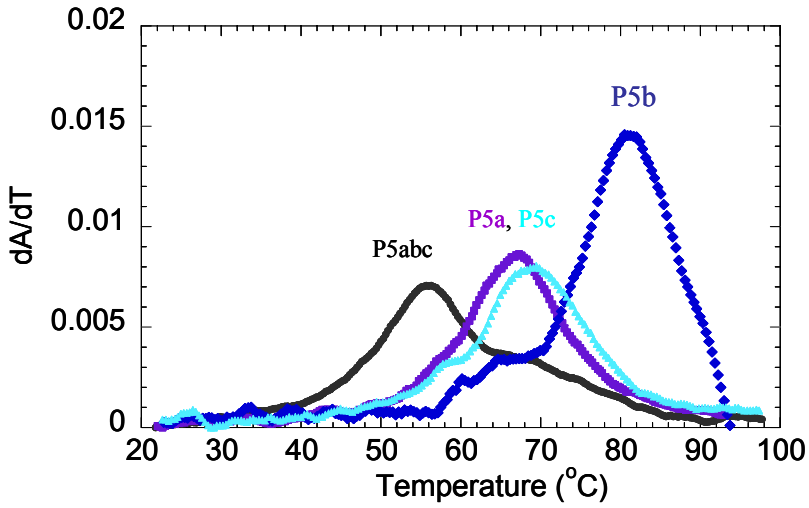

Figure 4-13. Overlap of P5abc with P5abc Fragments in the absence of divalent ions. P5abc (black line), P5a (purple line), P5b (blue line) and P5c (light blue line).

Upon the addition of divalent ions the three fragments again are more stable with higher T_m and ΔH values then when a part of the P5abc subdomain (Table 4-4). In the presence of 2 mM Mn^{2+}, P5b is the most stable and again P5a and P5c are less stable and have similar T_m's. The total increase in enthalpy of transition 2 for the three fragments in the presence of 2 mM Mn^{2+} added together is 20 kcal/mol. In the whole P5abc subdomain the total increase in enthalpy is 28 to 38 kcal/mol more than in the fragments. This data is consistent with thermal denaturation studies of a three helix junction in a 58-nucleotide ribosomal RNA from *E. coli* in which a total enthalpy of 25 kcal/mol was attributed to tertiary structure formation in the presence of 5 mM Mg^{2+} (Laing and Draper 1994). Only a 10 kcal/mol increase in enthalpy was observed for the addition of 5 mM Mg^{2+} to three individual helices (Laing and Draper 1994).

An addition of the enthalpies observed for the three fragments of P5abc in the absence (ΔH_{total} = 261 kcal/mol) and presence of divalent ions (ΔH_{total} = 267 kcal/mol) are twice the total enthalpies observed for the P5abc subdomain in the absence (ΔH_{total} = 113 kcal/mol) and presence (ΔH_{total} = 261 kcal/mol) of divalent ions. This data is consistent with enthalpies determined by isothermal titration calorimetry for the two individual stems in the hammerhead ribozyme compared to the hammerhead ribozyme which is a three-way RNA helical junction (Mikulecky et al. 2004). Folding of two of the three helices, stems 1 and 3, were studied individually and compared to the folding of the hammerhead ribozyme. Although only two of the three helices were studied individually, the total enthalpy for the addition of the stems 1 and 3 is approximately a third more than the total enthalpy for the hammerhead ribozyme (Mikulecky et al. 2004).

To further investigate the unfolding pathway of the whole P5abc subdomain, single base pair mutations were introduced individually into the P5a, P5b and P5c helices. The prediction is that the mutation would destabilize the transition due to the corresponding helix. The mutations are shown in Figure 4-14. For the P5a mutation the base pair G131-C192 was altered to an A-U base pair. For the P5b mutation the base pair G144-C159 was changed to an A-U base pair, and lastly for the P5c mutation the base pair G174-C166 was modified to an A-U base pair. The thermal melting profiles for the P5abc mutations in the absence and presence of divalent ions are compared to wild type P5abc in Figures 4-15 and 4-16. In the absence of divalent ions the P5abc

subdomain with the P5a mutation and the P5c mutation unfold in two transitions. However, the P5b mutation unfolds in one transition similar to transition one of wild type P5abc. Transition 1 for the P5a mutation is destabilized by 7 ^{o}C and transition 2 exhibits a 4 ^{o}C increase in stability in comparison with wild type P5abc. This destabilization in transition 1 for the P5a mutations is consistent with the prediction from the P5a fragment studies that the P5a helix unfolds in transition 1 of wild type P5abc. The P5c mutation unfolds in three transitions in which the P5c transition unfolds first followed by the P5a transition and then the P5b transition. This destabilization is also consistent with the prediction from the P5c fragment studies that the P5c helix unfolds with the P5a helix in transition 1 of wild type P5abc. For the P5b mutation only one unfolding transition is present at 58 ^{o}C. The prediction from the P5b fragment studies was that P5b unfolds last corresponding to transition 2 in wild type P5abc. Since transition two is not present in the unfolding of the P5b mutant, the A-U mutation in P5b may have destabilized this transition and now it is unfolding with the P5a and P5c helices. This is also consistent with the increase in ΔH value for transition 1 in the P5b mutant (ΔH = 68.5 kcal/mol) compared to the ΔH values for transition 1 in the P5a mutant (ΔH = 47.4 kcal/mol) and the P5c mutant (ΔH = 43.4 kcal/mol). All together the P5abc fragments and mutation studies predict that in the absence of divalent ions P5a and P5c helices unfold first followed by the P5b helix.

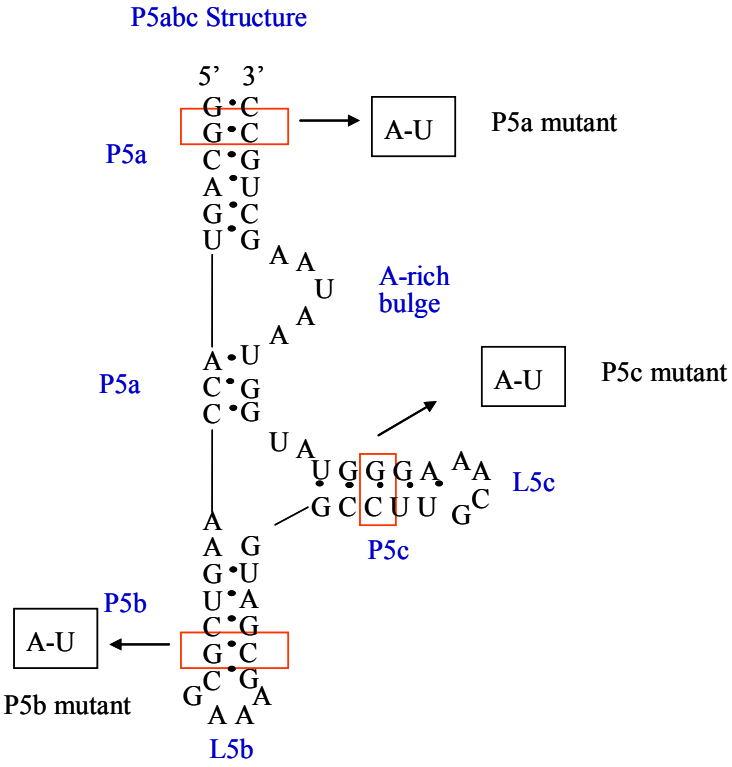

Figure 4-14. Secondary structure of P5abc subdomain with P5a, P5b and P5c mutants indicated in red boxes. All G-C base pairs were mutated to an A-U base pair.

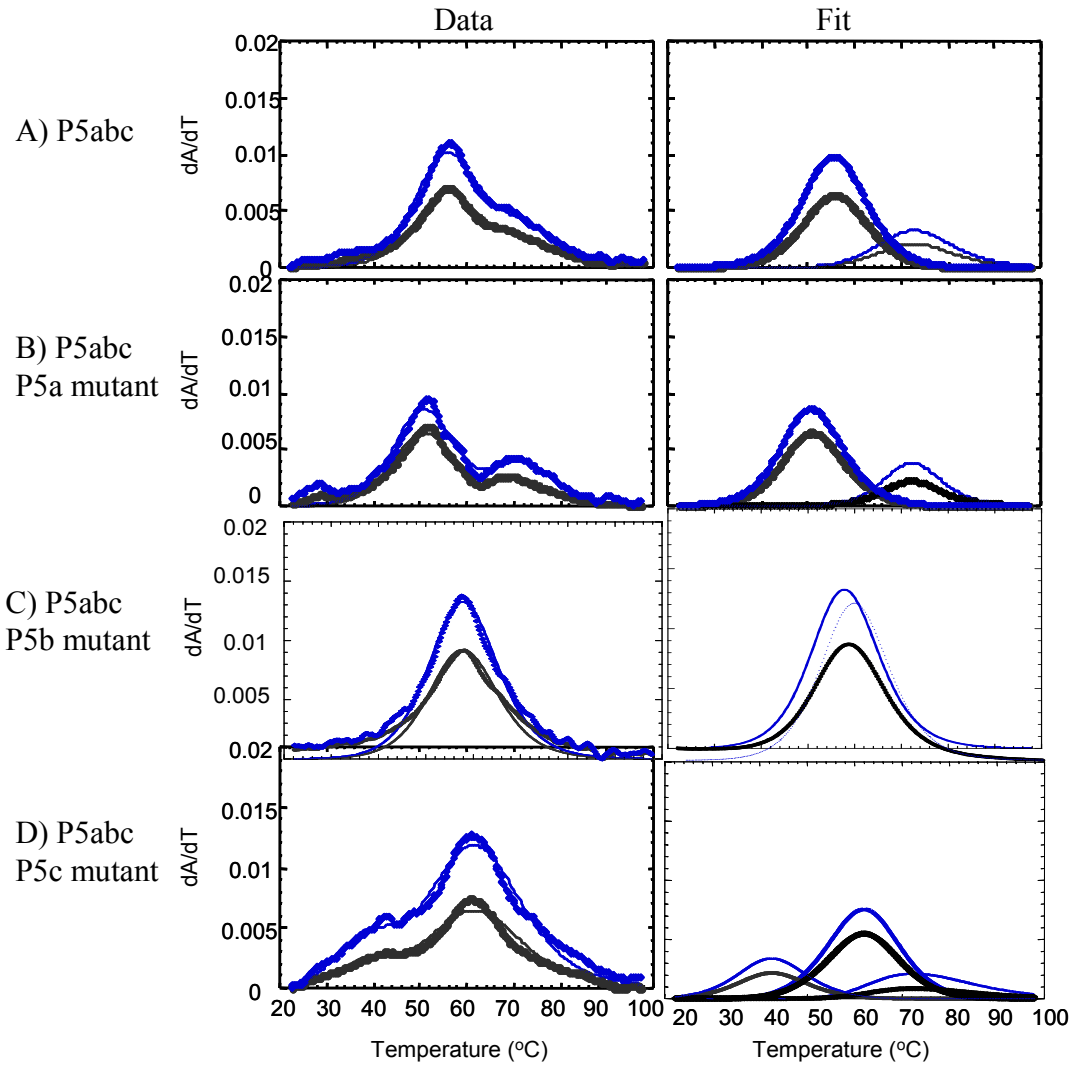

Figure 4-15. Optical melts of P5abc mutants in the absence of divalent ions. Comparison of A) P5abc unfolding with the B) P5a, C) P5b and D) P5c mutants

In the presence of 2 mM Mn^{2+} the P5a mutant unfolds in one transition while P5b and P5c mutants unfold in two transitions (Figure 4-16). The T_m's for all transitions increase upon the addition of Mn^{2+} indicating an increase in stability for the mutants (Table 4-4). The unfolding of transition 1 for all three P5abc mutants in the presence of 2 mM Mn^{2+} resemble unfolding transition 2 for

wild type P5abc in the presence of 2 mM Mn^{2+}. Again in agreement with the P5abc fragment studies all 3 helices may be unfolding in transition 2 of wild type P5abc. Although predictions cannot be made about the unfolding pathway of wild type P5abc in the presence of Mn^{2+} from this data, the mutations do indicate disruption of tertiary structure formation (metal ion core formation).

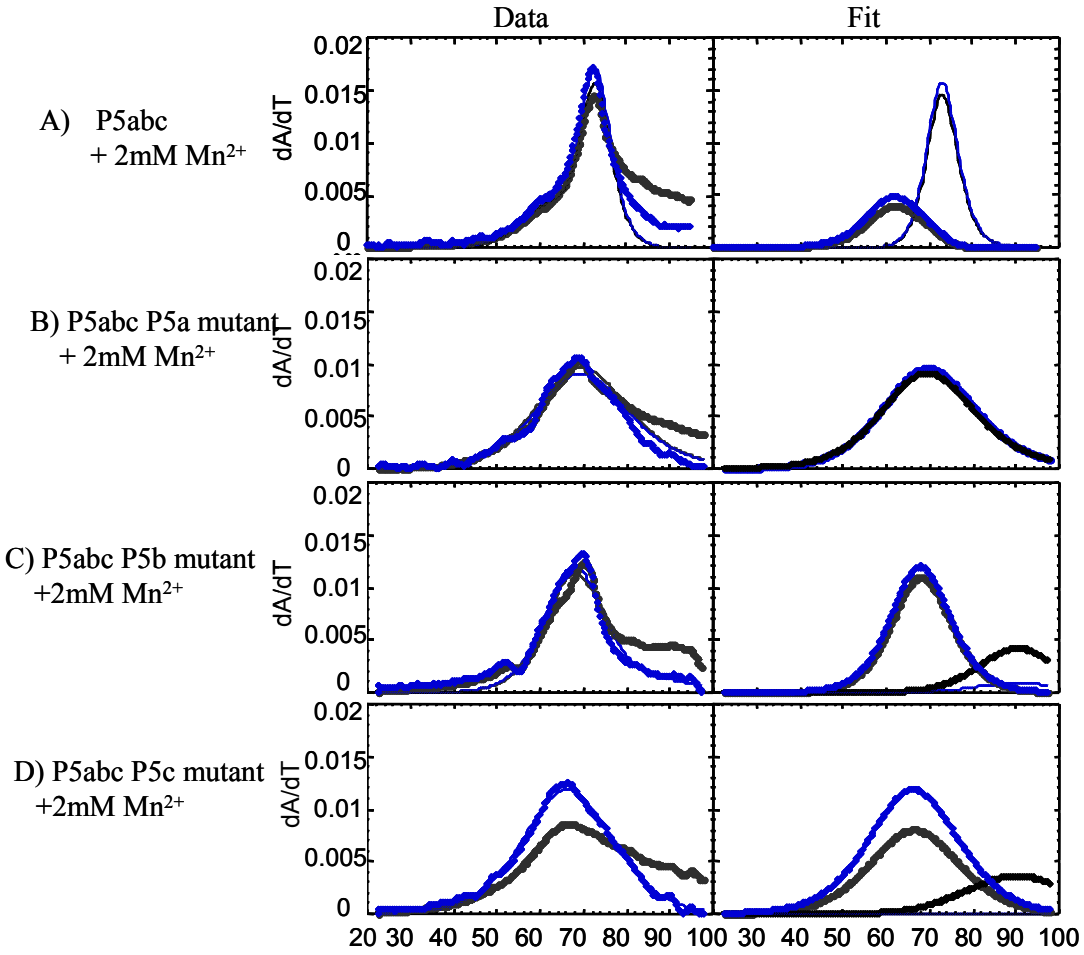

Figure 4-16: Optical melts of P5abc mutants in the presence of 2mM Mn^{2+}. Comparison of A) P5abc unfolding with the B) P5a, C) P5b and D) P5c mutants.

Discussion

Tertiary Structure Formation in the P5abc Subdomain

Results from hydroxyl radical footprinting studies of the truncated 56 nucleotide P5abc subdomain are consistent with previous hydroxyl radical footprinting studies of the native 72-nucleotide P5abc subdomain (Deras et al. 2000). The footprinting results indicate the truncated P5abc forms tertiary structure in the presence of divalent ions and the A186U mutant does not form tertiary structure. These results are also consistent with solution NMR and native gel electrophoresis studies of the truncated P5abc subdomain and the A186U mutant that indicate that P5abc folds into a tertiary structure in the presence of Mg^{2+} and the A186U mutant does not (Wu and Tinoco 1998).

Thermodynamic Analysis of P5abc Metal Ion Core Formation

The melting profiles reflecting secondary structure and tertiary structure formation in the P5abc subdomain were determined by both optical spectroscopy and differential scanning calorimetry. In 100 mM NaCl, the P5abc subdomain unfolds in two transitions. Since P5abc does not undergo tertiary structure formation in the absence of divalent ions these transitions have been assigned to secondary structure formation. Consistent with this, the A186U mutant also unfolds in two transitions similar to wild type P5abc in 100 mM NaCl. These results were expected since it has been shown that the A186U mutant forms the same secondary structure as does wild type P5abc (Wu and Tinoco 1998). Upon the addition of Mn^{2+} the apparent affinities of Mn^{2+} for both

unfolding transitions of wild type P5abc are 0.23 $\pm$ 0.03 mM for transition 1 and 0.08 $\pm$ 0.01 mM for transition 2. Since Mn^{2+} binds tighter to transition 2 and there is a 60.0 kcal/mol increase in enthalpy upon the addition of 2 mM Mn^{2+} to this transition, transition 2 may involve tertiary structure formation. The apparent affinities of Mn^{2+} for the A186U mutant are weaker for both transitions in comparison to wild type P5abc. There is no change in total enthalpy upon the addition of Mn^{2+} to the A186U mutant which suggests an absence of tertiary structure formation in this mutant. This data is consistent with the hydroxyl radical footprinting data that suggest the A186U mutant does not form the metal ion core.

Since the tertiary structure attributed to metal ion core formation has been assigned for P5abc, differential scanning calorimetry studies were utilized to directly determine the enthalpy of formation of this core. After comparing ΔH_{cal} for the P5abc subdomain in the absence and presence of 2 mM Mn^{2+} and comparing ΔH_{cal} for the A186U mutant and P5abc in the presence of 2 mM Mn^{2+}, it was determined that an average $\Delta\Delta H$ of 44.7 kcal mol^{-1} is the thermodynamic consequence for the formation of the metal ion core on the P5abc subdomain. The enthalpy for the formation of the metal ion core is consistent with previous RNA structure studies, including transfer RNA (Stein and Crothers 1976), a pseudoknotted α mRNA (Gluick and Draper 1994)and an *Escherichia coli* ribosomal RNA (Laing and Draper 1994), in which the unfolding enthalpies of 25-45 kcal mol^{-1} were assigned to tertiary structure. The free energy associated

with metal ion core formation was determined to have an average ΔG = 5.5 kcal/mol. The free energies associated with tertiary structure formation in transfer RNA (Stein and Crothers 1976), a pseudoknotted α mRNA (Gluick and Draper 1994)and an *Escherichia coli* ribosomal RNA (Laing and Draper 1994) range between 3.5 -11 kcal/mol. Therefore the ΔG = 5.5 kcal/mol associated with metal ion core formation is consistent with other known free energies for tertiary structure formation.

Investigation of P5abc Unfolding Pathway

The unfolding transitions of the fragments of the P5abc subdomain were utilized to investigate the unfolding pathway of P5abc. The results for these fragments in the absence and presence of divalent ions reveal the fragments are more stable alone then when they are combined as the whole subdomain. Based on the relative stabilities of the fragments, it is proposed that the P5a and P5c helices may be unfolding first and then P5b helix unfolding last. Results from the optical melting profiles for the P5abc mutations in each helix in the absence of divalent ions support this model. In the presence of Mn^{2+}, the unfolding of the three fragments are more stable then when they are apart of the P5abc subdomain. In the presence of 2 mM Mn^{2+}, there is a total increase in enthalpy of 20 kcal/mol for transition two in the three fragments added together. Upon the addition of 2 mM Mn^{2+}, there is an increase of 48 to 58 kcal/mol in transition two for the whole P5abc subdomain. This data suggests that the large increase in enthalpy in the presence of 2 mM Mn^{2+} for transition two in P5abc is

due to tertiary structure formation, while the small increase in enthalpy for the addition of the P5abc fragments in the presence of 2 mM Mn^{2+} is due to stabilization of the secondary structure. This data is consistent with thermal denaturation studies of a three helix junction in a 58-nucleotide ribosomal RNA from *E. coli* in which a total enthalpy of 25 kcal/mol was attributed to tertiary structure formation in the presence of 5 mM Mg^{2+} (Laing and Draper 1994). Only a 10 kcal/mol increase in enthalpy was observed for the addition of 5 mM Mg^{2+} to three individual helices (Laing and Draper 1994).

In the presence of Mn^{2+}, the P5abc mutants unfold in one main transition with similar T_m values. The T_m of this transition is similar to the large transition (transition 2) observed for wild type P5abc in the presence of Mn^{2+}. This data suggests that unfolding of helices P5a, P5b, and P5c may be contributing to transition 2 for the P5abc subdomain in the presence of Mn^{2+}. Results from this experiment are consistent with other RNA structure thermal denaturation studies. For example, thermal denaturation of $tRNA_f^{met}$ demonstrates that the individual transitions present in the absence of divalent ions, corresponding to both tertiary and secondary structure unfolding, collapse into a single transition in the presence of 3 mM Mg^{2+}.

CHAPTER V

SPECTROSCOPIC AND THERMODYNAMIC INVESTIGATION OF THE P4-P6 DOMAIN OF THE GROUP I INTRON

Introduction

The P4-P6 domain comprises half of the catalytic core of the Tetrahymena group I intron (Murphy and Cech 1993). A remarkable cluster of Mg^{2+} or Mn^{2+} ions has been shown to bind in the P5abc subdomain of the P4-P6 domain. Both the 2.3 Å and the 2.8 Å crystal structures of the P4-P6 domain reveal 12 Mg^{2+} or 12 Mn^{2+} ions bind to the domain, six of these ions are found in a cluster in the P5abc subdomain. (Cate et al. 1996; Juneau et al. 2001). Under solution conditions, the P4-P6 domain folds independently and formation of this domain investigated by time resolved hydroxyl footprinting studies establish it is the first step in the folding pathway of the ribozyme (Murphy and Cech 1993; Cate et al. 1996; Sclavi et al. 1998). Upon the addition of Mg^{2+}, the tertiary structure of the P4-P6 domain forms within 3 seconds (Sclavi et al. 1998). Hydroxyl radical footprinting studies also reveal that in the presence of Mg^{2+} the P4-P6 domain induces folding in the other catalytic domain of the group I intron, P3-P9 (Doherty and Doudna 1997). Therefore the P4-P6 domain organizes the formation of the catalytic core (Doherty and Doudna 1997). Since it has been shown under solution conditions that divalent ions are essential for folding of the P4-P6 domain, this research focuses on determining the number and affinity of

Mn^{2+} ions that bind to the domain and the thermodynamic properties of this domain in solution. An investigation for a spectroscopic signature of metal ion core formation in the whole P4-P6 domain was also conducted.

Results

Mn^{2+} Binding Affinities for the P4-P6 Domain

As previously determined for the P5abc subdomain, the relative affinities of Mn^{2+} for the P4-P6 domain were obtained under various NaCl concentrations from Mn^{2+} EPR titration experiments. The binding isotherm for P4-P6 in 10 mM, 50 mM and 100 mM NaCl is shown in Figure 5-1A. In 100 mM NaCl, 57.0 $\pm$ 4.9 Mn^{2+} ions bind to the P4-P6 domain with an average K_d of 198 $\pm$ 41.4 μM (Table 5-1). The number of Mn^{2+} ions that bind to the P4-P6 domain decreases with an increase in NaCl concentration and the relative affinities decrease (Figure 5-1A and Table 5-1). These data are consistent with the NaCl concentration dependence of Mn^{2+} binding to the P5abc subdomain (Chapter III). The decrease in Mn^{2+} binding with an increase in NaCl concentration suggests that diffuse metal binding can be satisfied with either monovalent or divalent cations.

Table 5-1. Relative affinities of Mn^{2+} for the P4P6 domain under various NaCl concentrations.

NaCl (mM)	*n*	K_d (μM)	n_H
10	74.1 $\pm$ 3.1	107 $\pm$ 12.9	1.3 $\pm$ 0.2
50	66.4 $\pm$ 3.4	154 $\pm$ 21.9	1.0 $\pm$ 0.1
100	57.0 $\pm$ 4.9	198 $\pm$ 41.4	0.98 $\pm$ 0.31

Samples contained 10 μM RNA in 5mM TEA, pH 7.8.

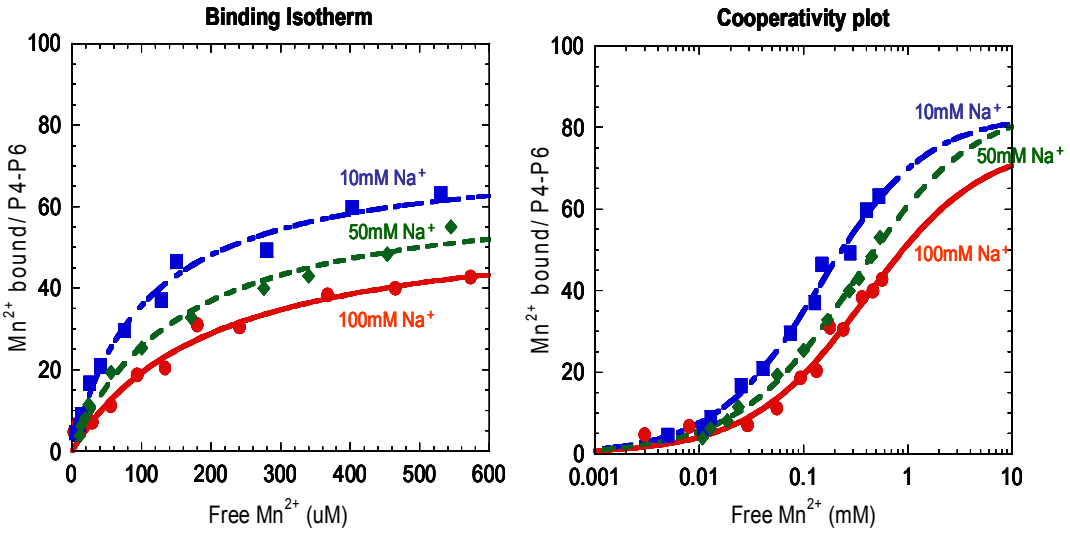

Figure 5-1. Na^+ dependence of P4 -P6 Mn^{2+} binding. A). Na^+ dependence of Mn^{2+} EPR binding isotherm. B). Cooperativity of Mn^{2+} binding to P4 -P6. (●) 100mM NaCl , (♦) 50mM NaCl and (■) 10mM NaCl. Each sample contained 10 μM RNA in 5mM TEA, pH 7.8. The binding isotherm data were fit to equation [2 -1] and the cooperativtiy data were fit to equation [2 -2].

The cooperativity of Mn^{2+} binding to P4-P6 was determined from the NaCl dependent Mn^{2+} EPR titration experiments (Figure 5-1B). The Hill coefficients determined for Mn^{2+} binding to P4-P6 under each NaCl concentration reveal an average n_H ~ 1.1 (Table 5-1). These data suggest that the binding of Mn^{2+} to P4-P6 is non-cooperative and the binding of one Mn^{2+} ion does not promote the binding of the next Mn^{2+} ion.

Spectroscopic Signature of Metal Ion Core Formation in the P4-P6 Domain

As previously discussed in Chapter III, the P5abc subdomain has been shown to fold around a metal ion core within the P4-P6 domain (Cate et al. 1996). Low temperature EPR microwave power saturation studies of the P5abc subdomain suggest that the metal ion core forms after 5 equivalents of Mn^{2+} are added to the subdomain. P5abc is a subdomain of the P4-P6 domain and P5abc folds first in the folding pathway of the P4-P6 domain (Murphy and Cech 1993). Therefore it is predicted that EPR microwave power saturation studies of the P4-P6 domain would result in similar $P_{1/2}$ values observed for the P5abc subdomain and a spectroscopic signature of the metal ion core would be obtained for the whole P4-P6 domain.

Microwave power saturation studies for 1 equivalent of Mn^{2+} to 1 P4-P6 through 10 equivalents of Mn^{2+} to 1 P4-P6 were obtained. An example of the microwave power saturation data for a 2mM Mn^{2+} standard vs. 2 equivalents of Mn^{2+} to 1 P4-P6 vs. 6 equivalents of Mn^{2+} to 1 P4-P6 is depicted in Figure 5-2. The $P_{1/2}$ values obtained for all equivalents of Mn^{2+} to P4-P6 are shown in Figure 5-3 and Table 5-2. From 1 through 4 equivalents of Mn^{2+} to 1 P4-P6 the $P_{1/2}$ value remains constant ($P_{1/2}$ ~ 5 mW). Upon the addition of the fifth equivalent of Mn^{2+}, the $P_{1/2}$ value increases to 9.2 $\pm$ 1.2 mW and continues to increase to 11.3 $\pm$ 0.9 mW with the sixth equivalent of Mn^{2+}. The $P_{1/2}$ value begins to level off after the sixth equivalent of Mn^{2+} is added to the P4-P6 domain. In comparison to the P4-P6 domain, microwave power saturation

studies of Mn^{2+} standards representing 2, 4, 6, 8 and 10 equivalents of Mn^{2+} results in similar $P_{1/2}$ values ($P_{1/2}$ ~ 4 mW) indicating that the increase in $P_{1/2}$ observed after 5 equivalents of Mn^{2+} are added to P4-P6 is due to the Mn^{2+} interacting with the RNA. Similar $P_{1/2}$ values are observed for the P5abc subdomain and the P4-P6 domain for all equivalents of Mn^{2+} (Figure 5-3, Table 3-4 and Table 5-2). Since the large increase in $P_{1/2}$ occurs after 5 equivalents of Mn^{2+} are added to the domain and this result is similar to that observed for the P5abc subdomain, this data suggests a spectroscopic signature of metal ion core formation in the P4-P6 domain.

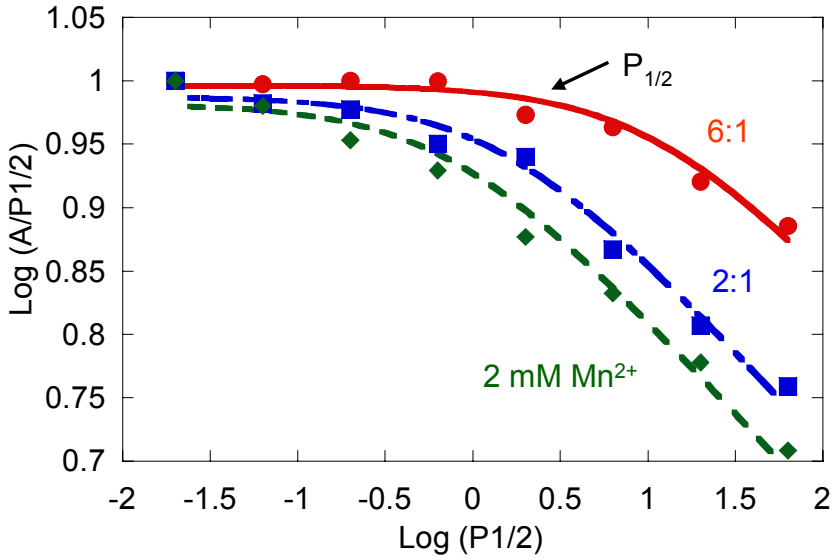

Figure 5-2. Example of EPR microwave power saturation behavior for Mn^{2+} bound to P4-P6. (●) $6Mn^{2+}$: 1P4-P6 , (■) $2Mn^{2+}$: 1P4-P6 and (♦) 2mM Mn^{2+} standard. The EPR microwave power saturation data were fit to [2-4]. Each sample contained 200 μM RNA in 5mM TEA, 100mM NaCl, pH 7.8 buffer. X-band EPR was run at 10K.

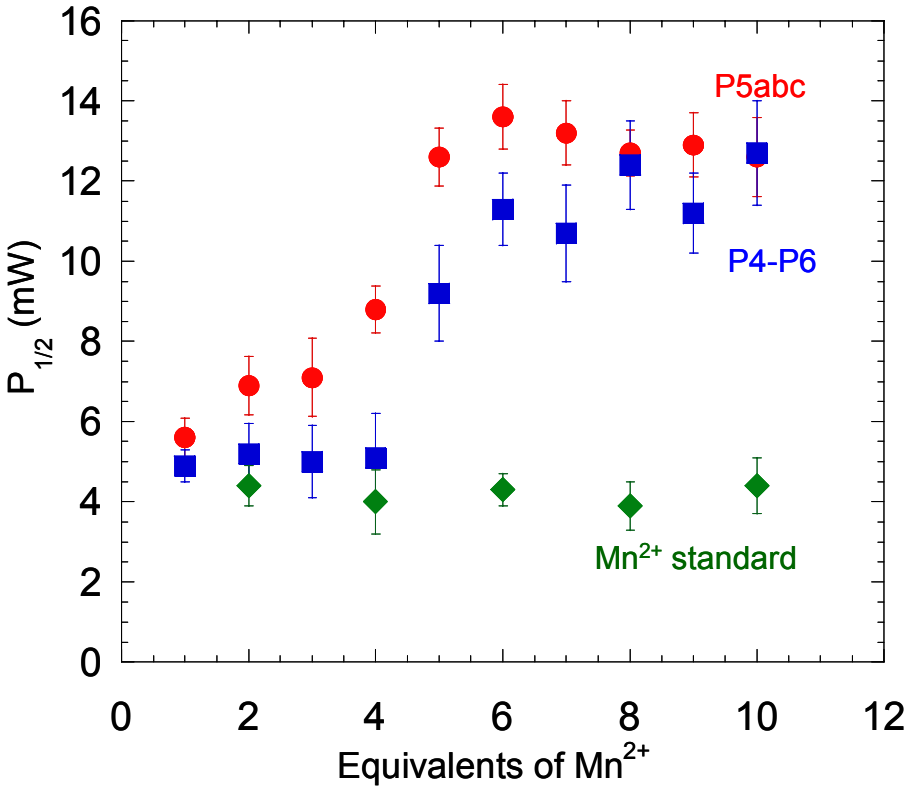

Figure 5-3. Microwave power saturation of P4-P6 domain. (●) WT P5abc, (■) P4-P6 domain and (♦) Mn^{2+} Standard.

Table 5-2. $P_{1/2}$ values obtained from microwave power saturation studies of the P4-P6 domain.

	$P_{1/2}$ (mW) values for different equivalents of Mn^{2+}									
RNA	1	2	3	4	5	6	7	8	9	10
P4-P6	4.9 ± 0.4	5.2± 0.8	5.0 ± 0.9	5.1 ± 1.1	9.2 ± 1.2	11.3 ± 0.9	10.7 ± 1.2	12.4 ± 1.1	11.2 ± 1.0	12.7 ± 1.3
Mn^{2+} Standards		4.4 ± 0.5		4.0 ± 0.8		4.3 ± 0.4		3.9 ± 0.6		4.4 ± 0.7

Samples contained 200 μM RNA, 5 mM TEA, 100 mM NaCl, pH=7.8, 20% ethylene glycol.

Thermal Denaturation of the P4-P6 Domain

Optically detected thermal denaturation experiments were used to analyze the thermodynamic properties of the P4-P6 domain and the influence of metal ions on these properties. Thermal denaturation profiles were acquired at 260 and 280 nm for the P4-P6 domain under 100 mM NaCl conditions in the absence and presence of Mn^{2+} (Figure 5-4). The data are shown as the derivative of absorbance with respect to temperature and are fit to an unfolding model consisting of sequential two-state unfolding transitions (Misra and Draper 1998; Nixon and Giedroc 1998). The experimental data are shown on the left-hand side and are superimposed with a smooth curve, which represents the optimized nonlinear least squared fit to the unfolding model. The individual transitions that make up the fit are shown on the right. Under 100 mM NaCl conditions, P4-P6 unfolds in two transitions with T_{m1} = 55.5 ^{o}C and T_{m2} = 61.5 ^{o}C and an overall ΔH_{total} = 256.4 kcal/mol (Table 5-3). With increasing concentrations of Mn^{2+} there is an increase in T_m for each transition indicating that the divalent ions are stabilizing the P4-P6 domain structure. An example of a thermal melting profile for the P4-P6 domain in the presence of Mn^{2+} is shown in Figure 5-4B. Upon the addition of 2 mM Mn^{2+} the P4-P6 domain unfolds in two transitions with T_{m1} = 60.0 ^{o}C and T_{m2} = 68.9 ^{o}C with an overall ΔH_{total} = 227.0 kcal/mol.

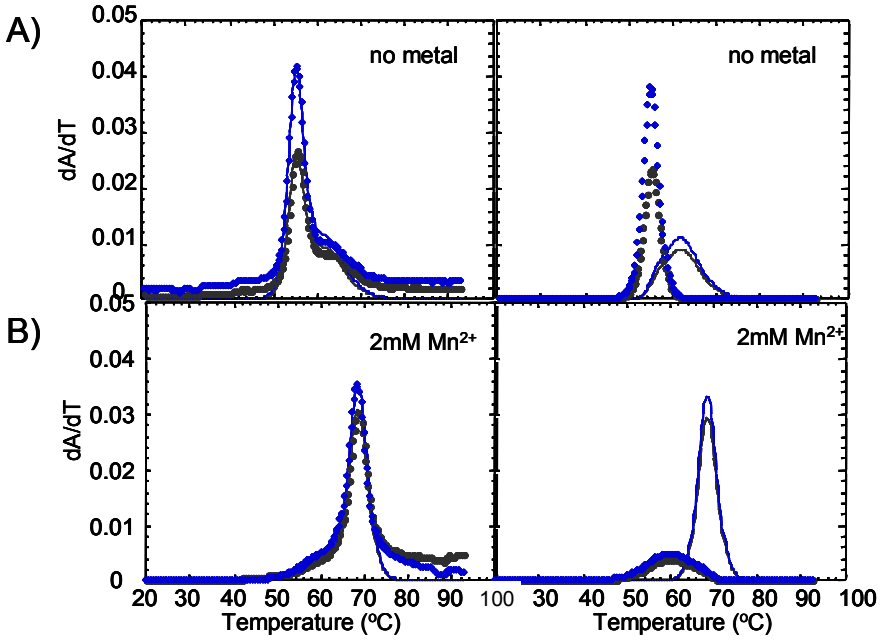

Figure 5-4. Comparison of melting profiles of the P4-P6 domain in the absence and presence of Mn^{2+}. A) P4-P6 B) P4-P6 + 2 mM Mn^{2+}. The data shown on the left were collected at two wavelengths, 260 nm (blue circles) and 280 nm (black circles). The calculated fits are shown as continuous lines through each data set. The data shown on the right represent individual transitions that make up the calculated fit to the data at each wavelength. All samples were obtained in 5mM TEA, 100 mM NaCl pH 7.8 buffer.

Table 5-3. Thermodynamic values obtained for the unfolding of the P4-P6 domain in 100 mM NaCl.

RNA	Conditions	Transition	T_m (ºC)	ΔH_{VH} (kcal mol^{-1})	ΔH_{total} (kcal mol^{-1})
P4P6		1 2	55.5 61.5	176.4 80.0	256.4
P4P6	2 mM Mn^{2+}	1 2	60.0 68.9	65.0 162.0	227.0

Samples contained 2μM RNA, 5mM TEA, 100mM NaCl, pH 7.8.

Turner's rules are a method for predicting thermodynamic properties of RNA. The method assumes that tertiary interactions between RNA motifs will be weaker than secondary structure interactions (Turner and Sugimoto 1988; Serra and Turner 1995). Therefore it is assumed that the sum of the ΔG, ΔH and ΔS

values of component secondary structures is a reasonable approximation of the total ΔG, ΔH and ΔS values (Turner and Sugimoto 1988; Serra and Turner 1995). Turner's rules predict an overall ΔH_{total} = 412 kcal/mol for the unfolding of the P4-P6 domain, and this is a 185 kcal/mol difference in ΔH_{total} observed from the optical experiments. This difference may be due to the fact that Turner's rules do not have values for all of the loops, bulges and junctions found in the P4-P6 secondary structure. Internal loops and bulges are known to be destabilizing to a structure while tetraloops, such as the GNRA tetraloop in the P5b helix, are known to be stabilizing (Turner and Sugimoto 1988). Therefore it is difficult to predict the thermodynamic values expected for the unfolding of the P4-P6 domain.

Mn^{2+} Dependence on the Unfolding of the P4-P6 Domain

Thermal denaturation profiles were obtained for the P4-P6 domain over a wide range of Mn^{2+} concentrations (10^{-5}-0.02 mM) in the presence of 100mM NaCl. The apparent affinity of Mn^{2+} for the folded form of the P4-P6 domain was determined by plotting $1/T_m$ vs. $[Mn^{2+}]$ and the data were fit to equation [2-10] (Figure 5-5). The apparent K_f, K_u and K_d values obtained for Mn^{2+} dependence of transition 1 are reported in Table 5-4. The apparent K_d value for Mn^{2+} for the unfolding of transition 1 is 0.414 $\pm$ 0.095 mM. As indicated previously the unfolding of the P4-P6 domain is too complex to assign each transition. However the apparent affinity of Mn^{2+} for the folded form of the P4-P6 domain (K_d = 0.414 $\pm$ 0.095 mM) is slightly weaker when compared to the apparent

affinity of Mn^{2+} for the folded form of the P5abc subdomain (K_d = 0.230 ±0.027 mM).

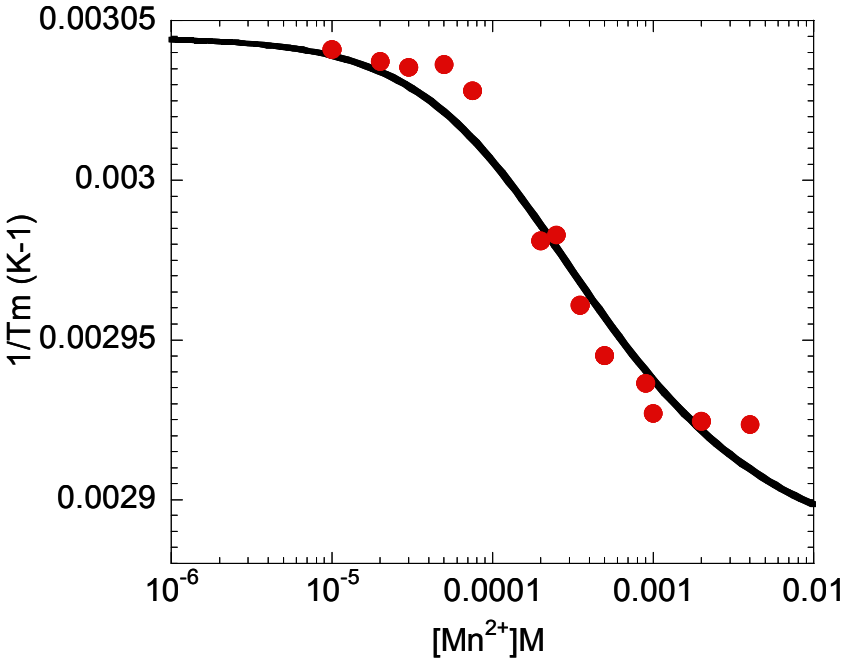

Figure 5-5. Mn^{2+} dependence on the UV-Vis thermal denaturation of P4-P6. Transition 1 Mn^{2+} dependence on folding of (•)P4-P6. The data were fit to equation [2-10].

Table 5-4. Mn^{2+} binding affinities for the P4P6 domain in 100 mM NaCl.

RNA	Transition	K_f (M^{-1})	K_u (M^{-1})	K_d (mM)
P4P6	1	2414	1248	0.414 ± 0.095

Samples contained 2 μM RNA, 5 mM TEA, 100 mM NaCl, pH 7.8.

Discussion

X-ray crystal structures of the P4-P6 domain reveal that 12 Mg^{2+} or Mn^{2+} ions bind to the domain and folding experiments under solution conditions reveal

these divalent ions are critical for folding of this domain. However the number and affinity of divalent ions bound to the P4-P6 domain under solution conditions has not been reported previously. Mn^{2+} EPR titration experiments reveal that under 100mM NaCl conditions, 57.0 ± 4.9 Mn^{2+} bind to the P4-P6 domain with an average K_d of 198 ± 41.4 μM and the binding of Mn^{2+} is non-cooperative. These cooperativity results contradict what has been seen in the literature for the dependence of folding of the P4-P6 domain on Mg^{2+} (Uchida et al. 2002). For 10 mM through 200 mM NaCl conditions it has been shown in footprinting experiments that the Hill coefficient for the folding of the P4-P6 domain with increasing concentrations of Mg^{2+} has on average a $n_H \sim 3.2$ (Uchida et al. 2002). However, the cooperativity of Mn^{2+} binding may not be linked to the cooperativity of folding of the P4-P6 domain in the presence of divalent ions.

Microwave power saturation studies of the P5abc subdomain reveal a clustering of Mn^{2+} ions after the addition of 5 equivalents of Mn^{2+} (Chapter III). Since the P5abc subdomain is the first to fold in the folding pathway of the P4-P6 domain (Doherty and Doudna 1997; Sclavi et al. 1998), Mn^{2+} microwave power saturation experiments were carried out on the P4-P6 domain to probe for metal ion core formation. With the addition of 5 equivalents of Mn^{2+} to the P4-P6 domain the $P_{1/2}$ value increases by ~ 4 mW. Upon addition of the sixth equivalent of Mn^{2+} the $P_{1/2}$ value continues to increase ~2 mW and with additional equivalents of Mn^{2+} the $P_{1/2}$ value remains constant. Similar results were observed for the P5abc subdomain, upon the fifth equivalent of Mn^{2+} to

P5abc the $P_{1/2}$ value increases by ~4 mW. Upon additional equivalents of Mn^{2+} to P5abc the $P_{1/2}$ value also remains constant. Since a total of 6 Mn^{2+} ions are proposed to bind in the core region of the P4-P6 domain (Juneau et al. 2001) and the P5abc subdomain is the first domain to fold, it is proposed that the increase in $P_{1/2}$ value observed for the microwave power saturation data for the P4-P6 domain is due to metal ion core formation. Furthermore since the $P_{1/2}$ values determined from the microwave power saturation experiment are an average of all Mn^{2+} dipole-dipole interactions within the system it is unlikely the large $P_{1/2}$ value obtained after the fifth equivalent of Mn^{2+} is only due to the two metals binding in the A-rich bulge.

Melting profiles were obtained for the unfolding of the P4-P6 domain in the absence and presence of Mn^{2+} by UV-Vis thermal denaturation. In the absence of divalent ions and in the presence of 100 mM NaCl the domain unfolds in two transitions. These transitions are likely due to the unfolding of the secondary structure of the P4-P6 domain since 100 mM NaCl is not sufficient to support tertiary structure formation (Takamoto et al. 2002; Uchida et al. 2002). However in the presence of greater than 200 μM Mn^{2+} the sharp main transition shifts to a maximum melting temperature of 69 ^{o}C and a new broad transition appears ~ 60 ^{o}C. The results for the thermal melting of the P4-P6 domain are similar to the results found for the P5abc subdomain. For the P5abc subdomain there is evidence to support the assignment of transition 1 and transition 2 individually to tertiary structure formation. The broad low temperature transition

observed in the presence of greater than 250 μM Mn^{2+} may be due to tertiary structure formation due to comparison of the unfolding transitions with a non-folding mutant of P5abc (Chapter IV). On the other hand, the large increase in enthalpy upon the addition of Mn^{2+} to P5abc and the tighter apparent affinity of Mn^{2+} for transition 2 may be evidence for tertiary structure in transition 2. The first transition observed ~ 60 ^{o}C for the P4-P6 domain in the presence of greater than 200 μM Mn^{2+} may be due to tertiary structure formation in the P4-P6 domain. However, further mutational studies will be required to definitively assign this transition. There was no increase in enthalpy observed for the P4-P6 domain in the presence of 2 mM Mn^{2+}.

The Mn^{2+} dependence of transition 1 was studied and the apparent K_d = 0.414 ± 0.095 mM. The apparent K_d for the association of Mn^{2+} ions for the folded form of the P4-P6 domain is weaker than that observed for the P5abc subdomain. Also the apparent K_d (0.414 ± 0.095 mM) obtained from the thermal denaturation experiments is weaker than the apparent K_d (0.198 $\pm$ 0.414 mM) determined from the Mn^{2+} EPR titration experiments. However, there are differences in the information obtained between these two experiments for the influence of divalent ions on the P4-P6 domain. The data obtained from the thermal denaturation studies of the P4-P6 domain in the absence and presence of divalent ions are only reporting on the influence of the divalent ions on stabilizing the structure. The thermal denaturation data does not provide information about the number of metals binding to the P4-P6 domain. The

Mn^{2+}EPR titration data do report on the number and affinity of Mn^{2+} binding to the subdomain.

CHAPTER VI

CONCLUSIONS

This dissertation focuses on the spectroscopic and thermodynamic characterization of an unusual metal-RNA cluster found in the P5abc subdomain of the *Tetrahymena* group I intron. An understanding of the role of these metal ions for facilitating the correct structure of the P5abc subdomain provides insight into the structure/function relationship of the P5abc subdomain and the P4-P6 domain in the *Tetrahymena* group I intron.

Monovalent and divalent cations are essential for RNA structure and function (V. J. DeRose 2003; Draper 2004). Divalent ions have been shown to be required for the folding of several ribozymes along with being essential for catalytic activity (Pyle 2002). These metal-dependent ribozymes include the group I and group II introns, RNase P ribozyme, hammerhead ribozyme, hairpin ribozyme, and hepatitis delta virus (HDV) ribozyme (Pyle 2002; Nakano et al. 2003).

Various EPR spectroscopy techniques were employed to investigate Mn^{2+} ions bound to the P5abc subdomain. Results from Mn^{2+} EPR titration experiments reveal that in the presence of 100 mM NaCl, 12 ± 1.1 Mn^{2+} bind to the subdomain non-cooperatively with an apparent affinity of 136 ± 18 μM. Under these same conditions the apparent affinity of Mn^{2+} for the P5abc subdomain is weaker in comparison to the apparent affinities determined for the Mn^{2+} sites in the hairpin ribozyme (K_d ~54.4 μM) and the first type of Mn^{2+} site

found in the hammerhead ribozyme (Type 1: K_d ~ 4 μM and Type 2: K_d ~ 460 μM) (Horton et al. 1998; Kirchner 2002). However, results from Na^+ competitions studies reveal that at high concentrations of NaCl, ~ 9 Mn^{2+} tight sites remain. These 9 sites may be consistent with the metal ion core occupied either with site bound Mg^{2+} or Mn^{2+} observed in both crystal structures (Cate et al. 1996; Juneau et al. 2001) .

A spectroscopic signature of metal ion core formation was assigned for the P5abc subdomain by EPR microwave power saturation studies. The Mn^{2+} EPR microwave power saturation studies of the P5abc subdomain and corresponding mutants reveal that the addition of 5 equivalents of Mn^{2+} are required for the wild type P5abc subdomain to form the metal ion core under solution conditions. Also, results from the microwave power saturation studies suggest this technique is useful for identifying a clustering of Mn^{2+} ions. A cluster of metal ion interactions in helices P1-P4 of the RNase P ribozyme, which is the catalytic core, has been proposed from thiophilic metal ion rescue experiments (Christian et al. 2002). Also a metal cluster has been proposed in the *Anabaena* group I intron from phosphorothioate interference experiments (Luptak and Doudna 2004). Microwave power saturation of both the RNase P and Anabaena group I intron ribozyme may provide additional support for metal cluster formation in these RNA structures.

The microwave power saturation results for wild type P5abc are consistent with the metal ion core determined from the X-ray crystal structures of

the P4-P6 domain (Cate et al. 1996; Juneau et al. 2001). Microwave power saturation studies of phosphorothioate substituted P5abc reveal formation of the metal ion core with an A171 PS can be rescued with Mn^{2+} while the A186 PS cannot. These results are consistent with previous Mn^{2+} rescue experiments (Basu and Strobel 1999). Although the exact Mn^{2+}-dependent folding pathway could not be determined from these studies, the data suggest that Mn^{2+} binding to A186 occurs in the last stages of metal ion core formation and this nucleotide is critical for tertiary structure formation.

Since the Mn^{2+} EPR investigation of the P5abc subdomain revealed evidence for metal ion core formation, the thermodynamic consequence of this metal ion core was probed by thermal denaturation techniques. Divalent ions are required for metal ion core formation in wild type P5abc while in the absence of divalent ions both wild type P5abc and the non-folding A186U mutant exhibit the same secondary structure (Wu and Tinoco 1998; Deras et al. 2000). Therefore the two unfolding transitions observed in the absence of divalent ions for the P5abc subdomain in the UV-Vis and DSC experiments have been assigned to secondary structure. Similarly, the two unfolding transitions observed for the A186U mutant in the absence of divalent ions are assigned to secondary structure. However, in the presence of Mn^{2+}, there are clear differences in the unfolding profiles of wild type P5abc and the A186U mutant. In the presence of greater than 0.250 mM Mn^{2+}, a low enthalpy transition present in the unfolding profile for wild type P5abc but absent in the unfolding

profile of the A186U mutant may be due to metal ion core formation. The large increase in enthalpy observed in transition 2 of P5abc in the presence of Mn^{2+} suggests evidence for tertiary structure in transition 2. However, that assignment of either unfolding transition in the P5abc subdomain in the presence of Mn^{2+} to tertiary structure formation cannot be elucidated from this data.

To directly determine the thermodynamic consequence of formation of the metal ion core in the P5abc subdomain, DSC experiments were utilized. After comparing ΔH_{cal} for the P5abc subdomain in the absence and presence of 2 mM Mn^{2+} and comparing ΔH_{cal} for the A186U mutant and P5abc in the presence of 2 mM Mn^{2+}, it was determined that an average $\Delta\Delta H$ of 44.7 kcal mol^{-1} is the thermodynamic contribution from the formation of the metal ion core in the P5abc subdomain. The enthalpy for the formation of the metal ion core is consistent with previous RNA structure studies, including transfer RNA (Stein and Crothers), a pseudoknotted α mRNA (Gluick and Draper) and an *E. coli* ribosomal RNA (Laing and Draper), in which the unfolding enthalpies of 25-45 kcal mol^{-1} were assigned to tertiary structure formation. Likewise, the average $\Delta\Delta G$ value of 5.3 kcal/mol is attributed to metal ion core formation in the P5abc subdomain. The free energy associated with tertiary structure P5abc is consistent with the free energy associated with tertiary structure formation in transfer RNA (Stein and Crothers), a pseudoknotted α mRNA (Gluick and

Draper) and an *E. coli* ribosomal RNA (Laing and Draper), which range between 3.5-11 kcal/mol.

The metal-dependent folding pathway of wild type P5abc was probed by thermal denaturation studies of P5abc fragments and mutations. Although the exact metal-dependent folding pathway could not be elucidated from these experiments, the results from the P5abc fragment and mutations studies ultimately suggest that the unfolding of P5abc is cooperative where unfolding of one helix promotes the unfolding of the next helix. Future mutation studies in the three helices may provide more insight into the P5abc unfolding pathway.

The P4-P6 domain of the *Tetrahymena* group I intron ribozyme contains the P5abc subdomain. The P4-P6 domain folds independent of the rest of the ribozyme, and in the presence of divalent ions, the P5abc subdomain containing the metal ion core folds first (Murphy and Cech 1993; Cate et al. 1996; Sclavi et al. 1998). To further explore the formation of the metal ion core in the P5abc subdomain, spectroscopic and thermodynamic experiments were performed on the P4-P6 domain. Mn^{2+} EPR titration experiments reveal that in the presence of 100 mM NaCl, 57.0 $\pm$ 4.9 Mn^{2+} bind to the P4-P6 domain with an average K_d of 198 $\pm$ 41.4 μM and the binding of Mn^{2+} is non-cooperative. It has been shown through Mg^{2+}-induced folding experiments on the P4-P6 domain that the folding of this domain is cooperative in the presence of increasing concentrations of Mg^{2+} (Sclavi et al. 1998; Deras et al. 2000; Uchida et al. 2002). However, the folding experiments are not reporting on the cooperativity of divalent ions binding

to the P4-P6 domain; they are only reporting on cooperativity of the folding event in the presence of divalent ions. Although it has been proposed that these two types of experiments may be reporting on the same events, it is clear from the results presented here that they are not. It is not known whether or not the chelated metal binding sites are preformed or the folding event induces them.

The search for a spectroscopic signature of metal ion core formation in the P4-P6 was investigated by Mn^{2+} EPR microwave power saturation techniques. Results from these experiments suggest that the increase in microwave power at half saturation ($P_{1/2}$) upon 5 equivalents of Mn^{2+} is due to metal ion core formation in the P5abc subdomain of the P4-P6 domain. These results are similar to that reported for the Mn^{2+} microwave power saturation studies of the P5abc subdomain alone. Results from both domain and subdomain microwave power saturation studies suggest this technique can be applied for detecting clustering of Mn^{2+} ions in other RNA structures.

Thermal denaturation experiments on the P4-P6 domain in the absence and presence of divalent ions provide insight into the unfolding pathway of this domain. In the presence of 100 mM NaCl, the two unfolding transitions observed for the P4-P6 domain have been assigned to secondary structure. This assignment is based on numerous folding experiments of the P4-P6 domain that suggest this domain does not form tertiary structure in the absence of divalent ions (Takamoto et al. 2002; Uchida et al. 2002; Westhof 2002; Woodson 2002). In the presence of Mn^{2+} the P4-P6 domain unfolds in two

different transitions in which the first transition could be due to tertiary structure formation based on results from the unfolding of the P5abc subdomain in the presence of divalent ions. However, there is no evidence that the first transition is due to tertiary structure. Non-folding mutants of this domain (ex. A186U) needs to be explored in these thermal denaturation studies to correctly assign these transitions. Lastly, a direct determination of the total enthalpy for the unfolding of the P4-P6 domain in the absence and presence of divalent ions by DSC is required to accurately compare the thermodynamic contributions of these unfolding events.

In summary, a spectroscopic signature of metal ion core formation has been assigned for the P5abc subdomain by Mn^{2+} EPR microwave power saturation studies. The thermodynamic consequence of this metal ion core was determined to be an average $\Delta\Delta H$ of 44.7 kcal/mol. The $\Delta\Delta H$ value obtained for tertiary structure formation in the P5abc subdomain is consistent with $\Delta\Delta H$ values obtained for other RNA tertiary structures. Thermal denaturation experiments on P5abc fragments and point mutations as well as Mn^{2+} EPR microwave power saturation studies on phosphorothioate substituted P5abc were utilized to explore the metal-dependent folding pathway of the P5abc subdomain. From these experiments, a metal-dependent folding pathway has been proposed (Figure 3-9). Results from Mn^{2+} EPR microwave power saturation studies of the P4-P6 domain reveal a spectroscopic signature of metal ion core formation similar to that observed for the P5abc subdomain alone.

Further thermal denaturation experiments are required to assign a $\Delta\Delta H$ value for tertiary structure formation in the P4-P6 domain.

Future Directions

Further Investigation of P5abc Metal-Dependent Folding Pathway

A proposed metal-dependent folding model of the P5abc subdomain has been constructed based on microwave power saturation studies of Mn^{2+} binding to wild type and mutant P5abc (Figure 3-9). To elucidate the metal-induced folding pathway of the P5abc subdomain, site-directed spin labeling in conjunction with EPR spectroscopy could be employed. In these experiments, dipolar line broadening of the EPR spectrum can be observed for RNAs with interspin distances between 10 – 25 Å using continuous wave EPR (Kim 2004) and longer distances ($\leq$ 80 Å) by PELDOR (Schiemann et al. 2003) . Previously, it has been demonstrated that EPR spectroscopy can be used to observe changes in the distance between two nitroxide spin-labels in HIV-1 TAR RNA, in the absence and presence of divalent ions, due to conformational changes of the RNA (Kim 2004). For the metal-dependent folding of the P5abc subdomain, spin-labels could be placed in two specific locations in the subdomain, and upon the addition of each equivalent of divalent ion, the distance between two spin-labels could be determined. Various spin-label positions could be investigated within the subdomain. For example, placing a spin-label in the A-rich bulge and the P5c helix and determining at which equivalent of Mn^{2+} the spin-labels come closest together would provide information on whether the large increase in $P_{1/2}$

observed, in the microwave power saturation studies, after 5 equivalents of Mn^{2+} are added to the subdomain is due to formation of the whole metal ion core or just the binding of the two closest ions in the A-rich bulge.

P4-P6 Mutations and Fragments

Studies of mutations in the P4-P6 domain, specifically the non-folding A186U mutant, would provide further information to the spectroscopic and thermodynamic investigation of the domain presented here. Similar to the P5abc subdomain, Mn^{2+} EPR microwave power saturation studies of the non-folding A186U mutant of the P4-P6 domain could be explored to confirm the spectroscopic signature of metal ion core formation observed for this domain. This mutation could also provide information on assignment of the unfolding transitions observed for the P4-P6 domain in the presence of Mn^{2+} in the UV-Vis thermal denaturation experiments. Also, the P4-P5-P6 helix fragment of the P4-P6 domain could be melted individually to help in assigning the unfolding transitions from the thermal denaturation experiments.

Differential Scanning Calorimetry of P4-P6 Domain

DSC studies of the P4-P6 domain would provide a direct measurement of the total enthalpy for the unfolding of this domain in the absence and presence of divalent ions. DSC experiments on the A186U mutant may also provide an enthalpic value for tertiary structure formation in the P4-P6 domain. As determined for the P5abc subdomain alone, a comparison of the $\Delta\Delta H$ value for the tertiary structure in the P4-P6 domain to other known $\Delta\Delta H$ values tertiary

RNA structures could be performed. This information would provide insight into the thermodynamic contributions of the divalent metal-dependent tertiary structure formations in the P4-P6 domain.

As suggested above for the P5abc subdomain, spin-labeling experiments in conjunction with EPR spectroscopy could be applied to probe the metal-dependent folding pathway of the P4-P6 domain. The metal-dependent folding pathway of both the P5abc subdomain and the P4-P6 domain would provide more information on how metal ions contribute to the compact folding of ribozymes.

REFERENCES

Antao, V. P., Lai, S. Y., and Tinoco, I., Jr. 1991. A thermodynamic study of unusually stable RNA and DNA hairpins. *Nucleic Acids Res* **19**: 5901-5905.

Basu, S., and Strobel, S. A. 1999. Thiophilic metal ion rescue of phosphorothioate interference within the *Tetrahymena* ribozyme P4-P6 domain. *RNA* **5**: 1399-1407.

Brudvig, G. W. 1995. Electron paramagnetic resonance spectroscopy. *Methods Enzymol* **246**: 536-554.

Cate, J. H., Gooding, A. R., Podell, E., Zhou, K., Golden, B. L., Kundrot, C. E., Cech, T. R., and Doudna, J. A. 1996. Crystal structure of a group I ribozyme domain: principles of RNA packing. *Science* **273**: 1678-1685.

Cate, J. H., Hanna, R. L., and Doudna, J. A. 1997. A magnesium ion core at the heart of a ribozyme domain. *Nat Struct Biol* **4**: 553-558.

Cech, T. R. 1990. Self-splicing of group I introns. *Annu Rev Biochem* **59**: 543-568.

Celander, D. W., and Cech, T. R. 1991. Visualizing the higher order folding of a catalytic RNA molecule. *Science* **251**: 401-407.

Chin, K., Sharp, K. A., Honig, B., and Pyle, A. M. 1999. Calculating the electrostatic properties of RNA provides new insights into molecular interactions and function. *Nat Struct Biol* **6**: 1055-1061.

Christian, E. L., Kaye, N. M., and Harris, M. E. 2002. Evidence for a polynuclear metal ion binding site in the catalytic domain of ribonuclease P RNA. *EMBO J* **21**: 2253-2262.

Christopher, J. 1998. *SPOCK: The structural properties observation and calculation kit (Program Manual)* Center for Molecular Design: Texas A&M University.

Clardy, D. R., Horton, T. E., and DeRose, V. J. 1998. EPR measurements of Mn2+ binding to a hammerhead 'ribozyme' complex. *Abstracts of Papers of the American Chemical Society* **215**: U796-U796.

Cogoni, C., and Macino, G. 2000. Post-transcriptional gene silencing across kingdoms. *Curr Opin Genet Dev* **10**: 638-643.

Cohn, M. T., J. 1954. A study of manganous complexes by paramagnetic resonance absorption. *Nature* **173**: 1090-1091.

Collins, C. A., and Guthrie, C. 2000. The question remains: is the spliceosome a ribozyme? *Nat Struct Biol* **7**: 850-854.

Costa, M., and Michel, F. 1995. Frequent use of the same tertiary motif by self-folding RNAs. *EMBO J* **14**: 1276-1285.

Deras, M. L., Brenowitz, M., Ralston, C. Y., Chance, M. R., and Woodson, S. A. 2000. Folding mechanism of the *Tetrahymena* ribozyme P4-P6 domain. *Biochemistry* **39**: 10975-10985.

DeRose, V. J. 2003a. Metal ion binding to catalytic RNA molecules. *Current Opinion in Structural Biology* **13**: 317-324.

DeRose, V. J. 2003b. Metals, folding and catalysis in ribozymes. *Biochemistry* **42**: 8595-8595.

DeRose, V. J., S. Burns, N.-K. Kim and M. Vogt 2003. DNA and RNA as ligands. *Comprehensive Coordination Chemistry II* **8**: 787-813.

Doherty, E. A., and Doudna, J. A. 1997. The P4-P6 domain directs higher order folding of the Tetrahymena ribozyme core. *Biochemistry* **36**: 3159-3169.

Doherty, E. A., and Doudna, J. A. 2000. Ribozyme structures and mechanisms. *Annu Rev Biochem* **69**: 597-615.

Doherty, E. A., Herschlag, D., and Doudna, J. A. 1999. Assembly of an exceptionally stable RNA tertiary interface in a group I ribozyme. *Biochemistry* **38**: 2982-2990.

Doudna, J. A., and Cech, T. R. 1995. Self-assembly of a group I intron active site from its component tertiary structural domains. *RNA* **1**: 36-45.

Downs, W. D., and Cech, T. R. 1996. Kinetic pathway for folding of the Tetrahymena ribozyme revealed by three UV-inducible crosslinks. *RNA* **2**: 718-732.

Draper, D. E. 2004. A guide to ions and RNA structure. *RNA* **10**: 335-343.

Draper, D. E., and Gluick, T. C. 1995. Melting studies of RNA unfolding and RNA-ligand interactions. *Methods Enzymol* **259**: 281-305.

Feig, A. L. 1999. The use of manganese as a probe for elucidating the role of magnesium ions in ribozymes. *Metal Ions in Biological Systems* **37**: 157-182.

Feig, A. L., Panek, M., Horrocks, W. D., Jr., and Uhlenbeck, O. C. 1999. Probing the binding of Tb(III) and Eu(III) to the hammerhead ribozyme using luminescence spectroscopy. *Chem Biol* **6**: 801-810.

Galli, C., Innes, J. B., Hirsh, D. J., and Brudvig, G. W. 1996. Effects of dipole-dipole interactions on microwave progressive power saturation of radicals in proteins. *Journal of Magnetic Resonance Series B* **110**: 284-287.

Giedroc, D. P., Theimer, C. A., and Nixon, P. L. 2000. Structure, stability and function of RNA pseudoknots involved in stimulating ribosomal frameshifting. *J Mol Biol* **298**: 167-185.

Gluick, T. C., and Draper, D. E. 1994. Thermodynamics of folding a pseudoknotted mRNA fragment. *J Mol Biol* **241**: 246-262.

Golden, B. L., Gooding, A. R., Podell, E. R., and Cech, T. R. 1998. A preorganized active site in the crystal structure of the *Tetrahymena* ribozyme. *Science* **282**: 259-264.

Gordon, P. M., Sontheimer, E. J., and Piccirilli, J. A. 2000. Metal ion catalysis during the exon-ligation step of nuclear pre-mRNA splicing: extending the parallels between the spliceosome and group II introns. *RNA* **6**: 199-205.

Groebe, D. R., and Uhlenbeck, O. C. 1988. Characterization of RNA hairpin loop stability. *Nucleic Acids Res* **16**: 11725-11735.

Guerrier-Takada, C., Gardiner, K., Marsh, T., Pace, N., and Altman, S. 1983. The RNA moiety of ribonuclease P is the catalytic subunit of the enzyme. *Cell* **35**: 849-857.

Hertzberg, R. P., and Dervan, P. B. 1984. Cleavage of DNA with methidiumpropyl-EDTA-iron(II): reaction conditions and product analyses. *Biochemistry* **23**: 3934-3945.

Hirsh, D. J., Beck, W. F., Innes, J. B., and Brudvig, G. W. 1992. Using saturation-recovery EPR to measure distances in proteins: applications to photosystem II. *Biochemistry* **31**: 532-541.

Horton, T. E., Clardy, D. R., and DeRose, V. J. 1998. Electron paramagnetic resonance spectroscopic measurement of Mn^{2+} binding affinities to the hammerhead ribozyme and correlation with cleavage activity. *Biochemistry* **37**: 18094-18101.

Hunsicker, L. M., and DeRose, V. J. 2000. Activities and relative affinities of divalent metals in unmodified and phosphorothioate-substituted hammerhead ribozymes. *Journal of Inorganic Biochemistry* **80**: 271-281.

Joyce, G. F., Vanderhorst, G., and Inoue, T. 1989. Catalytic activity is retained in the *Tetrahymena* group-I intron despite removal of the large extension of element P5. *Nucleic Acids Research* **17**: 7879-7889.

Juneau, K., and Cech, T. R. 1999. In vitro selection of RNAs with increased tertiary structure stability. *RNA* **5**: 1119-1129.

Juneau, K., Podell, E., Harrington, D. J., and Cech, T. R. 2001. Structural basis of the enhanced stability of a mutant ribozyme domain and a detailed view of RNA--solvent interactions. *Structure* (Camb) **9**: 221-231.

Kim, N. K., Murali, A. and DeRose, V.J. 2004. A distance ruler for RNA using EPR and site-directed spin labeling. *Chemistry & Biology* **11**: in press.

Kirchner, A. J. 2002. Investigation of metal binding properties in the hairpin ribozyme. M.S. Thesis Department of Chemistry, Texas A&M University.

Kruger, K., Grabowski, P. J., Zaug, A. J., Sands, J., Gottschling, D. E., and Cech, T. R. 1982. Self-splicing RNA: autoexcision and autocyclization of the ribosomal RNA intervening sequence of *Tetrahymena*. *Cell* **31**: 147-157.

Laggerbauer, B., Murphy, F. L., and Cech, T. R. 1994. Two major tertiary folding transitions of the *Tetrahymena* catalytic RNA. *EMBO J* **13**: 2669-2676.

Laing, L. G., and Draper, D. E. 1994. Thermodynamics of RNA folding in a conserved ribosomal RNA domain. *J Mol Biol* **237**: 560-576.

Laing, L. G., Gluick, T. C., and Draper, D. E. 1994. Stabilization of RNA structure by Mg ions. Specific and non-specific effects. *J Mol Biol* **237**: 577-587.

Latham, J. A., and Cech, T. R. 1989. Defining the inside and outside of a catalytic RNA molecule. *Science* **245**: 276-282.

Lilley, D. M. 2003. The origins of RNA catalysis in ribozymes. *Trends Biochem Sci* **28**: 495-501.

Liphardt, J., Onoa, B., Smith, S. B., Tinoco, I. J., and Bustamante, C. 2001. Reversible unfolding of single RNA molecules by mechanical force. *Science* **292**: 733-737.

Luptak, A., and Doudna, J. A. 2004. Distinct sites of phosphorothioate substitution interfere with folding and splicing of the *Anabaena* group I intron. *Nucleic Acids Res* **32**: 2272-2280.

Luptak, A., Ferre-D'Amare, A. R., Zhou, K., Zilm, K. W., and Doudna, J. A. 2001. Direct pK(a) measurement of the active-site cytosine in a genomic hepatitis delta virus ribozyme. *J Am Chem Soc* **123**: 8447-8452.

Michel, F., and Westhof, E. 1990. Modelling of the three-dimensional architecture of group I catalytic introns based on comparative sequence analysis. *J Mol Biol* **216**: 585-610.

Mikulecky, P. J., Takach, J. C., and Feig, A. L. 2004. Entropy-driven folding of an RNA helical junction: an isothermal titration calorimetric analysis of the hammerhead ribozyme. *Biochemistry* **43**: 5870-5881.

Milligan, J. F., and Uhlenbeck, O. C. 1989. Synthesis of small RNAs using T7 RNA polymerase. *Methods Enzymol* **180**: 51-62.

Misra, V. K., and Draper, D. E. 1998. On the role of magnesium ions in RNA stability. *Biopolymers* **48**: 113-135.

Murchie, A. I., Thomson, J. B., Walter, F., and Lilley, D. M. 1998. Folding of the hairpin ribozyme in its natural conformation achieves close physical proximity of the loops. *Mol Cell* **1**: 873-881.

Murphy, F. L., and Cech, T. R. 1993. An independently folding domain of RNA tertiary structure within the *Tetrahymena* ribozyme. *Biochemistry* **32**: 5291-5300.

Murphy, F. L., and Cech, T. R. 1994. GAAA tetraloop and conserved bulge stabilize tertiary structure of a group I intron domain. *J Mol Biol* **236**: 49-63.

Murray, J. B., Seyhan, A. A., Walter, N. G., Burke, J. M., and Scott, W. G. 1998. The hammerhead, hairpin and VS ribozymes are catalytically proficient in monovalent cations alone. *Chem Biol* **5**: 587-595.

Nakano, S., Cerrone, A. L., and Bevilacqua, P. C. 2003. Mechanistic characterization of the HDV genomic ribozyme: classifying the catalytic and structural metal ion sites within a multichannel reaction mechanism. *Biochemistry* **42**: 2982-2994.

Nissen, P., Hansen, J., Ban, N., Moore, P. B., and Steitz, T. A. 2000. The structural basis of ribosome activity in peptide bond synthesis. *Science* **289**: 920-930.

Nixon, P. L., and Giedroc, D. P. 1998. Equilibrium unfolding (folding) pathway of a model H-type pseudoknotted RNA: the role of magnesium ions in stability. *Biochemistry* **37**: 16116-16129.

Perrotta, A. T., Shih, I., and Been, M. D. 1999. Imidazole rescue of a cytosine mutation in a self-cleaving ribozyme. *Science* **286**: 123-126.

Pley, H. W., Flaherty, K. M., and McKay, D. B. 1994. Three-dimensional structure of a hammerhead ribozyme. *Nature* **372**: 68-74.

Puglisi, J. D., and Tinoco, I., Jr. 1989. Absorbance melting curves of RNA. *Methods Enzymol* **180**: 304-325.

Pyle, A. M. 1993. Ribozymes: a distinct class of metalloenzymes. *Science* **261**: 709-714.

Pyle, A. M. 2002. Metal ions in the structure and function of RNA. *J Biol Inorg Chem* **7**: 679-690.

Reed, G. H. 1984. Electron paramagnetic resonance studies of Mn(II) complexes with enzymes and substrates. *Biological Magnetic Resonance*. **6**: 73-142.

Rupert, P. B., and Ferre-D'Amare, A. R. 2001. Crystal structure of a hairpin ribozyme-inhibitor complex with implications for catalysis. *Nature* **410**: 780-786.

Schiemann, O., Weber, A., Edwards, T. E., Prisner, T. F., and Sigurdsson, S. T. 2003. Nanometer distance measurements on RNA using PELDOR. *J Am Chem Soc* **125**: 3434-3435.

Sclavi, B., Woodson, S., Sullivan, M., Chance, M. R., and Brenowitz, M. 1997. Time-resolved synchrotron X-ray "footprinting", a new approach to the study of nucleic acid structure and function: application to protein-DNA interactions and RNA folding. *J Mol Biol* **266**: 144-159.

Sclavi, B., Sullivan, M., Chance, M. R., Brenowitz, M., and Woodson, S. A. 1998. RNA folding at millisecond intervals by synchrotron hydroxyl radical footprinting. *Science* **279**: 1940-1943.

Scott, W. G., Finch, J. T., and Klug, A. 1995. The crystal structure of an all-RNA hammerhead ribozyme: a proposed mechanism for RNA catalytic cleavage. *Cell* **81**: 991-1002.

Serra, M. J., and Turner, D. H. 1995. Predicting thermodynamic properties of RNA. *Methods Enzymol* **259**: 242-261.

Shan, S., Kravchuk, A. V., Piccirilli, J. A., and Herschlag, D. 2001. Defining the catalytic metal ion interactions in the *Tetrahymena* ribozyme reaction. *Biochemistry* **40**: 5161-5171.

Shi, H., and Moore, P. B. 2000. The crystal structure of yeast phenylalanine tRNA at 1.93 A resolution: a classic structure revisited. *RNA* **6**: 1091-1105.

Silverman, S. K., Deras, M. L., Woodson, S. A., Scaringe, S. A., and Cech, T. R. 2000. Multiple folding pathways for the P4-P6 RNA domain. *Biochemistry* **39**: 12465-12475.

Sontheimer, E. J., Sun, S., and Piccirilli, J. A. 1997. Metal ion catalysis during splicing of premessenger RNA. *Nature* **388**: 801-805.

Stein, A., and Crothers, D. M. 1976. Conformational-Changes of Transfer-RNA - Role of Magnesium(Ii). *Biochemistry* **15**: 160-168.

Takamoto, K., He, Q., Morris, S., Chance, M. R., and Brenowitz, M. 2002. Monovalent cations mediate formation of native tertiary structure of the *Tetrahymena thermophila* ribozyme. *Nat Struct Biol* **9**: 928-933.

Tanner, N. K. 1999. Ribozymes: the characteristics and properties of catalytic RNAs. *FEMS Microbiol Rev* **23**: 257-275.

Theimer, C. A., and Giedroc, D. P. 1999. Equilibrium unfolding pathway of an H-type RNA pseudoknot which promotes programmed -1 ribosomal frameshifting. *J Mol Biol* **289**: 1283-1299.

Tullius, T. D., and Dombroski, B. A. 1985. Iron(II) EDTA used to measure the helical twist along any DNA molecule. *Science* **230**: 679-681.

Tullius, T. D., and Dombroski, B. A. 1986. Hydroxyl radical "footprinting": high-resolution information about DNA-protein contacts and application to lambda repressor and Cro protein. *Proc Natl Acad Sci USA* **83**: 5469-5473.

Turner, D. H., and Sugimoto, N. 1988. RNA structure prediction. *Annu Rev Biophys Biophys Chem* **17**: 167-192.

Uchida, T., He, Q., Ralston, C. Y., Brenowitz, M., and Chance, M. R. 2002. Linkage of monovalent and divalent ion binding in the folding of the P4-P6 domain of the Tetrahymena ribozyme. *Biochemistry* **41**: 5799-5806.

Valadkhan, S., and Manley, J. L. 2001. Splicing-related catalysis by protein-free snRNAs. *Nature* **413**: 701-707.

van der Horst, G., Christian, A., and Inoue, T. 1991. Reconstitution of a group I intron self-splicing reaction with an activator RNA. *Proc Natl Acad Sci USA* **88**: 184-188.

Vogt, M. a. D., V.J. 2003. Mn^{2+} sites investigated by advanced EPR techniques: in-depth study of Mn^{2+} ion-binding sites in the hammerhead ribozyme. *Paramagnetic Resonance of Metallobiomolecules* 193-211.

Wang, X. D., and Padgett, R. A. 1989. Hydroxyl radical "footprinting" of RNA: application to pre-mRNA splicing complexes. *Proc Natl Acad Sci USA* **86**: 7795-7799.

Wang, Y. H., Murphy, F. L., Cech, T. R., and Griffith, J. D. 1994. Visualization of a tertiary structural domain of the tetrahymena group-I intron by electron-microscopy. *Journal of Molecular Biology* **236**: 64-71.

Westhof, E. 2002. Group I introns and RNA folding. *Biochem Soc Trans* **30**: 1149-1152.

Woodson, S. A. 2002. Folding mechanisms of group I ribozymes: role of stability and contact order. *Biochem Soc Trans* **30**: 1166-1169.

Wu, M., and Tinoco, I., Jr. 1998. RNA folding causes secondary structure rearrangement. *Proc Natl Acad Sci USA* **95**: 11555-11560.

Yean, S. L., Wuenschell, G., Termini, J., and Lin, R. J. 2000. Metal-ion coordination by U6 small nuclear RNA contributes to catalysis in the spliceosome. *Nature* **408**: 881-884.

Zarrinkar, P. P., and Williamson, J. R. 1994. Kinetic intermediates in RNA folding. *Science* **265**: 918-924.

VITA

Shannon Naomi Burns was born in Bensalem, Pennsylvania on January 7, 1978. She was raised in Fairless Hills, Pennsylvania where she attended and graduated from Pennsbury High School in June of 1995. She went on to attend Millersville University located in Millersville, Pennsylvania where she received a Bachelor of Science degree in chemistry in May of 1999. In the fall of that same year, she began her research under the direction of Dr. Victoria J. DeRose at Texas A&M University. The author may be contacted through her parents at 129 Mountain View Rd., Titusville, NJ 08560.